OCS Study
BOEM 2019-029

Underwater Acoustic Monitoring Data Analyses for the Block Island Wind Farm, Rhode Island

US Department of the Interior
Bureau of Ocean Energy Management
Office of Renewable Energy Programs

BOEM
Bureau of Ocean Energy Management

OCS Study
BOEM 2019-029

Underwater Acoustic Monitoring Data Analyses for the Block Island Wind Farm, Rhode Island

May 2019

Authors (in alphabetical order):
Jennifer L. Amaral
Adam S. Frankel
Anwar A. Khan
Ying-Tsong Lin
James H. Miller
Arthur E. Newhall
Gopu R. Potty
Kathleen J. Vigness-Raposa

Prepared under BOEM Award
Contract No. M15PC00002,
Task Order No. M16PD00025
By
HDR
9781 S Meridian Boulevard, Suite 400
Englewood, CO 80112

U.S. Department of the Interior
Bureau of Ocean Energy Management
Office of Renewable Energy Programs

BOEM
Bureau of Ocean Energy Management

DISCLAIMER

Study concept, oversight, and funding were provided by the U.S. Department of the Interior, Bureau of Ocean Energy Management (BOEM), Environmental Studies Program, Washington, DC, under Contract Number M15PC00002, Task Order No. M16PD00025. This report has been technically reviewed by BOEM, and it has been approved for publication. The views and conclusions contained in this document are those of the authors and should not be interpreted as representing the opinions or policies of the U.S. government, nor does mention of trade names or commercial products constitute endorsement or recommendation for use.

REPORT AVAILABILITY

To download a PDF file of this report, go to the U.S. Department of the Interior, Bureau of Ocean Energy Management Data and Information Systems webpage (http://www.boem.gov/Environmental-Studies-EnvData/), click on the link for the Environmental Studies Program Information System (ESPIS), and search on 2019-029. The report is also available at the National Technical Reports Library at https://ntrl.ntis.gov/NTRL/.

CITATION

HDR. 2019. Underwater Acoustic Monitoring Data Analyses for the Block Island Wind Farm, Rhode Island. Final Report to the U.S. Department of the Interior, Bureau of Ocean Energy Management, Office of Renewable Energy Programs. OCS Study BOEM 2019-029. 110 pp.

ABOUT THE COVER

Cover photo: Block Island Wind Farm Facility Construction and Environmental Monitoring. Courtesy of HDR RODEO Team.

ACKNOWLEDGMENTS

The HDR RODEO Team includes the following subcontractors (in alphabetical order):

- Arthur Popper, Ph.D.
- Clark Group, LLC
- EA Engineering Science & Technology, Inc.
- Fugro Marine GeoServices, Inc.
- Fugro GB Marine Ltd.
- H.T. Harvey & Associates
- Loughine Limited
- Subacoustech Environmental.

Significant additional technical support for the monitoring effort was provided by the following institutions:

- Marine Acoustics, Inc.
- University of Rhode Island
- Woods Hole Oceanographic Institution
- Blue Land Media.

Vessel services for visual monitoring were provided by Hula Charters.

Assistance and support from all team members is greatly appreciated.

Contents

List of Figures

List of Tables

List of Abbreviations and Acronyms

3-D	three-dimensional
BIWF	Block Island Wind Farm
BOEM	Bureau of Ocean Energy Management
CTD	Connectivity, temperature, and depth
dB	decibel(s)
ft	foot/feet
Hz	Hertz
IPI	inter-pulse-interval
km	kilometer(s)
m	meter(s)
mi	mile(s)
mm/s	millimeter(s)per second
mm	millimeter(s)
m/s	meter(s)/second
µPa	micropascals
RMS	root mean square
RODEO	Real-Time Opportunity for Development Environmental Observations
S2R	source-to-receiver distance
SEL	sound exposure level
SHRU	Several Hydrophone Receiving Unit
SL	source level
SPL	sound pressure level
WTG	wind turbine generator

Editorial Notes

To facilitate presentation, review, and perusal of the large quantity of observations and data generated under Task Order M16PD00025, the deliverable is divided into four standalone volumes as follows:

1. **Field Observations during Wind Turbine Installation at the Block Island Wind Farm, Rhode Island (BOEM 2019-027)** – reports on the methods, data analyses, results, observations, and conclusions from environmental monitoring conducted at the BIWF under BOEM's RODEO Program during the *assembly of the wind turbine generator components (turbine towers, nacelles, and blades*).

2. **Field Observations during Wind Turbine Operations at the Block Island Wind Farm, Rhode Island (BOEM 2019-028)** – reports on the methods, data analyses, results, observations, and conclusions from environmental monitoring conducted at the BIWF under BOEM's RODEO Program during *turbine operations*.

3. **Underwater Acoustic Monitoring Data Analyses for the Block Island Wind Farm, Rhode Island (BOEM 2019-029)** – reports on the methods, observations, results, and conclusions from additional analyses of underwater acoustic monitoring data collected under BOEM's RODEO Program during *pile driving for securing the turbine foundations to the seabed*.

4. **Benthic Monitoring During Wind Turbine Installation and Operation at the Block Island Wind Farm, Rhode Island (BOEM 2018-047)** – Published in 2018, this report presented the methods, data analyses, results, observations, and conclusions from benthic monitoring conducted in 2017 and 2018 at the BIWF under BOEM's RODEO Program.

Executive Summary

This report presents methods, data, observations, results, and conclusions from analyses of underwater sound monitoring data that was collected during the construction of the Block Island Wind Farm (BIWF). The facility is located 4.5 kilometers (km) (2.8 miles [mi]) southeast of Block Island, Rhode Island. Construction was completed in two distinct phases. Phase 1 construction began in August 2015 and was conducted over an 18-week period. It included installation of wind turbine foundations on the seabed. Phase 2 construction was completed in two steps. In Step 1, which was initiated in January 2016, submarine power cables were laid on the seabed. In Step 2, which was completed over a two-week period (3 August–18 August) in 2016, a turbine tower, a nacelle, and three blades were assembled on each of the five wind turbine generator foundations. The nacelle is a case that houses all of the generating components in a wind turbine, including the generator, gearbox, drive train, and brake assembly.

During Phase 1 construction five wind turbine foundations were installed on the seabed within the BIWF Project Area. Unlike in Europe where the majority of the offshore wind turbines have monopile foundations, the BIWF turbine foundations consist of a jacket structure, which is tailored to accommodate the complex aerodynamic and hydrodynamic loading of deep waters. The four legs of the jacket structure are raked at an angle of 13.27° to the vertical. During construction, each steel jacket was lowered onto the seabed by a crane and then individual piles, which measured between 1.4 and 1.7 meters (m; 4.6 and 5.6 feet [ft]) in diameter, were placed into the guide holes at jacket corners. Impact (percussive) pile driving was used to drive the piles incrementally into the seabed. The piles were driven to their final penetration design depth of 76.2 m (250 ft) or until refusal, whichever came first.

Underwater acoustic monitoring was conducted during pile driving to detect and record underwater acoustic and sediment-borne signals generated by the pile driving impacts. Several stationary and a towed platform equipped with varying number of hydrophones were deployed for the data collection. The stationary mooring provided information at the deployment location (one range from the pile driving activity) whereas the towed array collected information across a variety of ranges during selected pile driving events. The towed array data was useful in addressing the question of the range at which a pile driving signal transitions from an impulsive signal to a non-impulsive signal. Knowing the transition point improves understanding of the potential effects to marine animals.

Results from ***preliminary*** data analysis[1] indicated that underwater pile driving sound was above background sound levels at ranges in excess of 20 km (12.4 mi) and that the received levels were approximately 120 decibels (dB) relative to 1 micropascals (µPa) root mean square (HDR 2018). Background sound levels at distances of 20 to 30 km (12.4 to 18.6 mi) from the construction site were recorded from 97.7 dB to a 125.7 dB (mean of 107.4 dB). Based on models calibrated with empirical data, the sound levels were a function of water depth, which varied based on direction away from the pile.

The key conclusion from preliminary data analyses was that underwater sound levels were lower in deep waters and higher in shallow waters; the difference between the two could be as large as 10 dB re 1 µPa root mean square. Sound levels were also shown to be dependent upon the orientation of the pile to the recording sensor. The piles were driven at an angle (13.3° relative to perpendicular). A 10 to 15 dB difference in sound levels resulted depending on whether the pile was angled towards or away from the measuring sensor. Particle motion, which is important to demersal fish and megabenthos, was greater at the seabed compared to higher in the water column.

[1] These results were separately reported in a document entitle "Field Observations during Wind Turbine Foundation Installation at the Block Island Wind Farm, Rhode Island" (HDR 2018).

Four sets of ***additional*** data analyses were conducted, and the results from these analyses are summarized below:

Pile Driving Data Analyses

During Phase 1 construction, impact (percussive) pile driving was used to drive piles incrementally into the seabed to secure the jacket foundation of each turbine to the sea floor. Impact pile driving creates intense sound that radiates into the environment and propagates through the air, water, and sediments. To monitor the underwater noise from the Phase 1 construction pile driving, an eight-hydrophone passive towed was deployed from a research vessel during three separate pile driving events. The hydrophone on the towed array recorded the noise from the pile driving as the vessel moved away from the construction site.

The recordings were analyzed to determine the sound levels of the pile driving versus range from the turbine, strike energy, pile angle, and penetration depth into the sediment. The analysis also investigated how the impulsive nature of the pile driving signal changes with range and how the angle of the raked pile being driven in relation to the array impacts the overall sound levels measured on the array.

Results from the data analyses indicated that the three monitoring events resulted in differing peak received levels, sound exposure levels, decay times, and kurtosis values. The differences were hypothesized to be due to the angle of the pile being driven relative to the towed array. The angle of the pile relative to the towed array changes based on the bearing of the array from the pile being driven. When the inclination of the pile relative to the array was towards the surface the received levels were highest. On the other hand, when the pile was angled towards the seabed relative to the array more sound energy was directed towards the sediment; therefore, less sound was transferred directly through the water column. Overall, the measured received levels from the impact pile driving varied significantly because of the pile rake and array bearing. The kurtosis of the pile driving signals also varied with range and bearing.

Pile driving of a raked pile results in azimuthal dependent sound radiation. Precise measurement of the beam pattern of the raked pile was not within the scope of this project, but the differences in signal characteristics and received level due to this azimuthal dependence were observed. This azimuthal dependence was the driving factor behind the differences in measurements seen in the data collected on the towed array. There was little correlation between the penetration depth and strike energy and the received sound levels recorded so no conclusion can be drawn as to how those affected the resulting sound field. As the towed array increased in range from the pile driving location the characteristics of the impulsive signal changed. The change in the signal duration and kurtosis suggest that the signal was becoming less impulsive with range, but there was no clear transition point to where the signal became definitively non-impulsive.

Particle Velocity Assessment

Pile driving operations produce intense sound and associated particle motion that propagates through the water, sediment and the water-sediment interface. Both sound levels and particle motion can potentially impact fish and invertebrates. Acoustic pressure gradients were determined using underwater acoustic monitoring data separately collected during 1) the BIWF Phase 1 construction and 2) turbine operations. These data were used to compute acoustic particle acceleration.

Particle velocity was estimated by numerically integrating the particle accelerations. Estimated particle acceleration data were compared with published behavioral audiograms for four fish species, namely, the Atlantic salmon (*Salmo salar*), plaice (*Pleuronectes platessa*), dab (*Limanda limanda*), and Atlantic cod (*Gadus morhua*). The comparison indicated that particle acceleration levels in water are slightly above the behavioral sensitivity in the frequency range 30 to 300 Hertz (Hz). This suggests that these fish may barely ‘detect’ the particle motion during construction at 500 m (1,640.4 ft) range.

The peak sound pressure levels measured in this study at 500 m (1,640.4 ft) are less than the levels that potentially result in mortality or injury as per ANSI-Accredited Standards Committee guidelines. The particle velocity levels measured on the seabed were well above the behavioral sensitivity for the four fish species up to a frequency of approximately 300 Hz. Hence, these species may barely 'detect' particle motion during construction at 500 m (1,640.4 ft) range. This also suggests that potential impacts from construction pile driving may be more pronounced on demersal (bottom-dwelling) fishes than pelagic species, which spend most of their time in the water column and away from the seabed. Pelagic fishes like herring may be affected more by the sound pressure rather than the particle motion. Overall, particle velocity measurement estimations agreed with values reported in the literature.

Comparison of seabed particle velocity estimations between the BIWF construction and operations phase indicated that the peak velocity levels (re 1 nm/s) on the seabed recorded during turbine operations were considerably lower (60 dB) when compared to the construction phase (120 dB).

Three-Dimensional (3-D) Underwater Sound Propagation Modeling

The BIWF Phase 1 construction underwater acoustic monitoring data were used to set up a 3-D underwater sound propagation model to extend the sound propagation predictions beyond the coverage of the in-situ listening measurements. The raked foundation design of the BIWF turbines along with the complicated bathymetry, bottom properties and oceanography presented unique challenges that had to be addressed during the model setup. Two parallel modeling approaches were adopted: A finite element modeling approach was used for 3-D source characterization of the raked steel pile in air, water and sediments, and a 3-D Parabolic Equation model was used to simulate underwater acoustic propagation of sound originating from the pile driving. Interpretation of model simulation output from the finite element modeling will be presented in future technical publications. Results and conclusions from the 3-D Parabolic Equation modeling are presented and discussed in this volume.

The model utilized an accurate numerical solution scheme to solve the 3-D Helmholtz wave equation with realistic ocean environmental information inputs. Analyses of the simulation outputs indicated that underwater sound propagation within the BIWF Project Area showed strong seasonal variability. The results suggested that pile driving sound decays faster in summer months, when the water column supports a downward refracting propagation condition. The BIWF Project area is characterized by a strong thermocline in summer, which produces a significant negative sound speed gradient of -3.2/s and generates a downward refracting propagation condition. This may be the cause of sound rays bending towards the seabed and hitting the bottom at greater angles resulting in higher bottom reflection loss.

In winter the surface water cool down because of less solar heat and atmosphere effects causing the thermocline to weaken. Also, in winter strong winds and storms can enhance water column mixing. As a result, the water temperature is nearly constant from the sea surface to the seabed, which produces an iso-velocity condition and more omni-directional propagation, in contrast to downward refracting in summer time. Also, colder water temperature in winter causes lower water sound speeds, which increases the acoustic impedance at the seabed. So, the total reflection angle from the bottom becomes greater compared to summer. This can remarkably enhance long distance propagation of underwater sound.

Marine Mammal Detection Analyses

Passive acoustic monitoring has become a standard methodology for assessing occurrence and distribution of marine mammals. The RODEO Program environmental monitoring offered a unique opportunity that allowed the data collected by platforms deployed underwater to monitor sounds associated with BIWF construction and operations to be analyzed for the presence of marine mammals. To effectively use passive acoustics to monitor marine mammals, an understanding of the area over which a given monitoring system can detect a particular species of interest is critical.

During the monitoring period, a single vocalizing fin whale (*Balaenoptera physalus*) was detected by the RODEO underwater acoustic system for an extended period of time and became the focus of the analysis. Fin whales are common marine mammals in waters off Rhode Island and vocalizations from these mammals were recorded at various times throughout the BIWF Phase I construction acoustic monitoring period. The fin whale vocalizations provided information that will help to increase the understanding of the propagation (and detection) of low-frequency vocalizations in shallow water environments.

The data, results, conclusions, and recommendations presented in this report were generated for the Bureau of Ocean Energy Management by the HDR RODEO Team under IDIQ Contract M15PC00002, Task Order M15PD00025.

1 Introduction

This report presents methods, data, observations, results, and conclusions from analyses of underwater sound monitoring data that was collected during the construction of the Block Island Wind Farm (BIWF) (**Figure 1**). The monitoring was conducted under the Bureau of Ocean Energy Management's (BOEM) Real-Time Opportunity for Development Environmental Observations (RODEO) Program.

Figure 1. The BIWF project area.

1.1 The RODEO Program

The purpose of the RODEO Program is to make direct, real-time measurements of the nature, intensity, and duration of potential stressors during the construction and initial operations of selected proposed offshore wind facilities. The purpose also includes recording direct observations during the testing of different types of equipment that may be used during future offshore development to measure or monitor activities and their impact producing factors.

BOEM conducts environmental reviews, including National Environmental Policy Act analyses and compliance documents for each major stage of energy development planning which includes leasing, site assessment, construction, operations, and decommissioning. These analyses include 1) identification of impact producing factors (stressors) and receptors such as marine mammals and seafloor (benthic) habitats, and 2) evaluation of potential environmental impacts from the proposed offshore wind development activities on human, coastal, and marine environments. The analyses require estimations of impact-producing factors such as noise and the effects from the stressor on the ecosystem or receptors. Describing the impact-producing factors requires knowledge or estimates of the duration, nature, and extent of the impact-generating activity. Since there have been no offshore facilities constructed in the United States prior to the BIWF, model predictions will be used primarily to forecast likely impacts from future projects.

The RODEO Program data may be used by BOEM as inputs to analyses or models that evaluate the effects or impacts from future offshore wind turbine construction and operations, as well as facilitate operational planning that would reduce potential impacts to the greatest extent possible. The understanding and insights gained from the BIWF monitoring program data analyses will help BOEM to identify, reduce, and mitigate environmental risks in the future, and significantly increase the efficiency and efficacy of BOEM's regulatory review process for offshore wind development in the United States. Finally, data collected by the BIWF monitoring program will support prioritization of future monitoring efforts and risk retirement. For example, if the BWIF monitoring data indicates that likelihood of impacts from a particular project development phase is low or inconsequential, then such phases may not be monitored during future projects.

It is important to note that the RODEO Program is not intended to duplicate or substitute for any monitoring that otherwise may be required by the developers of the proposed projects. Therefore, RODEO monitoring was limited to selected parameters only. Also, RODEO Program monitoring is coordinated with the industry and is not intended to interfere with or result in delay of industry activities.

The BIWF is the first facility to be monitored under the RODEO Program. All monitoring surveys were implemented in accordance with a pre-approved field sampling plan, which included a project-specific Health and Safety Plan (**Appendix A**). **Table 1** identifies the types of field data collected under the RODEO Program during construction and/or initial operations of this facility.

1.2 The Block Island Wind Farm

The BIWF is the first offshore wind farm in the United States, located 4.5 kilometers (km) (2.8 mi [mi]) from Block Island, Rhode Island. Water depth in the wind farm area is approximately 30 meters (m) (98.4 feet [ft]). The five-turbine, 30-megawatt facility is owned and operated by Deepwater Wind Block Island, LLC[2]. Power from the turbines is transmitted to Block Island. A 32 km (19.9 mi) transmission submarine power cable transfers excess power from Block Island to the mainland. This cable is buried under the ocean floor and makes landfall on the mainland, north of Scarborough Beach at Narragansett.

[2] Deepwater Wind was acquired by Ørsted of Denmark in 2018 and is now known as Ørsted US Offshore Wind.

Table 1. RODEO Program monitoring conducted at the BIWF.

Phase	Key Activities	Dates	Monitoring Surveys	Comment
Construction Phase 1	• Steel jacket foundations were installed on the seabed using two different types of hammers. Both derrick barges and a lift boat were used as construction platforms. Piles were installed with a 13.27° rake from the vertical.	26 July–26 October 2015.	• Visual observations and documentation of the construction activities. • Airborne noise monitoring associated with pile driving. • Underwater sound monitoring associated with pile driving. • Seabed sediment disturbance and recovery monitoring through bathymetry surveys conducted immediately after construction was completed and in approximately 3-month intervals for one year. • Turbine platform scour monitoring through installation of two scour monitoring devices on selected WTG foundations. • An Acoustic Wave and Current Profiler was also deployed within the project area.	Results, conclusions and recommendations from Construction Phase 1 monitoring were presented in the report entitled "*Field Observations during Wind Turbine Foundation Installation at the Block Island Wind Farm, Rhode Island. Final Report to the U.S. Department of the Interior, Bureau of Ocean Energy Management, Office of Renewable Energy Programs, OCS Study BOEM 2018-029 (HDR 2018a)*."
Construction Phase 2	• WTGs were installed on the steel foundations.	3 August–18 August 2016.	• Airborne noise monitoring. • Visual observations and documentation of activities.	Results, findings, conclusions, and recommendations from the Phase 2 Construction Monitoring are presented in the report entitled: "*Field Observations During Wind Turbine Installation at the Block Island Wind Farm, Rhode Island, OCS Study BOEM 2019-027 (HDR 2019a)*."

Phase	Key Activities	Dates	Monitoring Surveys	Comment
	• Submarine transmission power cables connecting Block Island and mainland were laid using a jet plowing in the offshore portions and horizontal directional drilling in the near shore area.	3 June–26 June 2016.	• Visual observations and documentation of the cable laying activities and of turbine installation from both on shore and off shore locations. • Still photography and filming of portions of trenching operations for cable laying. • Seabed sediment disturbance monitoring. • Post-construction seabed recovery through bathymetry surveys.	For details see report entitled: "*Observing Cable Laying and Particle Settlement During the Construction of the Block Island Wind Farm. Final Report to the U.S. Department of the Interior, Bureau of Ocean Energy Management, Office of Renewable Energy Programs, OCS Study BOEM 2017-027 (Elliot et al. 2017).*
Operational Phase	• Testing of the newly installed turbines. • Testing of the submarine transmission power cables.	Operational testing conducted from 29 August–30 November 2016.	• Visual observations of the operational wind farm from on shore and off shore locations at varying distances.	Results, conclusions, and recommendations from monitoring conducted during turbine operations are presented in an accompanying report entitled: "*Field Observations during Wind Turbine Operations at the Block Island Wind Farm, Rhode Island, OCS Study BOEM 2019-028 (HDR 2019b).*"
	• Facility operations.	Wind farm operation began on 2 December 2016.	• Airborne noise monitoring. • Underwater sound monitoring. • Seabed sediment disturbance and recovery monitoring.	
			• Benthic monitoring.	Results, conclusions, and recommendations from this monitoring are presented in an accompanying report entitled: "*Benthic Monitoring During Wind Turbine Installation and Operation at the Block Island Wind Farm, Rhode Island, OCS Study, BOEM 2018-047 (HDR 2018b).*"

Phase	Key Activities	Dates	Monitoring Surveys	Comment
Follow-on Data Analyses	• Additional in-depth analyses were conducted using data collected during construction Phase 1.	28 July– 31 December 2019	• No field surveys. Only desk-top data analyses and preliminary 3-dimensional modeling with were conducted during this phase.	Results, finding, conclusions and recommendations from the additional data analyses are presented in an accompanying report entitled: "*Underwater Acoustic Monitoring Data Analyses for the Block Island Wind Farm, Rhode Island, OCS Study BOEM 2019-029 (HDR 2019c).*"

BIWF construction began in July 2015, and was conducted in a phased manner through November 2016. During the first phase, five turbine foundations were installed on the seabed from 26 July to 26 October 2015. These turbines were designated as wind turbine generator (WTG) 1 to WTG 5. Unlike in Europe where the majority of the offshore wind turbines have monopile foundations, the BIWF turbine foundations consist of a four-legged jacket structure, which is tailored to accommodate the complex aerodynamic and hydrodynamic loading of deep waters. The four legs of the jacket structure are raked at an angle of 13.27° to the vertical.

Phase 2 construction was completed in two steps. In Step 1, which was initiated in January 2016, submarine power cables were laid on the seabed. In Step 2, which was conducted over a two-week period in August 2016, a turbine tower, a nacelle, and three blades were assembled on each of the five WTG transition decks. During this assembly, the first of three turbine tower sections was bolted in place on each transition deck and then the other two sections were sequentially placed on top of the first section. A nacelle was then connected to the top of the tower and three blades were installed on the nacelle.

Operational testing of the facility was conducted from August through November 2016, and the initial operations commenced on 2 December 2016.

1.3 Underwater Acoustic Monitoring and Data Analyses

During Phase 1 construction, five wind turbine foundations were installed on the seabed within the Project Area. Each steel jacket was lowered onto the seabed by a crane and then individual piles, which measured between 1.4 to 1.7 m (4.6 to 5.6 ft) in diameter, were placed into the guide holes at jacket corners. Impact (percussive) pile driving was used to drive the piles incrementally into the seabed. The piles were driven to their final penetration design depth of 76.2 m (250 ft) or until refusal, whichever came first.

Underwater acoustic monitoring was conducted during active pile driving to detect and record underwater sound and sediment-borne signals generated by pile driving. Several stationary and a towed platform equipped with varying number of hydrophones were deployed for the data collection. The stationary mooring provided information at the deployment location (one range from the pile driving activity) whereas the towed array collected information across a variety of ranges during selected pile driving events. The towed array data was useful in addressing the question of the range at which a pile driving signal transitions from an impulsive signal to a non-impulsive signal. Knowing the transition point is important to improve understanding of the potential effects to marine animals.

In a previous report on field observations at BIWF (HDR 2018), a description of the underwater acoustic monitoring methods and results from *preliminary data analyses* were presented. This report is a follow-on compendium, which include results from *detailed* analysis of the underwater acoustic monitoring data collected during the pile driving. The following chapters in this report address the specific analyses:

- **Section 2** presents methods, results, and key observations from detailed pile driving data analyses.
- **Section 3** contains results and discussion of the particle velocity estimations.
- **Section 4** describes the three-dimensional (3-D) underwater sound propagation model and includes findings from the analyses of the model simulated data.
- **Section 5** includes a discussion of the marine mammal detections and modal dispersion.

The results from *preliminary* analyses indicated that underwater pile driving sound was above background sound levels at ranges in excess of 20 km (12.4 mi) and that the received levels were

approximately 120 decibels (dB) relative to 1 micropascals (μPa^2) root mean square (RMS) (HDR 2018). Background sound levels at distances of 20 to 30 km (12.4 to 18.6 mi) from the construction site were recorded from 97.7 to 125.7 dB (mean of 107.4 dB). Based on models calibrated with measured data, the sound levels were a function of water depth, which varied based on direction away from the pile.

The key conclusion from ***preliminary*** data analyses reported was that underwater sound levels were lower in deep waters and higher in shallow waters; the difference between the two could be as large as 10 dB re 1 µPa RMS. Sound levels were also shown to be dependent upon the orientation of the pile to the recording vessel. The piles are driven at an angle (13.3° relative to perpendicular). A 10 or 15 dB difference in sound levels resulted depending on whether the pile was angled towards, perpendicular, or away from the measuring vessel. Particle motion, which is important to demersal fish and megabenthos, was greater at the seabed compared to higher in the water column.

Additional data analyses were then conducted for the following purposes:

1. Determine the sound levels of pile driving as a function of range from the turbine, strike energy, pile angle, and penetration depth into the sediments. These analyses also included evaluating how the impulsive nature of the pile driving signal changes with distance from the pile, and how the angle of the raked piles being driven impact the overall received sound levels. Based on the hammer type, the difference in the levels of noise radiating from the pile driving hammer impacts were investigated. Background noise was characterized and compared with the data collected during prior studies. Kurtosis of the data were calculated to investigate the changes in this metric as a function of range and pile rake.

2. Evaluate propagation of sound and associated particle motion through water, sediment, and the water-sediment interface. This evaluation also included reviewing available literature on particle velocity measurements and potential impacts on fishes.

3. Set up, calibrate, and validate a three-dimensional underwater sound propagation model for assessing seasonal variation of underwater sound propagation. Model setup included consolidating available environmental information including sound speed profiles from conductivity, temperature, and depth (CTD) data, bathymetry and geo-acoustic information. The model can potentially be used to understand, predict and exploit temporal (hourly, daily, monthly and seasonal) and spatial (on-site, local and regional) variability of underwater sound propagation for mitigating, managing and planning noise impacts of BIWF or other future wind farm's construction and operation.

4. Detect and analyze the presence of marine mammals in the vicinity of the wind farm.

1.4 Report Organization

Key results, observations, and conclusions from the additional analyses conducted using the construction Phase 1 underwater acoustic monitoring data are summarized in individual sections of this report:

- **Section 1** presents an overview of the BIWF Facility and the RODEO Program, and includes a summary description acoustic data analysis.
- **Section 2** presents methods, results, and key observations from pile driving data analyses.
- **Section 3** contains results and discussion of the particle velocity estimations.
- **Section 4** describes the 3-D underwater sound propagation model and includes findings from the analyses of the model simulated data.
- **Section 5** includes a discussion of the marine mammal detections and modal dispersion.

- **Section 6** contains the references cited in the report.

Raw data and detailed discussions from each type of analysis are contained in technical reports, which are provided as digital appendices to this summary report.

2 Pile Driving

Each BIWF turbine foundations consist of a four-legged, steel, jacket structure. Each jacket consists of a lattice structure with four hollow leg structures at the corners. The individual jacket legs are referred to as A1 (western leg), A2 (southern leg), B1 (northern leg), and B2 (eastern leg). Leg B1 has a ladder for crew access. The legs of the jacket structure are raked at an angle of 13.27° to the vertical (**Figure 2**). Raked piles are common in infrastructure projects because of their increased resistance to lateral loads. Because of the non-axisymmetric geometry of the pile relative to the water column and seabed, raked piles are expected to radiate underwater sound with an azimuthal dependence (Wilkes and Gavrilov 2017).

During Phase 1 construction, the steel jacket of each wind turbine foundation was lowered onto the seabed by a crane. Then individual piles, which measured between 1.4 and 1.7 m (4.6 and 5.6 ft) in diameter, were placed into the guide holes at jacket corners. Impact (percussive) pile driving was used to drive the piles incrementally into the seabed (**Figure 3**).

Three separate pile segments were used at each leg. The first segment (P1) was inserted into guide hole and driven into leg structure until approximately 20 percent of the P1 pile segment remained above the guide hole. Then the second pile segment (P2) was welded onto segment P1 and pile driving continued until approximately 20 percent of the P2 pile segment remained above the guide hole. Finally, the third segment (P3) was welded onto segment P2 and pile driving continued until the entire pile was driven to the final penetration design depth of 76.2 m (250 ft) or until refusal, whichever came first. For record keeping and reporting purposes, individual pile segments were identified separately for each leg. For example, the label "WTG 1, B2P3" refers to the third pile that was driven into leg B2 of the first turbine.

Impact pile driving creates intense sound that radiates into the environment and propagates through the air, water, and sediments. Observational and numerical studies suggest that only approximately 0.5 percent of the hammer energy used during pile driving translates into acoustic energy in the water column (Dahl et al. 2015). To monitor the underwater noise from the Phase 1 construction pile driving, an eight-hydrophone passive towed was deployed from a research vessel during three separate pile driving events. The hydrophone on the towed array recorded the noise from the pile driving as the vessel moved away from the construction site.

The recordings were analyzed to determine the sound levels of the pile driving versus range from the turbine, strike energy, pile angle, and penetration depth into the sediment. The analysis also investigated how the impulsive nature of the pile driving signal changes with range and how the angle of the raked pile being driven in relation to the array impacts the overall sound levels measured on the array. *No relevant comparable data was available from European wind farm measurements and analyses, therefore the RODEO Project findings could not be validated against prior investigations*.

Key results and major conclusions from the data analysis are summarized below. Additional details are presented in the Technical Report contained in **Appendix A**.

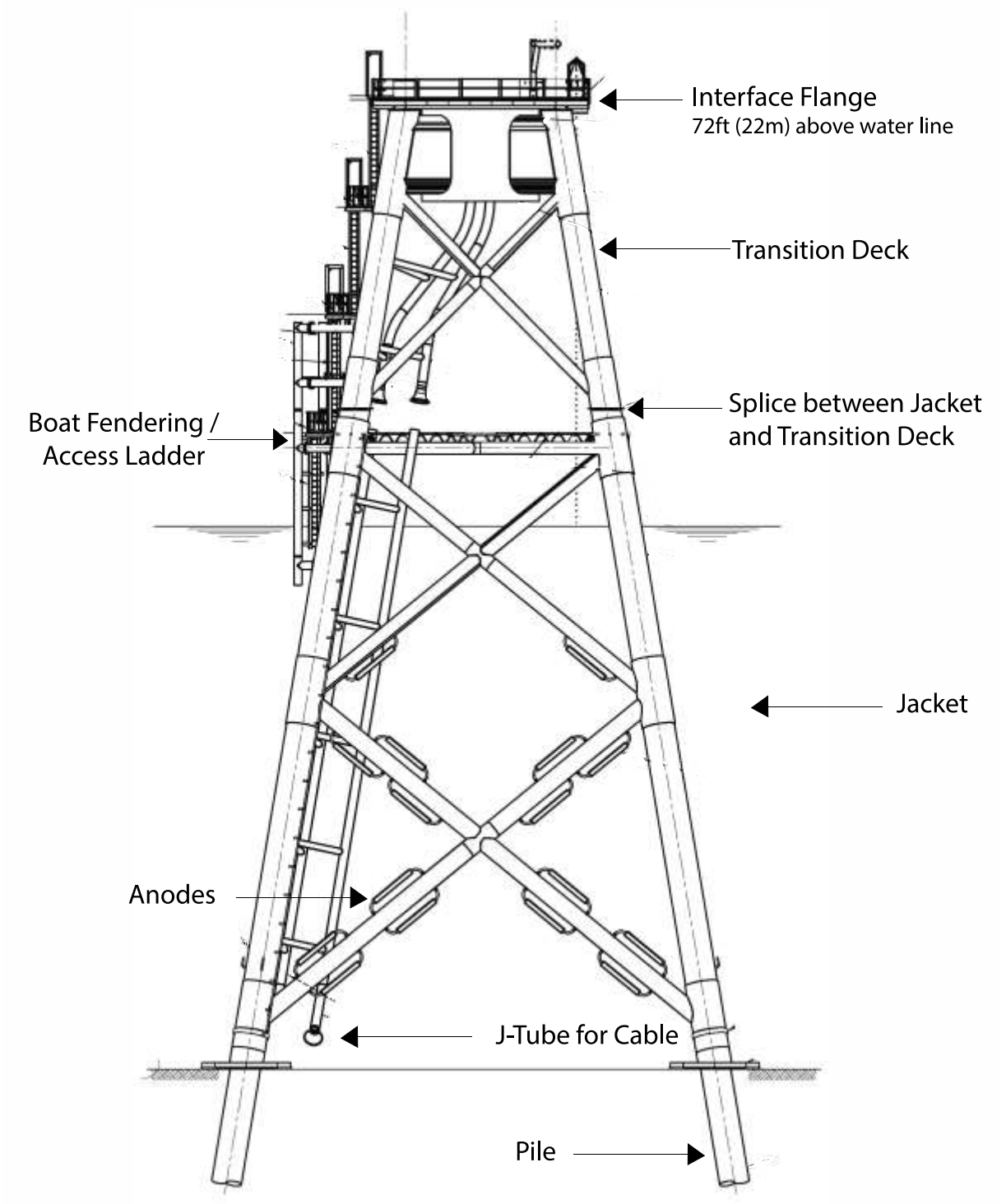

Figure 2. Schematic of the lattice jacket foundation structure showing the raked piles.

Figure 3. BIWF Phase 1 Construction Pile Driving. Top panel: Piles inserted in jacket prior to start of pile driving. Lower panel: Pile driving in progress.

2.1 Data Collection

An eight-hydrophone passive towed array built by Hydroscience Technologies, Inc. was deployed to record sound from impact pile driving events. The hydrophone elements were irregularly spaced to allow for beam-forming at multiple frequencies. The array was towed from the R/V *Shanna Rose*, which is based at the University of Rhode Island's dock at the Point Judith Marina.

A customized acoustic data acquisition system was designed for use with the towed array. It included Alligator BNC input/output boxes, an Alligator SCS-800 chassis with an Alligator 820 Bessel-function filter card, a National Instruments SCB-68 interface box, and a National Instruments PCI 6071E analog-to-digital conversion card. The array was powered by two 12V batteries connected in series. The data were recorded using the software program Raven (Charif et al. 2010) in 30-second files at a sampling rate of 64 kilohertz. Gains of 1x, 10x, or 100x were applied during data acquisition in the field depending on the range of the array from the pile driving event and the associated signal-to-noise ratio.

During data collection, the array was towed as straight as possible along a radial emanating from the pile-driving location. If pile driving stopped, the boat slowed or stopped until pile driving started again. The GPS positions of the R/V *Shanna Rose* were recorded throughout the duration of the towed array deployment. These data were used during the analysis to determine the range of the array to the pile-driving events at all points during the towing operations.

Monitoring was conducted on two separate days. On 2 September 2015, two pile driving events, namely WTG 3 A2P1 and WTG 3 B2P1 were monitored. On 17 September 2015, a single pile driving event, WTG 5 A1P1, was monitored. The track lines for the three monitored piling driving events are shown in in **Figure 4**. The locations of the A1, A2, and B2 legs of the lattice jacket foundations are provided in **Figure 5**.

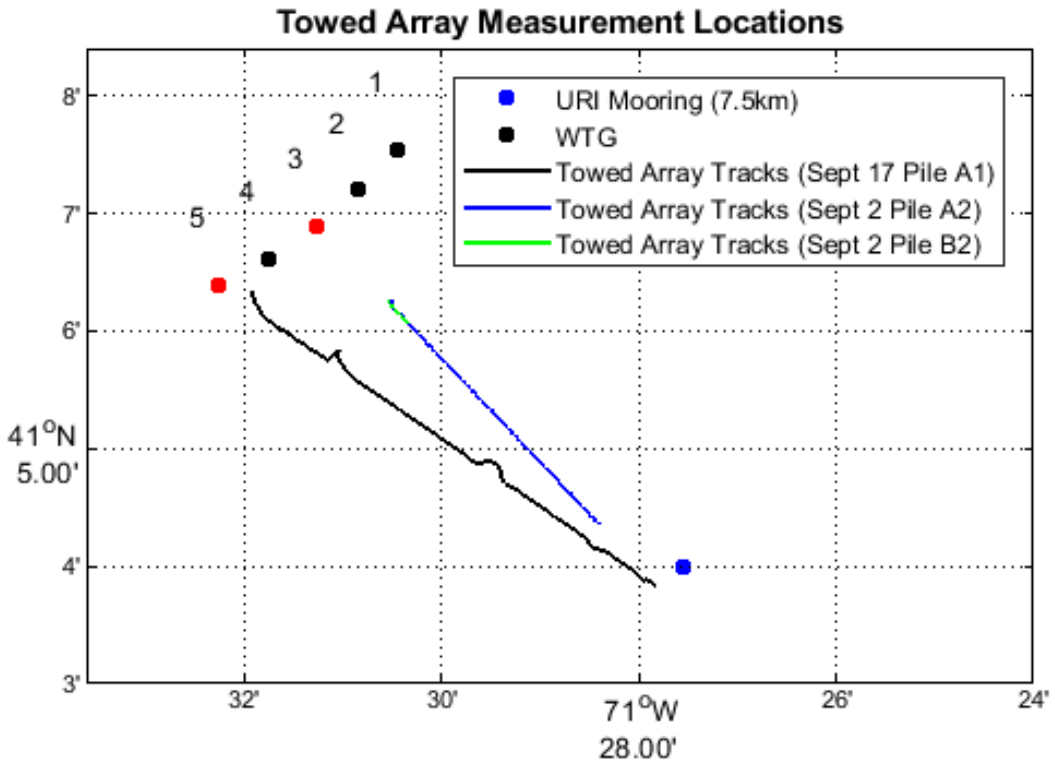

Figure 4. Towed array track lines for the three piling events. Wind turbine locations are indicated by black dots. The red dots indicate the turbines on which pile driving data were recorded.

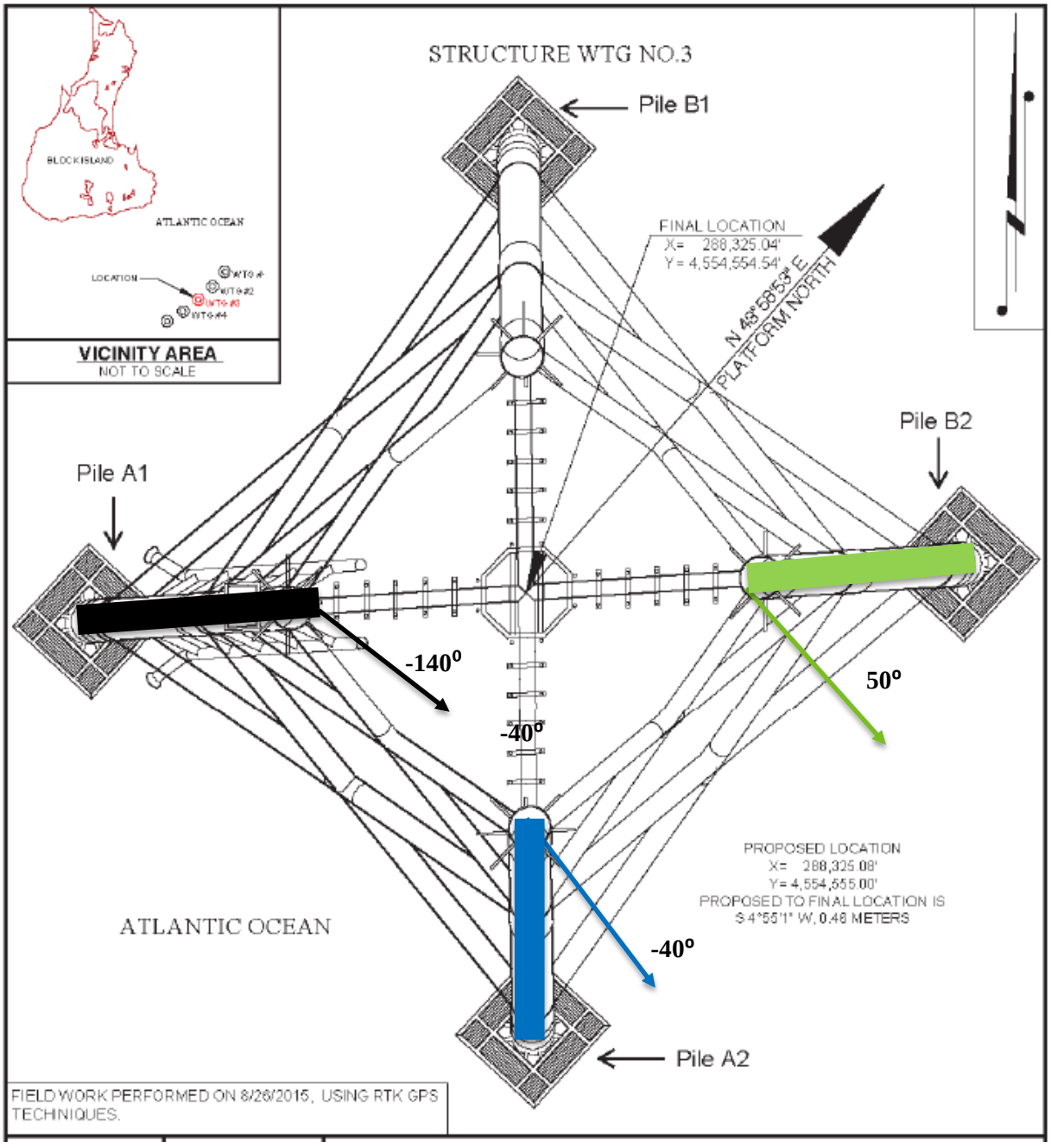

Figure 5. Indications of which piles were driven during the specific deployment days of 17 September 2015 (black), 2 September 2015 pile event 1 (green) and 2 September 2015 pile event 2 (blue). Calculated horizontal orientation angles between pile and array transit are indicated. Arrows represent the direction of the towed array transit in relation to the pile.

2.2 Data Analysis Methods

2.2.1 Range Determination

The distance between the vessel position and the pile was determined by great circle calculations using GPS data from the R/V *Shanna Rose*. Because the GPS position recorded was that of the vessel, the distance offset from the GPS receiver to the middle of the array had to be determined. The distance from the GPS receiver to the stern of the boat was estimated at 7 m (23 ft), the amount of hydrophone array lead-in cable was 47 m (154.2 ft), and the distance to the center of the array was 50 m (164 ft). Therefore, a distance offset of 104 m (341.2 ft) was used in the analysis.

2.2.2 Pile and Towed Array Orientation

Using the bearing of each towed array transit in relation to the center of the wind turbine and the orientation of each pile, the orientation of the towed array transit in relation to the pile was calculated. The horizontal angle between the array and the piles driven on 2 September was 50° and -40°, whereas the angle between the array and the pile driven on 17 September was approximately -140° (**Figures 6** and **7**). A positive angle is clockwise from the towed array track line to the pile and a negative angle is measured counterclockwise from the track line to the pile being driven.

The horizontal angles calculated for the two events on 2 September shows that the towed array transit was at approximately the same relative angle for both piles driven. The orientation of the pile to the array was much different on 17 September, with the relative angle of the pile being more towards the seabed bottom than during the measurements made on 2 September. When the array is oriented such that the pile is angled more towards the seabed, the top of the pile is closer to the array. When the bottom of the pile is closer to the array than the top, this is defined as the pile angled towards the surface (**Figure 7**).

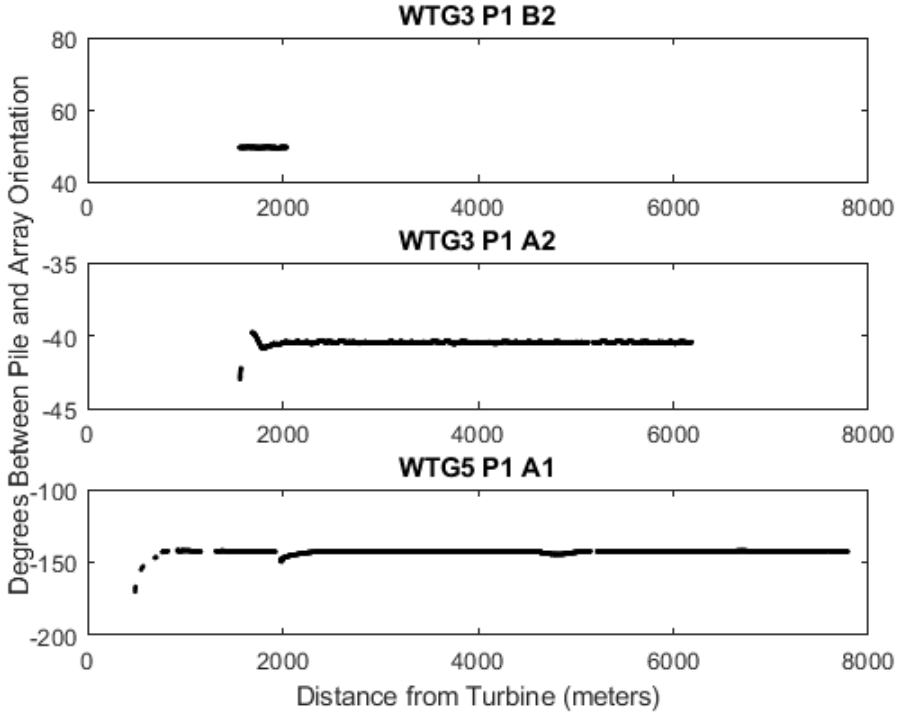

Figure 6. Horizontal angle between the towed array track line along the transit and the orientation of the pile being driven for all three pile driving events. Angle is measured clockwise relative to the pile. A negative angle means the array is east of the pile being driven.

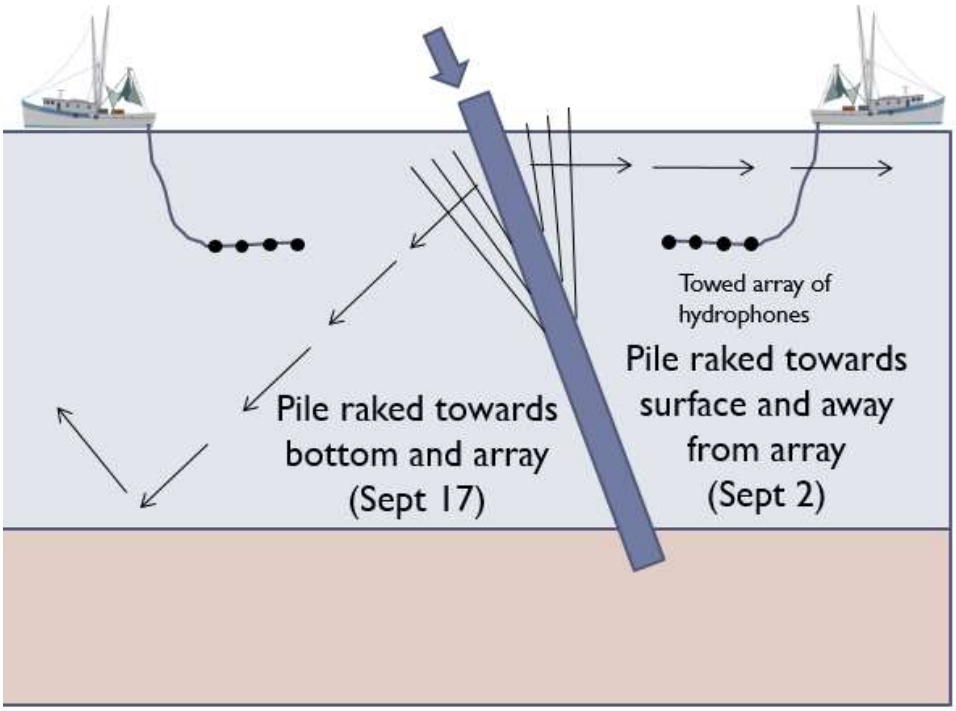

Figure 7. Schematic showing the orientation of the pile towards the array on both measurement days. The V-shaped lines emanating from the pile represent the Mach cone produced when the pile is struck.

Wilkes and Gavrilov (2017) demonstrated that sound radiation from a raked pile is significantly different at various horizontal directions from the pile. They reported sound exposure levels (SELs) radiated by piles raked at an angle of 14° to the vertical and inclined towards the array direction to be 10 dB in the opposite direction.

2.2.3 Underwater Mach Wave Generated from Pile Driving

The high-pressure underwater sound field generated from impact pile driving on hollow steel pipes is attributed to a "Mach wave" effect (Dahl et al. 2015). Elastic waves are excited in the steel pile because of hammer strikes. The hammer energy travels down the length of the pile as compressional waves, which causes the pile to bulge outwards and deform. This radial deformation of the pile wall is due to the Poisson effect, which occurs when a material is compressed in one direction and expanded in another. The bulge acts as the sound source because it produces pressure waves in the air, water, and sediment as it moves down the length of the pile (Wilkes and Gavrilov 2017).

The compressional wave speed in steel is much greater than the speed in water. As the pressure wave from the pile enters the water it will slow down, causing a Mach cone around the pile. The angle of this Mach cone depends on the ratio of the compressional wave speed in water to that in steel. Assuming the compressional wave speed in steel (Cs) is 5,300 meters/second (m/s) and the speed through water (Cw) is 1,500 m/s, the angle of the Mach cone relative to the axis of the pile would be approximately 16^0, which was calculated using **Equation 1**. Depending on the precise values of Cw and Cs, the angle could range from 15^0 to 19^0 (Dahl et al. 2015).

$$\theta = \sin^{-1}\frac{Cw}{Cs} \qquad \text{(Equation 1)}$$

The angle calculated in **Equation 1** is relative to the axis of the pile. When the pile is raked, the sound level radiated from the pile will depend on the orientation from the pile. The wave front of the primary Mach wave radiated in the direction of the pile incline has a much steeper incidence angle on the seabed compared to that in the opposite direction where it propagates almost horizontally (**Figure 8**). Because of the non-axisymmetric geometry of the pile relative to the water column and seabed, raked piles are expected to radiate underwater sound with an azimuthal dependence, with sound levels varying by approximately 10 dB in different directions (Wilkes and Gavrilov 2017).

2.2.4 Acoustic Analysis

The data from both measurement days were recorded using consecutive 30-second duration files. The total number of files and piling time collected on both days is shown in **Table 2**. The total time used in the analysis for each pile is also shown. This excludes any clipped data and includes all of the data used in the analysis presented in this report. The track lines that correspond to the data used in the analysis are shown in **Figure 4**. The data collected on WTG 5 on 17 September had lower dynamic range than the data collected on 2 September.

All analysis was completed using custom MATLAB scripts. Each individual 30-second duration file was opened in MATLAB and adjusted to account for the amplifier gain and hydrophone sensitivity. Thus, each file then represented the received level of the sound at each hydrophone.

A peak detector was employed to locate all of the pile driving impulses in the recordings. For each impulse, the peak and peak-to-peak sound pressure received levels were calculated according to **Equations 2** and **3**, respectively.

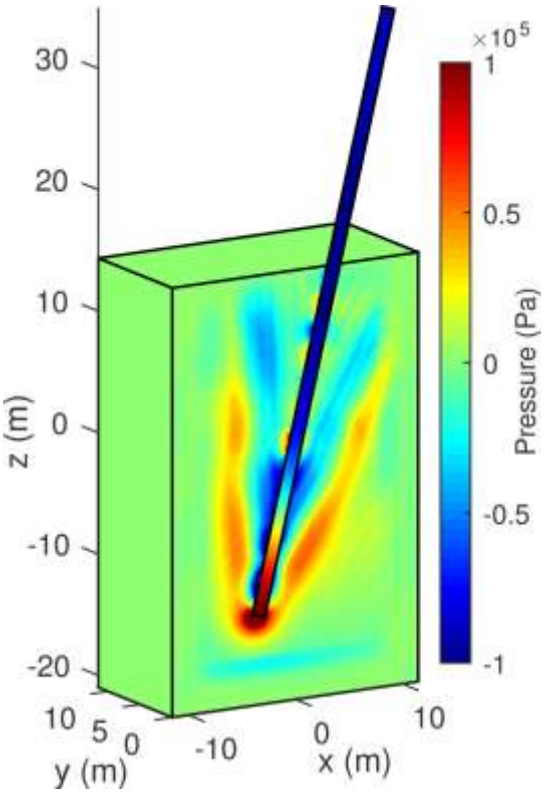

Figure 8. Schematic showing the orientation of the pile towards the array on both measurement days. The V-shaped lines emanating from the pile represent the Mach cone produced when the pile is struck (Wilkes and Gavrilov 2017).

Table 2. Total size and number of files collected during both cruise days.

Date	Number of Files Collected	Total Data Collected	Total Recorded Time Used in Analysis
9/2/2015	145	4.08 GB	Pile B2: 4.7 minutes Pile A2: 50.1 minutes
9/17/2015	342	9.76 GB	Pile A1: 74.4 minutes

$$RL_{pk} = 20\log_{10}(max(|P(t)|)) \qquad \text{(Equation 2)}$$

$$RL_{pk-pk} = 20\log_{10}(max(P(t)) - min(P(t))) \qquad \text{(Equation 3)}$$

The sound exposure level was also calculated for each impulse according to **Equation 4**, with the signal duration being defined as the 90 percent envelope (T_{90}) or the amount of time that contains 90 percent of the signal energy. This is a meaningful definition of the signal duration that begins when the cumulative signal energy exceeds 5 percent (T_5) of the total signal energy and ends when it reaches 95 percent (T_{95}) of this value. The 90 percent envelope is $T_{95} - T_5$.

$$SEL = 10\log_{10}\left(\int_{T5}^{T95} P(t)^2 dt\right) \qquad \text{(Equation 4)}$$

The rise and decay times of each impulse were also calculated. The rise time was defined as the peak time minus the time at which 5 percent of the energy is present (T_5). The decay time was defined as the time at which 95 percent of the energy is present (T_{95}) minus the peak time.

The kurtosis of each impulse was also calculated. Kurtosis is a measure of the "impulsiveness" and variance of a signal. Higher kurtosis relates to a signal where the variance is a result of infrequent extreme deviations as opposed to frequent, modestly sized deviations. A signal that has the same power spectrum can have much different kurtosis values depending on the impulsiveness of the signal. For example, **Figure 9** provides a comparison of two signals that have the same energy spectrum. The signal on the left has constant variance and deviations and results in a kurtosis of 3. The signal on the right is impulsive and therefore consists of an extreme pressure fluctuation, which results in a higher kurtosis value of 189.

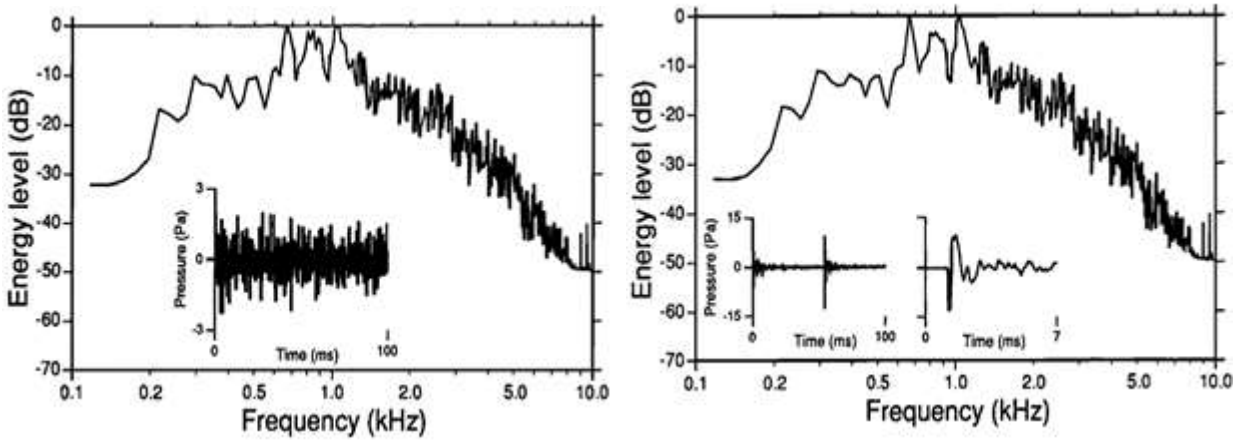

Figure 9. Comparison of two signals that have the same average energy spectrums but result in different kurtosis values depending on the impulsiveness of the signal. The signal on the left has a kurtosis value of 3, whereas the signal on the right has a kurtosis value of 189 (Hamernik 1993).

A time window of 0.1 second before and 0.8 second after the peak were used for this calculation. This time window was chosen to account for the varying time interval between hammer drops. This window ensured the kurtosis calculation only contained one impulse and did not overlap adjacent hammer drops. Examples of the time windows used in the SEL and kurtosis calculations are shown in **Figure 10**. These metrics were plotted against range from the pile to visualize the variation in values over distance and investigate the range dependence of the signal.

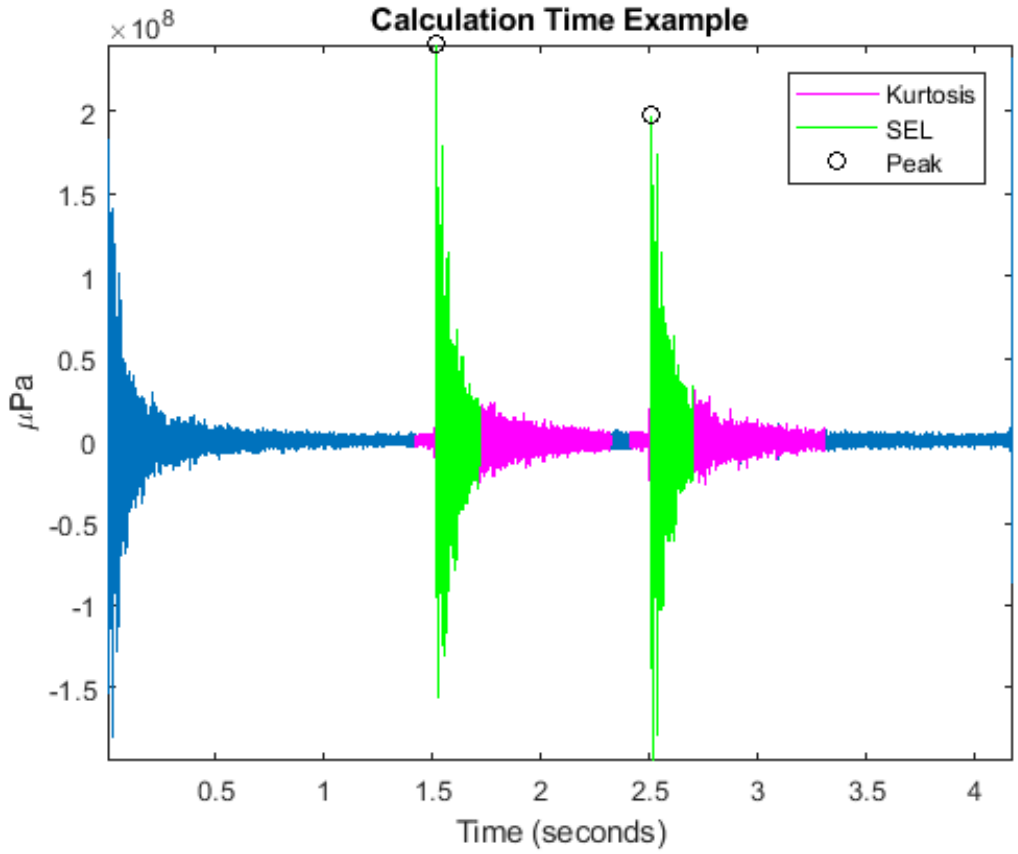

Figure 10. Example of time windows used for SEL and kurtosis calculations on two impulses.

2.2.5 Statistical Analysis

One of the reasons for applying a statistical model to these data is that many of the predictive variables (i.e., penetration depth of the pile into the sediment, strike energy of each hammer impulse, range of the array from pile driving activity) were dynamic and changed throughout the measurement period. For example, the range from source to receiver was increasing, the strike energy generally increased in large increments (blue line, **Figure 11**) and the penetration depth into the sediment gradually increased (black line, **Figure 11**).

If these varying contributions from the predictive variables are not parsed, counter-intuitive results can occur. For example, a simple plot of received level measured on the towed array as a function of strike energy (**Figure 11**) shows that as the strike energy increased, received level decreased. This paradoxical finding is the result of simultaneous changes in strike energy, range of array from pile driving, and pile penetration depth.

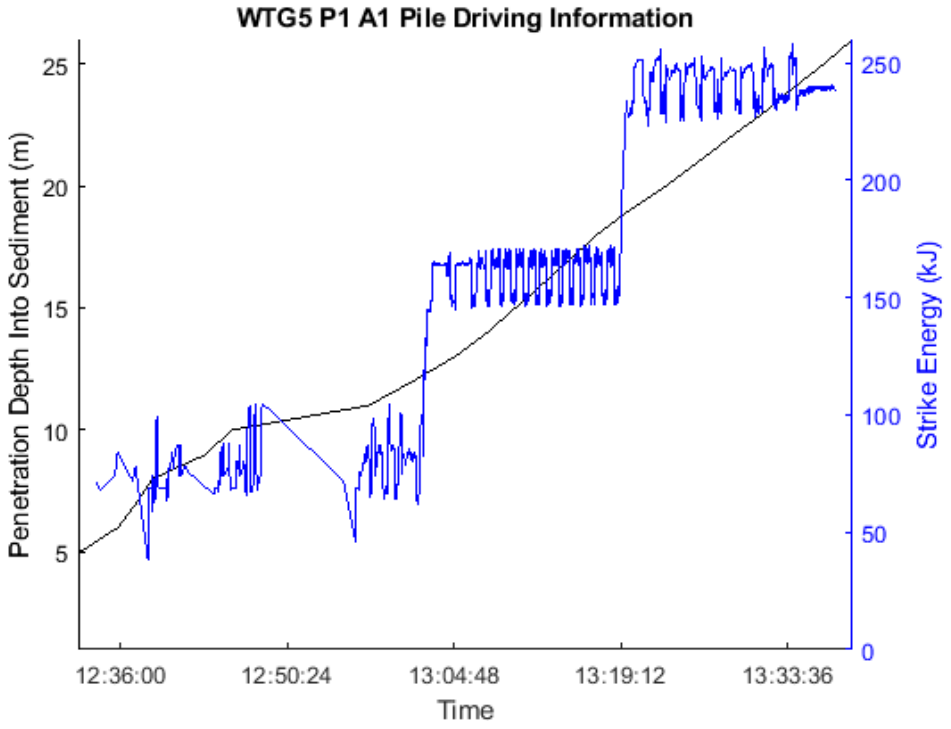

Figure 11. Penetration depth (black) and strike energy (blue) over the course of the A1 pile being driven during the 17 September 2015 recording.

The combined data from both measurement days and three piling events were analyzed statistically using multiple regression models to explore the relationship of the received level metrics as functions of the following predictor (independent) variables:

1. the log of range
2. the 3-D angle of the pile relative to the hydrophone array (described below)
3. pile penetration depth (Johnson transformed to reduce skewness)
4. strike energy (kilojoules)
5. the interaction term of strike energy and pile depth.

The individual measures of peak RL, SEL and kurtosis from the eight hydrophones were averaged for each pile strike. This prevented artificial inflation of sample size and pseudo replication. Individual regression models were created for each dependent metric.

Because the piles were raked relative to vertical, the 3-D angle or apparent angle of the pile changed depending on the orientation of the array to the pile. This is illustrated in **Figure 13**. The piles are angled at 13.27˚ relative to the centerline of the support jacket. The 3-D angle relative to the receiver was calculated using **Equation 5** and **Figure 13**, where β is the horizontal angle between the pile and direction of the receiver (**Figure 5**). A positive 3-D angle means the pile is angled more towards the surface and a negative angle means the pile is angled more towards the seabed.

$$3D\ Angle = \tan^{-1}(\cos\beta * \tan(13.27°)) \qquad (Eq.5)$$

For example, pile B2 has an orientation of 90°. The bearing from the jacket structure to the ship was around a constant of 140˚. Thus, the horizontal angle between the pile being driven and the array was roughly 50˚ (140˚ to 90˚) and the 3-D angle of the pile relative to the array was 8.6˚.

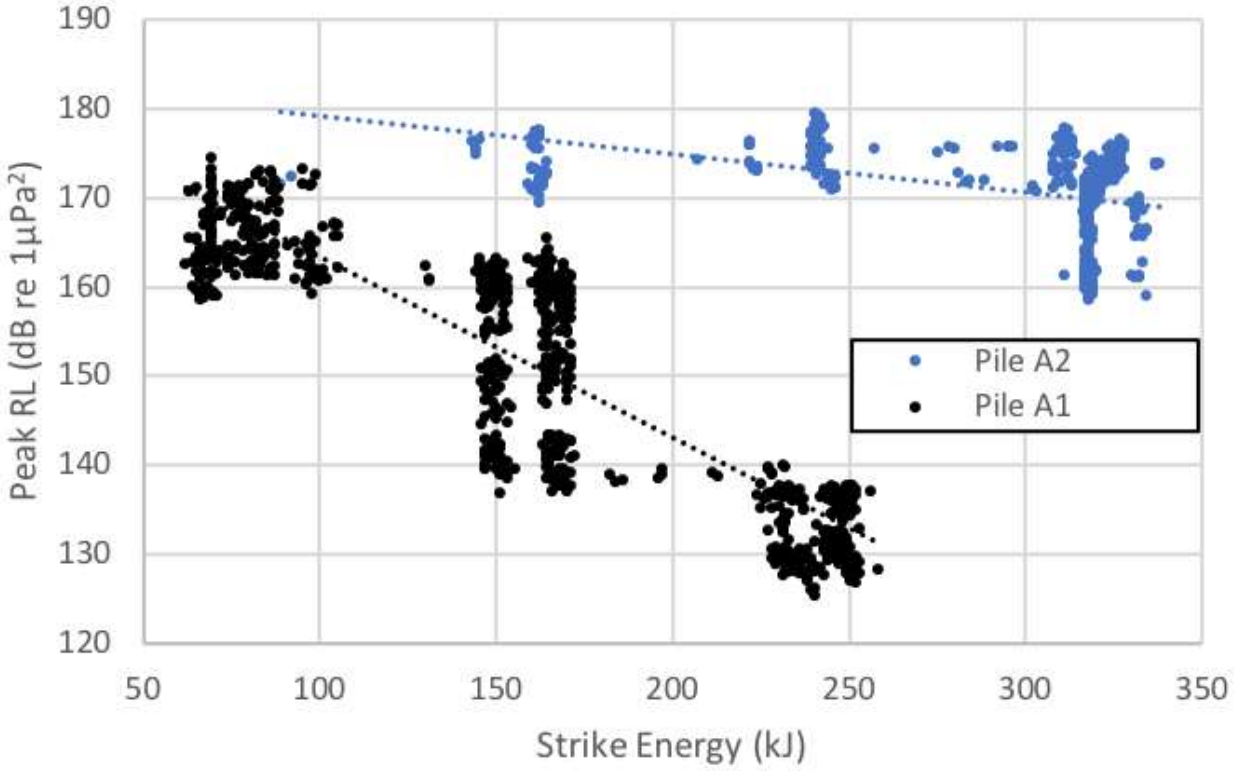

Figure 12. Simple plot of towed array peak received level as a function of strike energy. This presentation shows a decrease in received sound levels as strike energy increases. This paradoxical finding is the result of simultaneous changes in strike energy, receiver range and pile penetration depth. Pile A2 is from 2 September and Pile A1 is from 17 September.

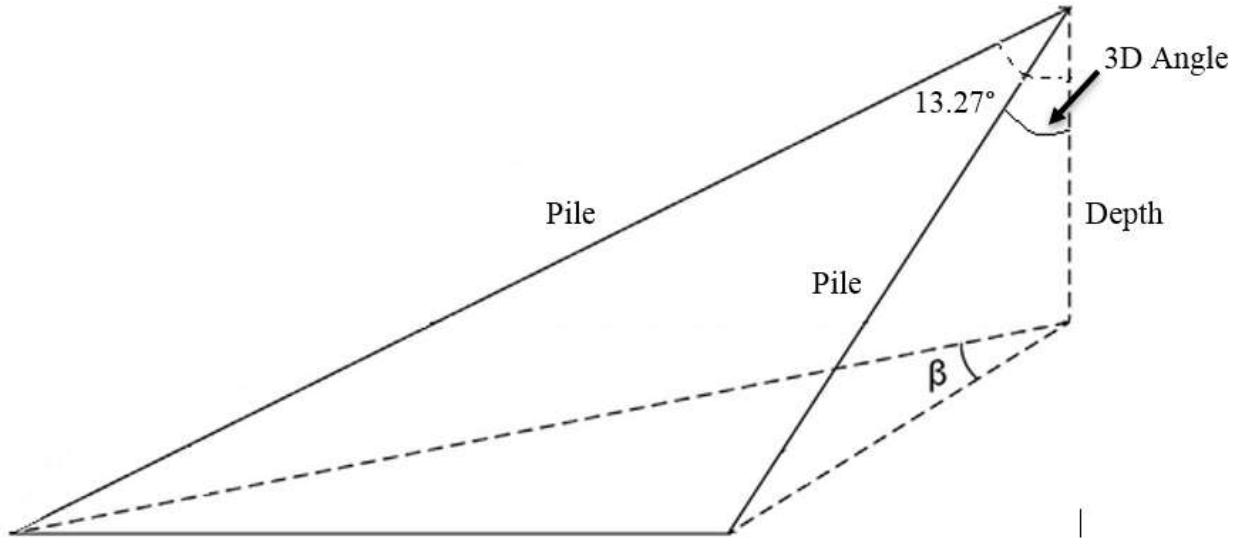

Figure 13. Schematic showing the 3-D apparent angle and how this angle changes with the perspective of the array. The pile length and depth are constant, but the angle of the pile to the vertical appears to change as the horizontal angle (β) from the pile direction changes. This apparent angle is measured as the 3-D angle according to Equation 5.

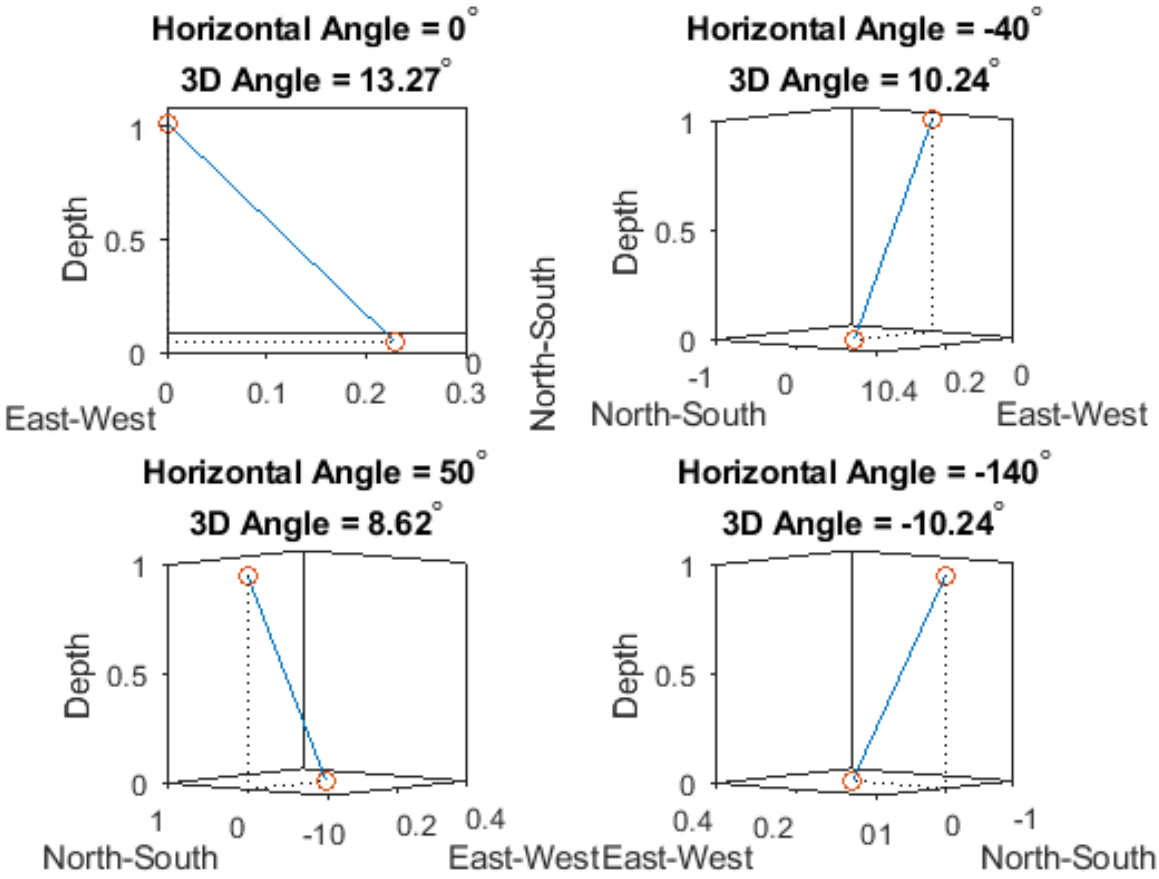

Figure 14. An illustration of the 3-D angle, the bearing dependent apparent angle between the pile and a vertical line. The views that result from the horizontal orientation of the pile and array, as shown in Figure 5, are shown. The resulting 3-D apparent angles for each array orientation are provided. A negative 3-D angle means the pile is angled more towards the bottom, whereas a positive angle is when the pile is angled more towards the surface in relation to the array location.

2.3 Results

2.3.1 Pile Driving Sound

2.3.1.1 Received Levels

Peak received level for each pile driving impulse for all three pile-driving events are shown in **Figure 15**. The peak RL calculated for all three pile driving events revealed larger RLs from the piles angled towards the surface (blue and green) versus the pile angled towards the bottom (black). Because the orientation of the Mach cone is relative to the raked pile, when the pile was angled towards the bottom more energy was directed towards the sediment. This resulted in more bottom interactions and subsequent attenuation that reduced the measured received levels at range. When the array was oriented such that the pile was angled towards the surface, the Mach cone propagated more horizontally through the water column and therefore suffered less interface attenuation, as supported by **Figures 7** and **8**. The same trend is seen in the SEL calculations in **Figure 16**. Both **Figures 15** and **16** show a decrease in RL and SEL with distance. The trend is similar in both figures, but levels appear different due to difference in units.

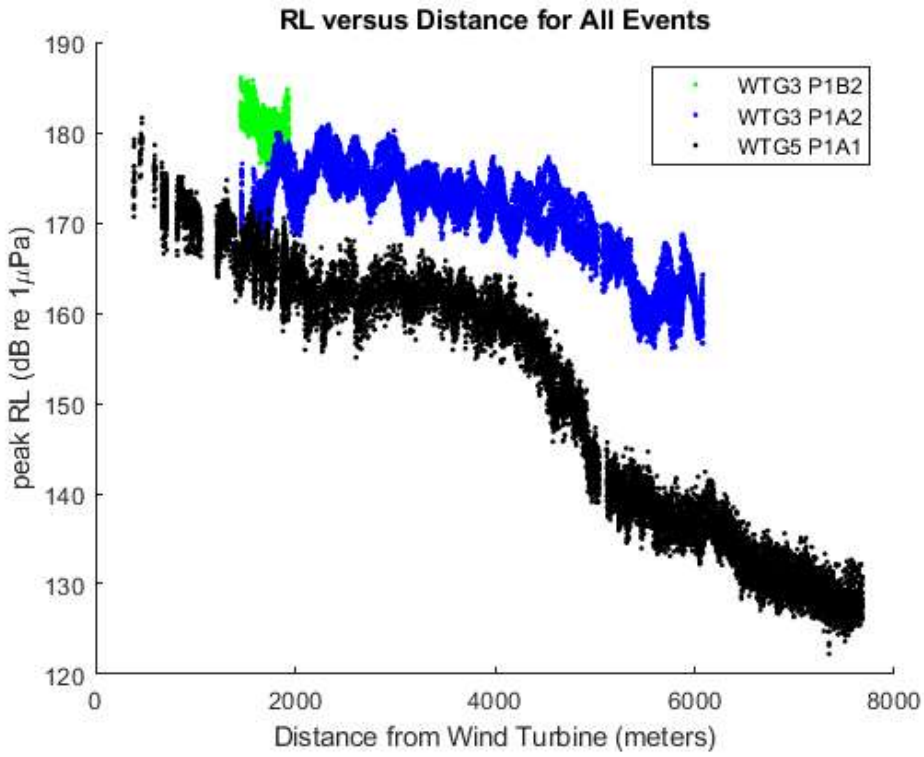

Figure 15. Peak received level for each pile driving impulse for all three pile driving events.

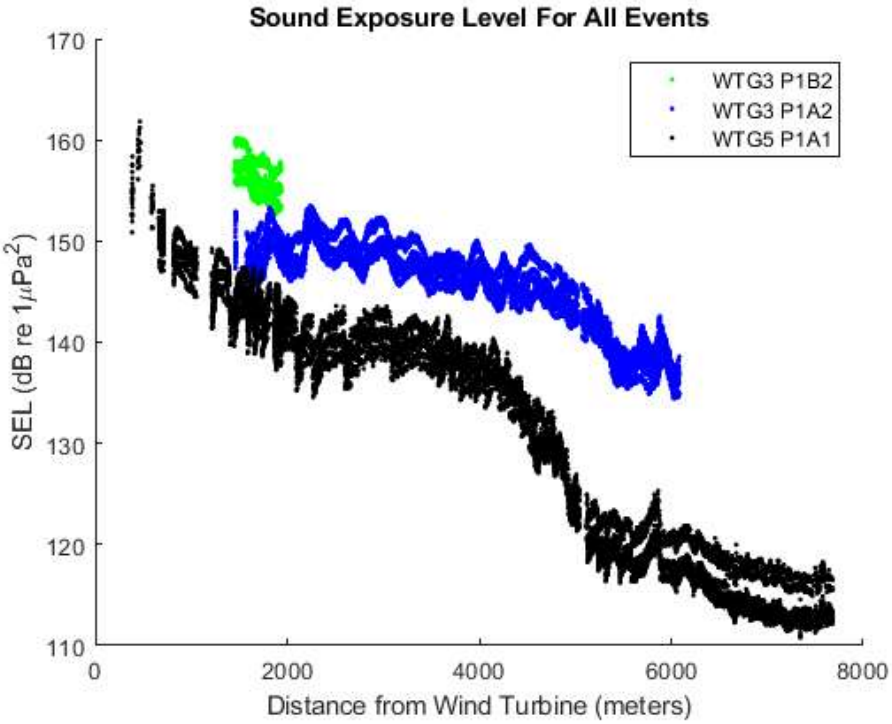

Figure 16. Single strike sound exposure levels using signal duration of T90 for each pile-driving impulse for all three pile-driving events.

Comparison of peak RL measurements (**Figure 15**) to the NMFS 2018 peak unweighted permanent threshold shifts and temporary threshold shifts indicates that all BIWF measurements were below the peak temporary threshold shifts and permanent threshold shifts values for all hearing groups.

In summary, the main factor that affected the measured RLs was the relative angle of the pile to the towed array. In general factors such as temperature, depth and bathymetry affect propagation, but these factors were relatively constant between the two measurement days. Therefore, the most important factor affecting the RL measurements was the pile being driven.

2.3.1.2 Kurtosis

Kurtosis is a measure of the impulsiveness of a signal (Hamernik et al. 1993). As the array travels farther from the pile driving, the signal has increased travel and spreading time. This results in an elongated signal because of multipath arrivals, which decreases the impulsiveness of the signal in the time domain. Therefore, signals received at closer ranges are expected to have higher kurtosis than those at farther ranges. The relative trend of the measured kurtosis in **Figure 16** shows the kurtosis decreasing as the array moves out in range. This trend is seen regardless of the inclination of the pile in relation to the array.

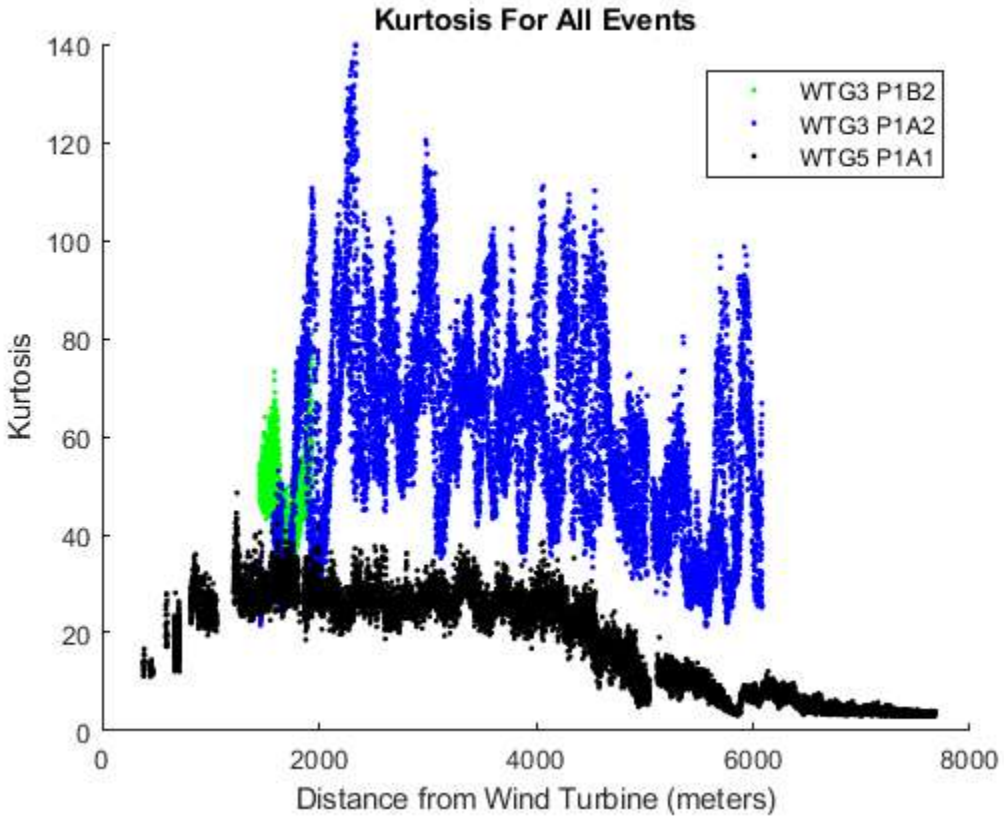

Figure 17. Kurtosis for each pile-driving impulse for all three pile-driving events. Calculated using 0.1 second before and 0.8 second after the peak.

2.3.1.3 Decay Time

The decay time of each impulse increases with range of the array from the pile. This is consistent with the kurtosis trend seen in **Figure 18** because as the signal elongates, the kurtosis should decrease. The increase in decay time is due to the multipath arrivals spreading out in time as the array moves away from the pile.

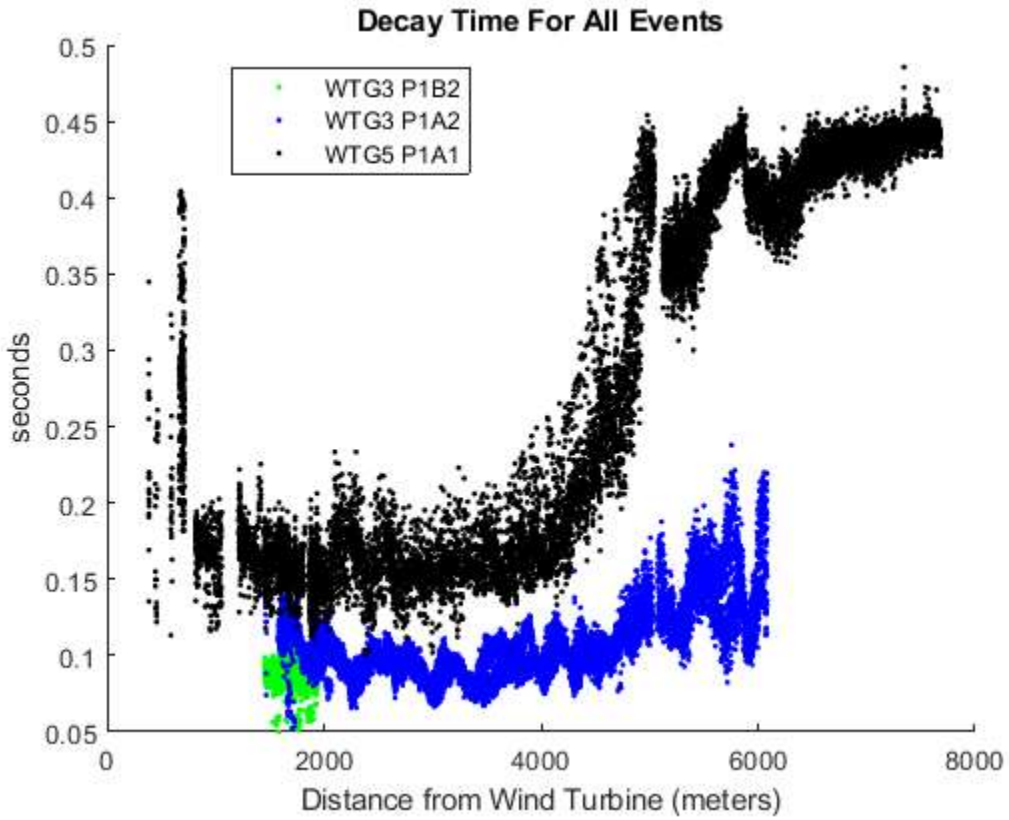

Figure 18. Decay time for each pile driving impulse for all three pile driving events. Calculated by determining the time interval between the peak and the time at which 95 percent of the energy had passed (T_{95}).

2.3.2 Statistical Analysis

Table 3 summarizes the direction and magnitude of the relationship between the measured (dependent) and predictor (independent) variables in all of the previous tables. Using the t-ratio values, the significance of the parameter in defining the relationship is represented with one + or – sign if the t-ratio value is less than 1, two + or – signs if the t-ratio value is greater than 1 but less than 10, and three + or – signs if the t-ratio value is greater than 10. NS stands for "non-significant."

Both received sound level metrics of peak RL and SEL decreased strongly with range. Kurtosis initially increased at short ranges and then decreased strongly at ranges beyond 4,500 m (2.8 mi) (**Table 3**). Likewise decay time only began to significantly increase at ranges greater than 4,500 m (2.8 mi). The kurtosis and decay time metrics show the effect of increased multipath arrivals with increasing range.

Table 3. Statistical Summary. The sign indicates the direction of the effect and the number of + or – signs indicate the relative strength of the effect based on the t-ratio values. NS indicates a non-significant effect.

Predictors		Measured Values			
		Peak RL	SEL	Kurtosis	Decay Time
Log Range	Near	---	---	++	NS
	Far	---	---	---	+++
3-D Angle	Near	+++	+++	+++	---
	Far	--	--	--	++
Penetration Depth	Near	--	NS	--	++
	Far	+++	+++	NS	---
Strike Energy	Near	+++	+++	++	---
	Far	++	++	NS	++
Strike Energy x Penetration Depth	Near	++	NS	++	--
	Far	NS	NS	---	+++

The analysis indicated that when the pile is raked toward the surface in relation to the array the received levels metrics and kurtosis both increase at the closer ranges, while decay time decreases. The opposite pattern is seen at ranges greater than 4,500 m (2.8 mi). All of these effects are consistent with sound that propagates more horizontally in the water column. The subsequent reduction in boundary interactions reduced transmission loss.

Penetration depth had little effect on received level at close ranges, but increased received level at greater ranges. This may be due to enhanced coupling of the pile to the sediment and subsequent acoustic re-radiation into the water column. The effect of increased penetration depth on kurtosis and decay time was less clear, with apparently contradictory effects of reducing kurtosis but increasing decay time at short ranges.

Increased strike energy led to increased received level metrics at all ranges and kurtosis near the turbine. Decay time decreased at close range near the turbine but increased at longer ranges. This may be due to a slightly stronger main pulse at close ranges and increased multiple arrivals at longer ranges.

2.4 Discussion and Conclusions

The three different pile driving events recorded on the towed array resulted in differing peak received levels, sound exposure levels, decay times and kurtosis values. The differences were hypothesized to be due to the angle of the pile being driven relative to the towed array. In general factors such as temperature, depth and bathymetry could potentially affect sound propagation, but these factors were relatively constant between the two measurement days. Therefore, the single most influential factor affecting the received level measurements was the pile being driven.

The angle of the pile relative to the array changes based on the bearing of the array from the pile being driven. **Figure 5** indicates that the horizontal bearing of the array to the piles was similar for the 2 September deployments, but much different during the 17 September deployment. This difference in bearing resulted in the pile being angled more towards the seabed during the 17 September measurements than for the 2 September measurements.

The inclination of pile towards the surface produced higher received levels, as predicted by pile jacket geometry and Mach cone propagation theory (Reinhall and Dahl 2011, Wilkes and Gavrilov 2017). This was noted when the received levels recorded on 2 September were higher than those recorded on 17 September. Increased kurtosis values when the pile is inclined towards the surface also derived from

enhanced propagation through the water column and fewer interactions with the waveguide boundaries. Therefore, the received signal was more impulsive and the signal energy was not as elongated in time because it contained fewer multipath arrivals. On the other hand, when the pile was angled towards the seabed, more sound energy was directed towards the sediment; therefore, less sound was transferred directly through the water column.

The signal elongating in time was directly observed by measuring the decay time of each impulse. The decay time increased with range, with a sharp increase at a distance of approximately 4,500 m (2.8 mi). The data from 2 September also showed the decay time trending upwards approximately 4,500 m (2.8 mi). This sharp increase could be a result of propagation effects due to varying bathymetry along this radial.

Overall, the raked pile has an azimuthal dependent beam pattern. Precise measurement of the beam pattern was not within the scope of this project, but the differences in signal characteristics and received level because of this azimuthal dependence were observed between the two measurement days. This azimuthal dependence was the driving factor behind the differences in measurements between the two pile driving days. There was little correlation between the penetration depth and strike energy and the received sound levels recorded so no conclusion can be drawn as to how those affected the data. The increasing decay time and decreasing kurtosis suggest that the signal was becoming less impulsive with range, but there was no clear transition point to where the signal became definitively non-impulsive. More measurements would have to be taken to further define this transition point, which would be location and source dependent.

3 Particle Velocity

Pile driving produces intense sound and associated particle motion that propagates through the water, sediment and the water-sediment interface. Both the sound levels and the particle motion can potentially impact fish and invertebrates. Acoustic pressure gradients were determined using underwater acoustic monitoring data separately collected during 1) the BIWF Phase 1 construction and 2) turbine operations. These data were used to compute acoustic particle acceleration. Particle velocity was estimated by numerically integrating the particle accelerations. The results were compared to findings and observations from review of available and relevant acoustic particle velocity literature. Findings from the construction phase data analyses were also compared to results from operational phase data analyses.

3.1 Literature Review Results

The importance of using particle velocity estimations in assessing impact of sound exposure to fishes and invertebrates has been emphasized by several researchers including Popper and Hawkins (2018). However, relative few prior studies have attempted to directly measure particle motion. A few European studies, which included both particle motion measurements and modeling, were identified during the literature review; key findings from these studies are discussed below. It should be noted that the wind turbine construction methodology have evolved considerably over the years and the units have become quieter and more efficient. Also, acoustic radiation and associated particle motion depends upon site-specific environmental conditions (bathymetry, sound speed in the water column and bottom characteristics) and the type of sub-structure (mono pile, jacket, gravity etc.). Therefore, measurements from prior studies from European locations cannot be directly compared to the BIWF measurements. But the historical data are useful in defining an approximate range of values that can be expected because of pile driving operations.

Bruns et al. (2014) measured the acoustic noise and particle velocity generated during installation (pile driving) of a wind turbine in the German North Sea. The measurements were made at different distances

from the turbine using sensors in the seabed and in the water column. **Figure 19** shows the particle velocity measured at 250 m (822.2 ft) from the turbine during one hammer strike.

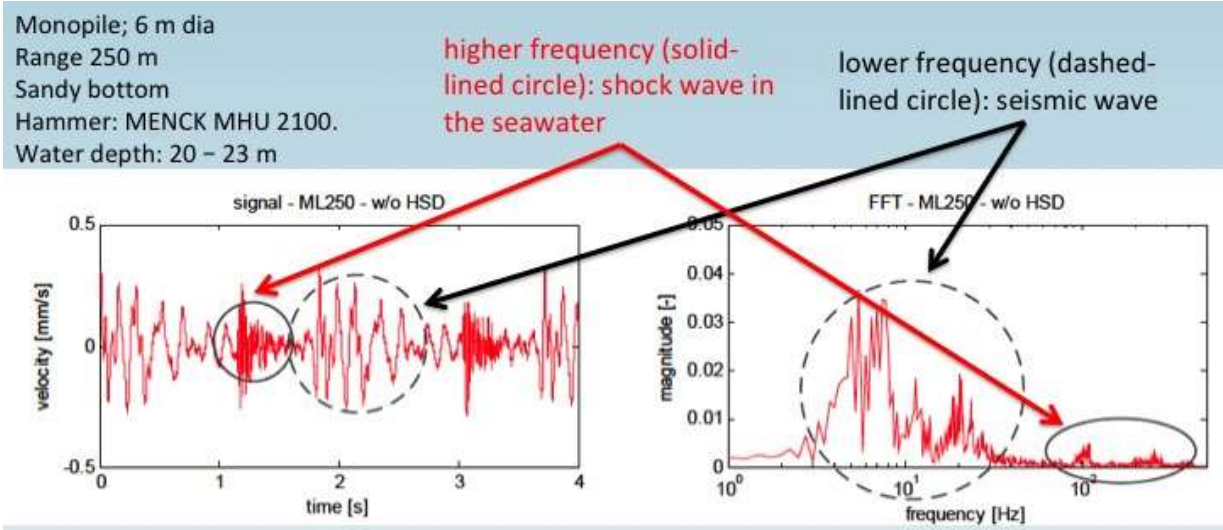

Figure 19. Time series (left panel) and spectra of vertical vibrations of the ground due to hammer impact. Low frequency interface waves (dashed circle, speed approximately 500 m/s) and high frequency water waves (continuous circle) are highlighted. (Figure from Bruns et al. 2014).

The left panel shows the time series in which the early water arrivals and the late arrivals corresponding to interface waves can be clearly seen. The right panel shows the amplitude spectrum of this signal. The water depth at the site was 20 to 23 m (65.6 to75.5 ft), the pile diameter was 6 m (XX ft) and the bottom consisted of sand (capable of supporting interface waves).

Tsouvalas and Metrikine (2016) developed a semi-analytical model to predict the structure-borne wave radiation into the sediment and water because of pile driving. The model was tested and validated using the data from the German North Sea data discussed above (Bruns et al. 2014). In **Figure 20**, the computed vertical velocity is shown on the seabed at three different ranges from the pile (left panel) together with the corresponding amplitude spectra at the same ranges (right plot). These graphs can be compared to the ones presented in **Figure 19**.

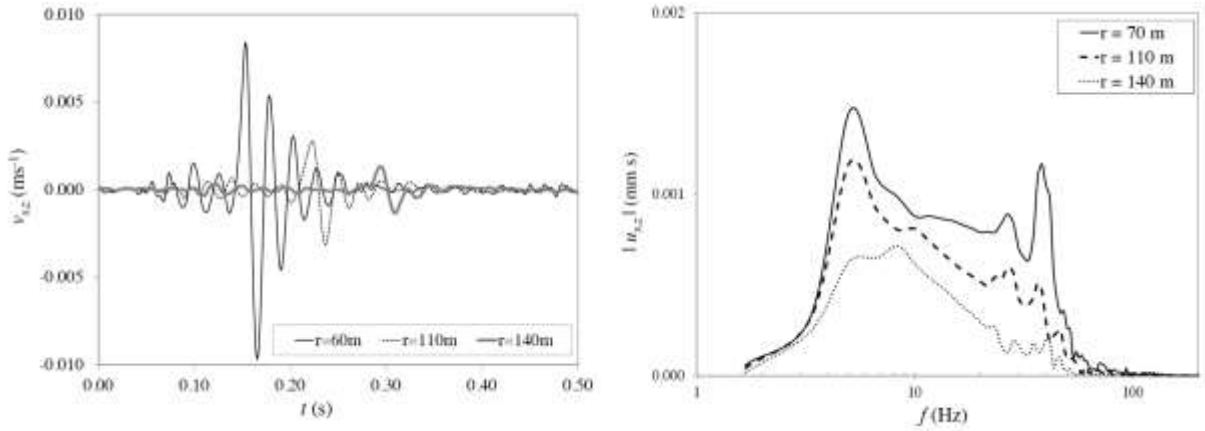

Figure 20. Time histories of the vertical velocity component at the ground surface at three different ranges (70, 110, and 140 m [229.7, 360.9, and 486.3 ft]) from the wind turbine (left panel). Right panel shows the amplitude spectra of the data shown in the left panel. (Figure adapted from Tsouvalas and Metrikine [2016]).

Based on model data comparison, Tsouvalas and Metrikine (2016) concluded that both 1) amplitude of the vertical velocity, and 2) its attenuation at increasing ranges from the pile were comparable to the measurements. It seemed that the model slightly overestimated the amplitude of the interface waves. The measured amplitudes were 2 mm/s and 1 mm/s at distances of 70 and 140 m (229.7 and 360.9 ft), respectively. The computed values were 6.1 mm/s and 1.2 mm/s at the same distances.

The amplitude spectrum of the measured vertical velocity on the surface of the ground at these locations showed that the energy carried by the interface waves is concentrated at frequencies of approximately 10 Hertz (Hz) with limited amounts of energy above 50 Hz. The model (right panel in **Figure 20**) computes energy at similar frequency ranges. In addition the model also predicted the sound pressure level (SPL) (peak) and SEL as a function of range as shown in **Figure 21**. Based on the model results the peak SPL at 50 m (164 ft) is approximately 205 dB re 1 µPa.

3.1.1 Effect of Sound Pressure and Particle Motion on Fish Hearing

Popper and Hawkins (2018) have emphasized the importance of particle motion to fishes and invertebrates and the steps that needs to be taken to improve the knowledge of its effects. They point out that when examining the potential effects of sound on fishes and invertebrates, the sensitivity of these animals to particle motion component of sound is often overlooked. They address some of the data gaps that exist currently that needs to be addressed in order to properly understand the relevance of particle motion to fishes.

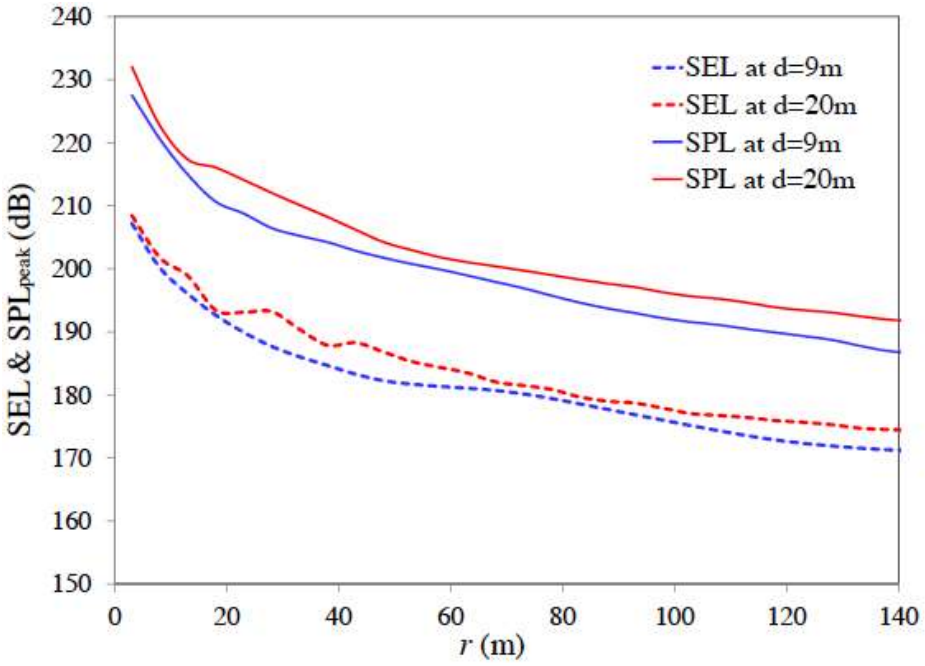

Figure 21. Peak Sound pressure level (SPLpeak) and SEL as a function of distance from the pile surface at two water depths (9 and 20 m [29.5 and 65.6 ft]). (Figure adapted from Tsouvalas and Metrikine [2016]).

There is widespread concern about the potential effects of sound on fishes, and there is a limited body of literature on the effects of exposure to sound on fishes. Papers by Popper (2006), Popper and Hastings (2009), Dahl et al. (2015), Hawkins and Popper et al. (2014) and the references cited in these papers provide an overview of the state of the research in this area.

The sensitivity of the fish to sound (and particle motion) is often expressed using audiograms. Experimental studies determine the range of frequencies (or bandwidth) that a fish can detect, and then

determine the lowest levels of the sound detected at each frequency (the 'threshold'), or lowest signal that an animal will detect (Popper and Hastings 2009). The graphic representation of the threshold as a function of frequency is called an "audiogram."

Hearing range and sensitivity varies considerably between species. Behavioral audiograms have been published for only a few species of fish (e.g., Fay 1988, Ladich and Fay 2013), and there are concerns about the usefulness of many of these. Acoustic conditions were poorly monitored in many studies and it is difficult to determine from such studies whether the fishes were responding to sound pressure or particle motion (Popper and Hawkins 2018, Rogers et al. 2016). Levels of ambient or background sound can result in the audiograms being masked so that the full hearing sensitivity of the animal cannot be determined. Auditory-evoked potentials may not fully reflect the hearing capabilities of animals and do not include signal processing by the brain (Popper et al. 2014).

There are no standards which specify the criteria for mortality, injury and behavioral changes when fishes are exposed to sound. The technical report prepared by ANSI-Accredited Standards Committee S3/SC1 (Popper et al. 2014) provides some useful sound exposure guidelines for fishes and sea turtles. The guidelines for acoustic pressure exposure specify the maximum peak levels as 213 dBpeak (fishes without a swim bladder) and 207 dBpeak (other types of fishes) to avoid mortality and have recoverable injury. The peak sound pressure levels measured in this study at 500 m (1,640.4 ft) are lower than the levels that potentially result in mortality or injury as per this guideline.

The guidelines and regulations designed to protect fishes (there are no guidelines for invertebrates) are based solely in terms of sound pressure. Virtually all experiments have only measured, and provided guidance, in terms of sound pressure. Because the high intensity sources that produce large sound pressure levels may also produce high levels of particle motion, it is possible that many of the effects seen to date are a result of exposure to particle motion, or the combination of pressure and particle motion (Popper and Hawkins 2018).

Popper and Hawkins (2018) also suggest that there is growing evidence that invertebrates and fishes may be capable of detecting sounds traveling through and on the substrate. There is a bioacoustically relevant class of waves that exist between water and its boundaries, including shear and surface waves at the water/bottom interface (Gray et al. 2016). Scholte wave amplitude decreases exponentially away from the interface. These low frequency waves have been used extensively in bottom characterization studies (Potty and Miller [2012]), Giard et al. (2013) and Potty and Miller (2018). We have made measurements of particle velocity in the water column and on the seabed to understand the contributions from wave types propagating in the water and along the seabed.

3.2 Data Collection

During BIWF Construction Phase 1, acoustic and seismic signals for particle velocity assessment were measured and recorded in October 2015 using a bottom moored geosled (HDR 2018). The sled was deployed for four weeks approximately 500 m (1,640.4 ft) from WTG 3 and WTG 4 at a depth of 26 m (85.3 ft) at 41.1110 N and 71.5225 W. It carried the following monitors:

- a four-hydrophone tetrahedral array for measurement of acoustic particle velocity in the water column
- a geophone sensor package with a three-axis geophone and a co-located low sensitivity hydrophone for the measurement of sediment motion and acoustic pressure on the seabed.

The sound pressure hydrophones had a spacing of 0.5 m (1.6 ft). In **Figure 22**, the right panel shows the surface floats for the geosled; the middle and left panel shows the geosled before deployment.

Figure 22. Images of the geosled before deployment (left and center). These two photographs show the tetrahedral array of hydrophones with a spacing of 0.5 m (1.6 ft). Photograph of the surface floats for the sled with WTG 4 in the background (right).

3.3 Results

An example spectrogram of the data collected on one of the sound pressure channels of the tetrahedral array is shown in the left panel of **Figure 23**. The x-axis for both plots is referenced to an arbitrary start time. Pile-driving signals from 25 October 2015 from the four hydrophones of the tetrahedral array are shown in the right panel.

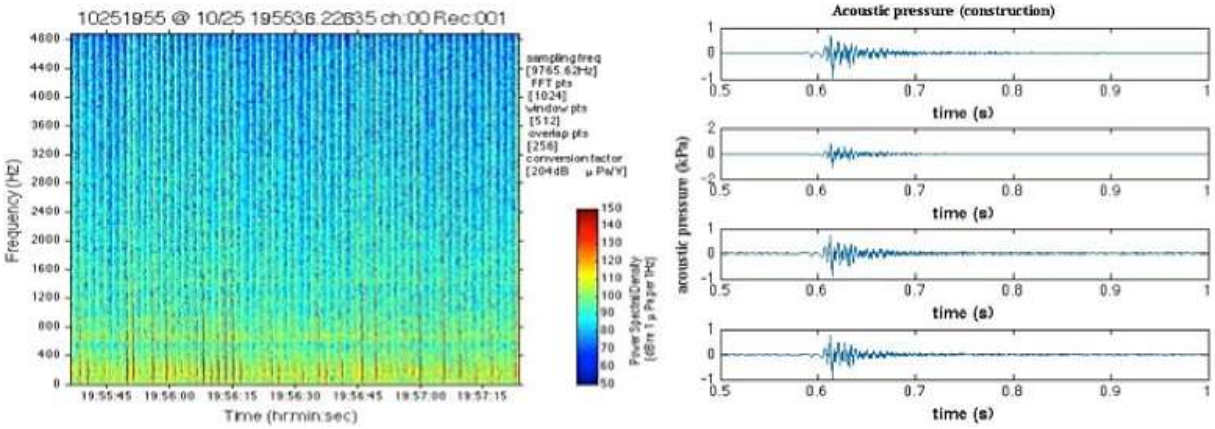

Figure 23. Spectrogram of data from a single tetrahedral array hydrophone is shown in the left panel. Right panel shows acoustic pressure signals on the four channels of the tetrahedral array.

For the hammer strike data shown in **Figure 23**, the peak-to-peak SPL at the sled was found to be approximately 185 dB relative to 1 micropascal (re 1 µPa). Using the transmission loss estimates from previous study (BOEM OCS Study 2018-029) and this SPL value at 500 m (1.640.4 ft), an approximate estimate of the peak-to-peak source level of the pile driving signal is approximately 235 dB re 1 µPa at 1 m. This value is consistent with the range of values reported in Section 4.2.4 of BOEM Report 2018-029.

The acoustic particle accelerations were computed from the gradient of the acoustic pressures using the following equation:

$$-\nabla p = \rho \frac{\partial \vec{u}}{\partial t}$$

p acoustic pressure

$\vec{u}$ acoustic particle velocity

ρ density

Particle velocity was estimated from the above equation by numerically integrating the particle accelerations. An example of the particle acceleration and velocity calculated using the hydrophone data for a single hammer strike event is shown in **Figure 24**.

An example of the data from the three-axis geophone deployed off the geosled is shown in **Figure 25**. The figure shows the particle velocity along vertical (channel 3) and two horizontal directions (channels 1 and 2, left panel) and the total (vector sum) particle velocity (right panel) generated by a single impact pile driving at a range of 500 m (1,640.4 ft) from WTG 3 and 4. These data were recorded on 25 October 2015 at approximately 2:58 UTC.

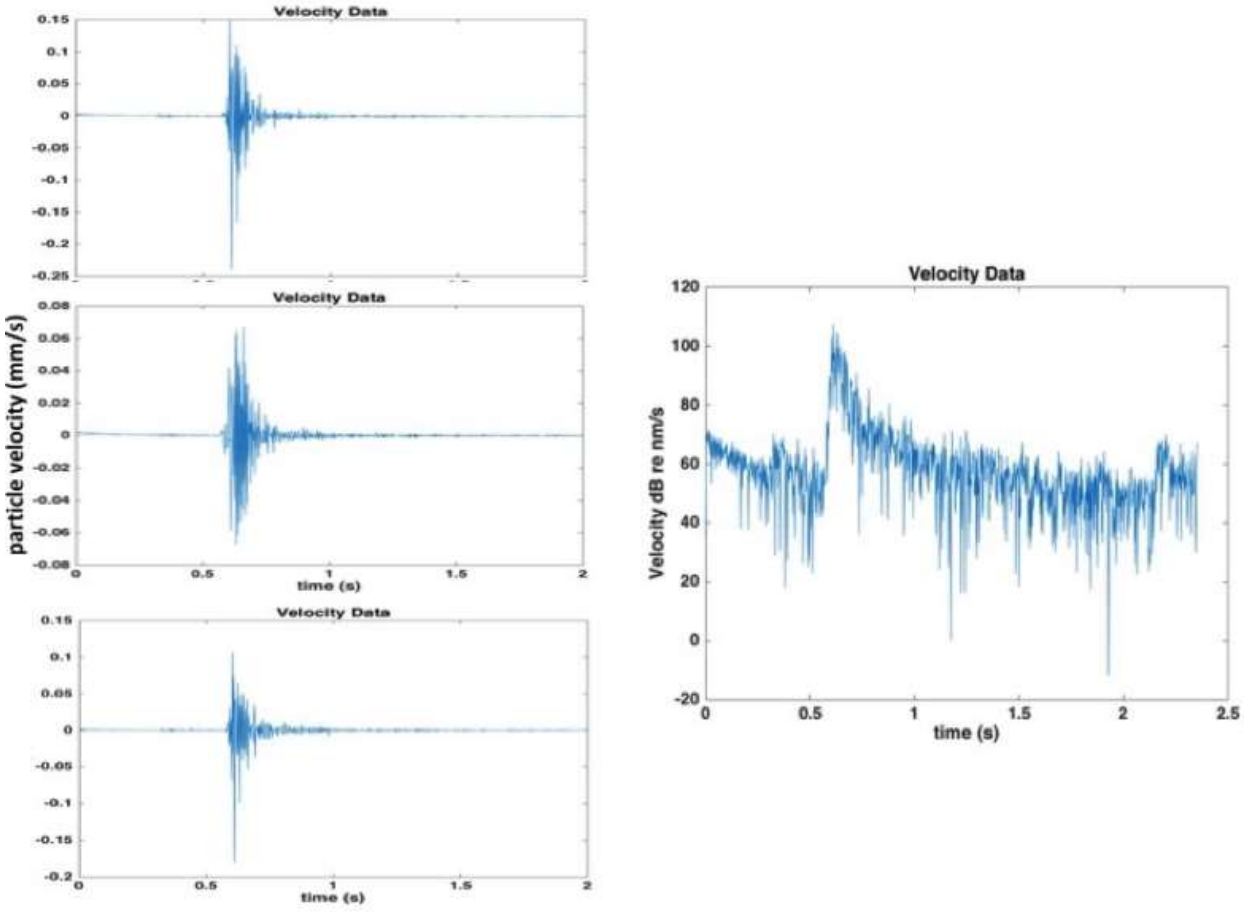

Figure 24. Particle velocity calculated from the sound pressure gradients for one hammer strike. Left panel shows the values in mm/s and the right panel shows the magnitude of the total velocity (vector sum) in dB re nm/s.

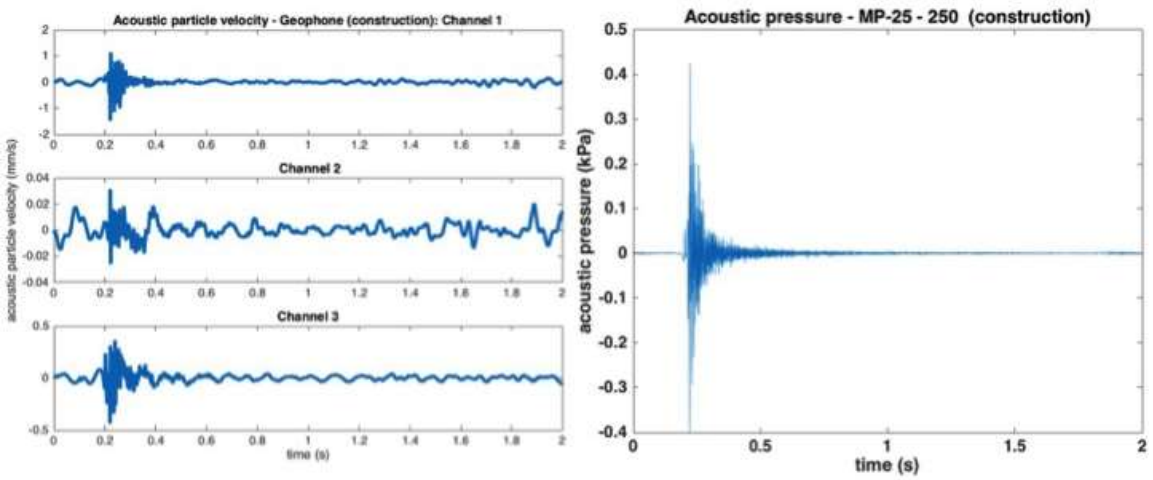

Figure 25. An example of the particle velocity data (in mm/s in three mutually perpendicular directions) from the three-axis geophone deployed off the geosled (left panel). Channels 1 and 2 are horizontal, and channel 3 is vertical. Right panel shows the acoustic pressure measured by the hydrophone co-located with the geophone.

The seismic signals from the pile driving had high signal-to-noise ratio, no clipping, and the time series has complexity that may be ascribed to the pile-driving mechanisms. The velocities are shown in mm/s and the pressure in kPa. The peak-to-peak sound pressure levels are comparable to the levels measured (described previously) in the hydrophones in the tetrahedral array. The particle velocity magnitudes are higher compared to values calculated using the tetrahedral array data.

Figure 26 shows the magnitude of the total particle velocity (vector sum) in dB re nm/s measured at the seabed using the geophone (left panel). Right panel shows the particle velocity in the water column (same units), 1 m from the seabed, calculated using the tetrahedral array data. There is an approximate 10 dB difference in peak velocities (dB re nm/s).

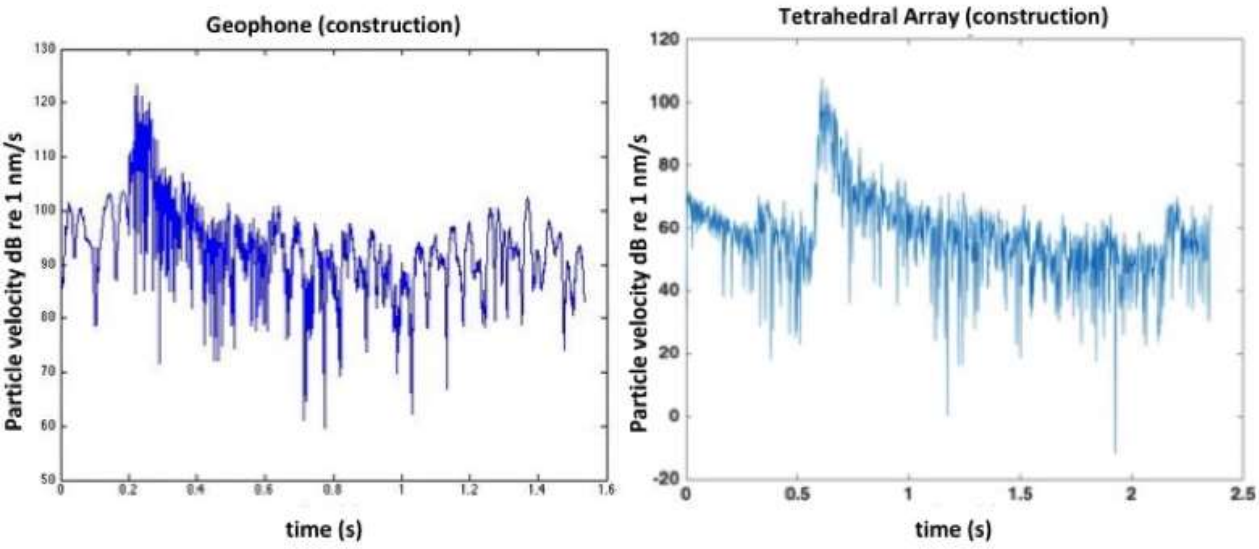

Figure 26. Magnitude of the total particle velocity (vector sum) in dB re nm/s measured by the geophone (left panel). Right panel shows the magnitude of the total velocity (vector sum) calculated from the tetrahedral array data. Note that the start times (x-axis) are arbitrary.

The spectral distribution of the energy from the geophone and co-located hydrophone measurements is shown in **Figure 27**. The difference in frequency content between the hydrophone and geophone response is apparent in the figure. This indicates that the response of the geophone and hydrophone are possibly dominated by different wave types. The geophones measure the ground motions whereas the tetrahedral array estimates the particle velocities above the ground in the water column (approximately 1 m from the bottom). The single sound pressure hydrophone measures the compressional waves in the water whereas the geophone measures the motion generated by shear and interface (Scholte) waves in addition to the motion associated with compressional waves. Particle motions produced by interface waves (Scholte waves) are likely to dominate the geophone signal. These motions decay exponentially (Dosso and Brooke 1995) away from the interface (seabed).

Previous studies have shown that signals recorded on seismic sensors on the seabed are found to be more complicated (consisting of different wave types) than on co-located hydrophones (Bibee 2011). The differences were attributed to the response of the seismometer sensors to shear waves in the seabed and interface waves at the water-sediment boundary. It was hypothesized that the particle velocities measured at the seabed and in the water column can be different because shear and interface waves can contribute (in addition to compressional waves) in the sediment medium. The particle velocity measured in the water column likely is dominated by that because of compressional waves. There will be contributions from the Scholte waves in the water column, but they will be significantly fewer than those in the seabed because the Scholte wave amplitude decays exponentially away from the interface.

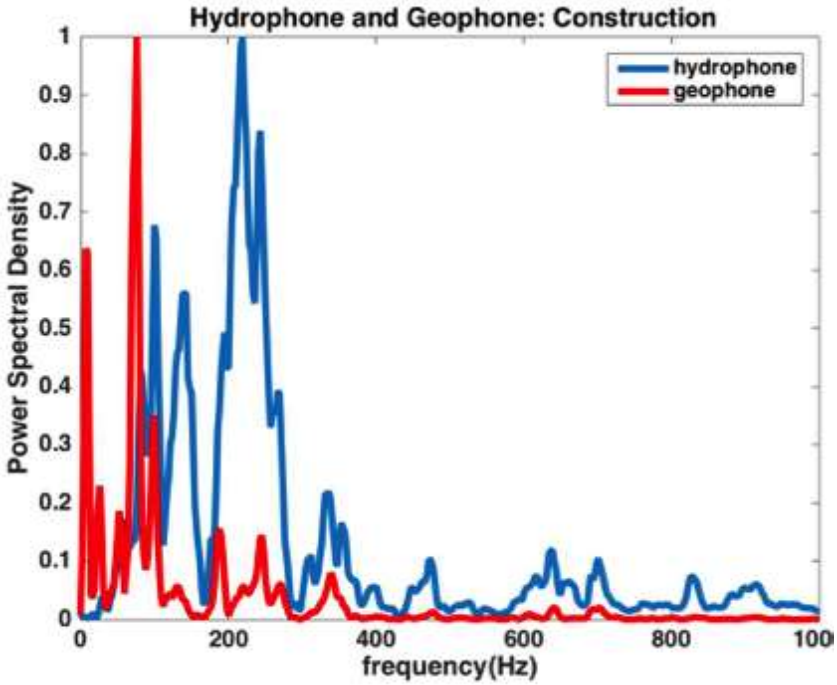

Figure 27. Spectra of the particle velocity (red) and acoustic pressure (blue) measured on the seabed using the co-located geophone and hydrophone. Note that the amplitudes are normalized using the peak values. The difference in frequency content between the hydrophone and geophone response is apparent.

Figure 28 compares particle accelerations calculated from the measurements made during the pile driving with published behavioral audiograms for some species for which there are particle motion hearing data. The behavioral audiograms shown in the figure are from: Atlantic salmon (*Salmo salar*, Hawkins and Johnstone 1978), plaice (*Pleuronectes platessa*) and dab (*Limanda limanda*, Chapman and Sand 1974), and Atlantic cod (*Gadus morhua*, Chapman and Hawkins 1973). The left panel shows the frequency

distribution of particle acceleration calculated using the tetrahedral array data and the right panel shows the geophone data. Particle accelerations are shown in dB re 1 μm/s^2.

Particle acceleration levels in water (left panel in **Figure 28**) are slightly above the behavioral sensitivity for the fishes considered in the frequency range 30 to 300 Hz. Hence fishes may barely 'detect' the particle motion during construction at 500 m (1,640.4 ft) range. Note that the particle velocity levels measured on the seabed (right panel in **Figure 28**) are well above the behavioral sensitivity for all fishes shown in the figure up to a frequency of approximately 300 Hz. Based on the data, it appears that the impact of construction may be more pronounced on fishes whose habitat is close to the seabed and sensitive to particle motion compared to fishes who spend most of their time in the water away from the seabed. It should be noted that fish in mid-water like the herring may be affected by the sound pressure rather than the particle motion.

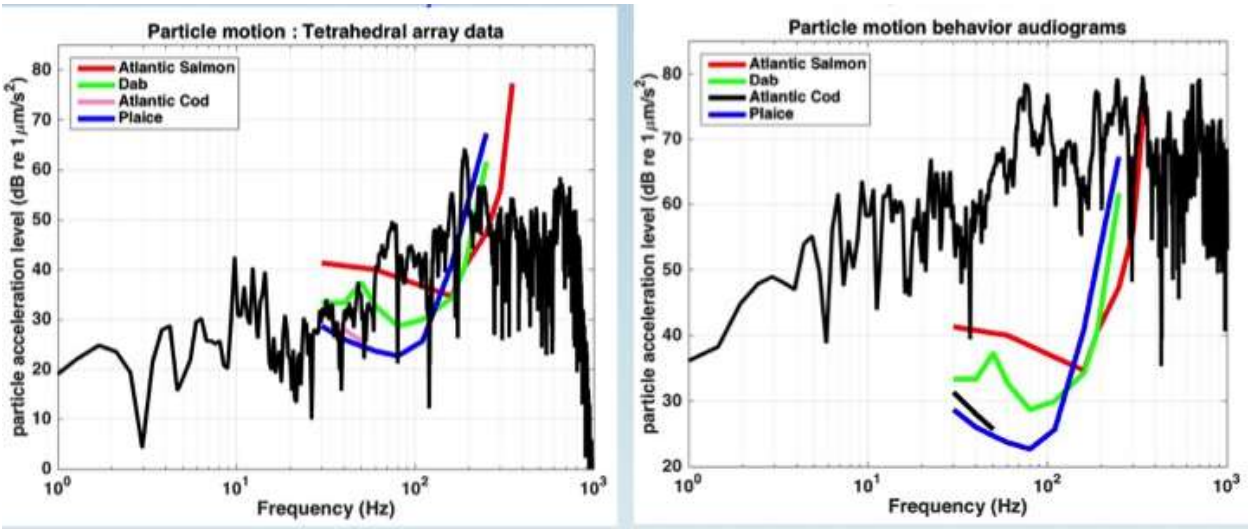

Figure 28. Spectra of the particle acceleration (black) in the water column estimated using the tetrahedral array (left panel) close to the seabed (approximately 1 m [3.3 ft]) and measured on the seabed using the geophone (right panel). Both the measurements were made in the 500 m (1,640.4 ft) range. Particle acceleration compared with behavioral audiograms of Atlantic salmon (Hawkins and Johnstone 1978), Plaice and Dab (Chapman and Sand 1974), Atlantic cod (Chapman and Hawkins 1973). The left panel shows the frequency distribution of particle acceleration calculated using the tetrahedral array data and the right panel shows the geophone data. Particle accelerations are shown in dB re 1 μm/s^2.

The peak particle velocity measured by other investigators during the pile driving range from 0.075 m/s to 0.225 m/s at 500 m (1,640.4 ft) from the turbine (HDR 2018). This translates into a range of 98 dB re 1 nm/s to 110 dB re 1 nm/s, which agrees well with the previously reported tetrahedral array measurements (HDR 2018).

The particle velocity levels on the seabed are much higher during construction when compared to the levels measured during operation as shown in **Figure 29**[3] . The peak velocity levels (re 1 nm/s) on the seabed during construction and operations are approximately equal to 120 dB and 60 dB, respectively.

[3] See accompanying report entitled "*Field Observations during Wind Turbine Operations at the Block Island Wind Farm, Rhode Island*" for in-depth discussion of particle velocity measurements and analyses conducted using underwater sound monitoring data collected during wind turbine operations.

The amplitude spectra of the data collected during construction and operation of the wind turbine is compared in **Figure 30**. The dominance of seismic waves (low frequency) in the geophone and hydrophone during the operation of the wind farm is clear in Figure 30 (right panel). The compressional waves through the water column (high frequency) dominate the hydrophone signals during construction (left panel in **Figure 30**).

Figure 31 compares acoustic pressure (as a function of frequency) measured on the geosled during BIWF construction (black curve in **Figure 31**) versus operation (red curve). It should be noted that the measurement locations were different during these two measurements. During construction, the geosled was deployed at 500 m (1,640 ft), whereas for the monitoring conducted during the operational phase, it was deployed at 50 m (328.1 ft). Comparison of the acoustic pressure at the same range would have been ideal, but restrictions during construction to close access prevented this. The peak construction pressure amplitude is approximately 1000 times higher than the peak operational amplitude. This amounts to 60 dB differences in sound pressure levels between the construction and operational measurements. At 500 m the operational pressure level is likely smaller. This result reinforces one of the major conclusions of this project; i.e., the sound pressure levels produced during the operational phase is small compared to construction phase.

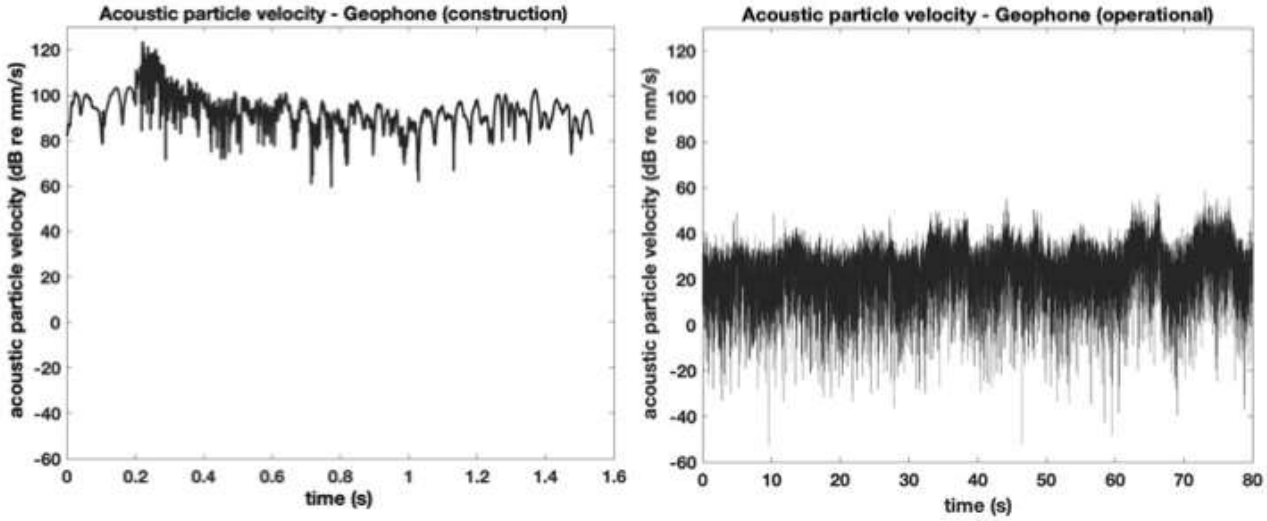

Figure 29. The particle velocity levels on the geophone on the seabed during construction (left panel) are compared to the levels measured during operation (right panel).

The time domain signal corresponding to the data from construction and operation are shown in **Figure 32**. The peak sound pressure level during construction (185 dB re 1 µPa) at 500 m compares well with the Tsouvalas and Metrikine (2016) model results. They predicted, based on model results, peak SPL of 190 dB re 1 µPa at 144 m (472.5 ft) from a turbine (**Figure 31**).

The impact of the acoustic pressure on fish behavior can be assessed when the behavior audiograms are available. Behavior audiograms of some of the fishes are shown **Figure 33**. The SPL values measured at 500 m (1,640 ft) range during construction are much higher than the behavior thresholds of Atlantic Cod (*Gadus morhua*, Chapman and Hawkins 1973), Common Carp *(Cyprinus carpio,* Popper 1972), Soldier fish (*Myripristus*, Coombs and Popper 1979) and Hardhead catfish (*Arius felis*, Popper and Tavolga 1981) (**Figure 33**). The peak values measured during turbine operations at 50 m (49.2 ft) (red curve in **Figure 31**) are higher than the behavior thresholds of these species but not as high as the values measured during construction.

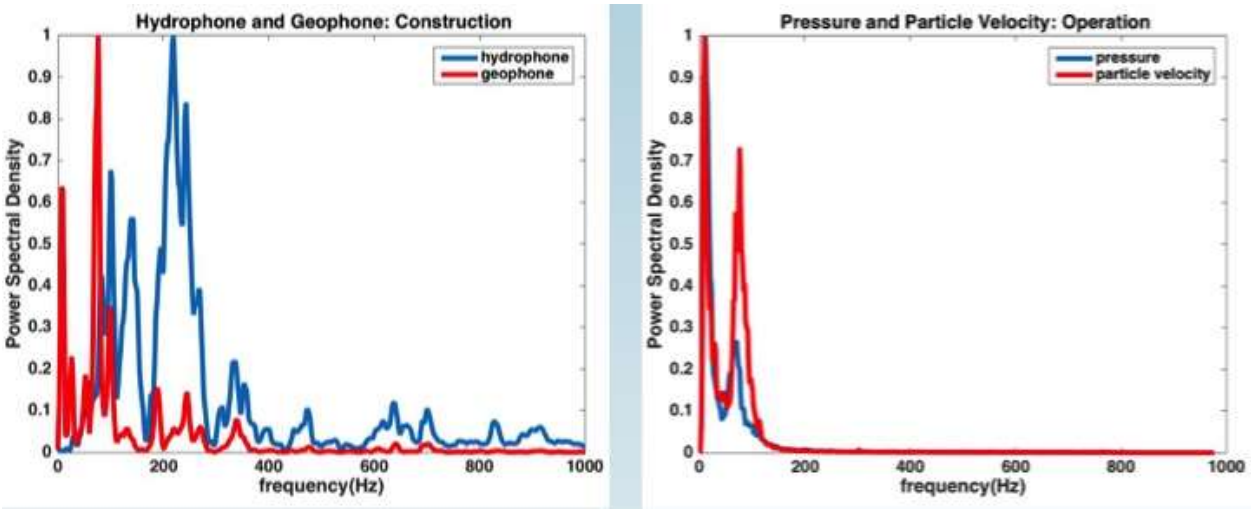

Figure 30. Comparison of the spectra of the hydrophone (blue) and geophone (red) signals measured during construction (left panel) and operation (right panel) of the wind turbine. Note the similarity between the geophone and hydrophone frequencies during operation.

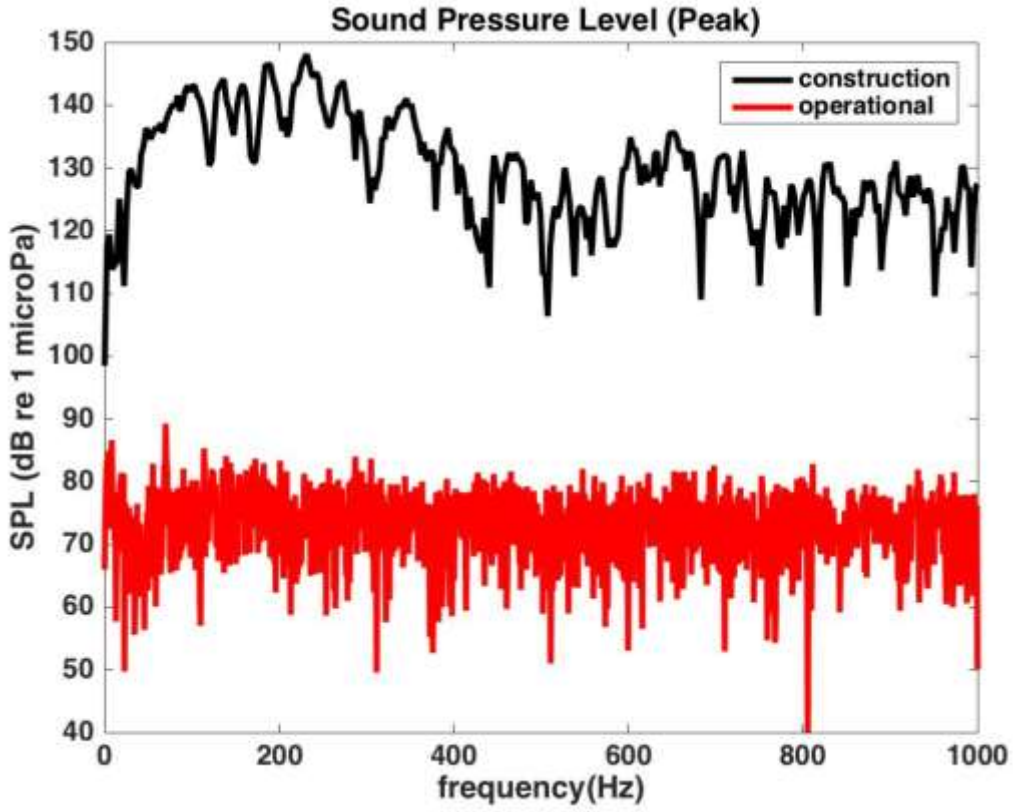

Figure 31. The sound pressure levels (kPa) measured during construction and operation of the wind farm. The levels during construction (black curve) was measured at a range of 500 m (1,640.4 ft). Operational noise (red curve) was measured at 50 m (49.2 ft) from the tower WTG 5.

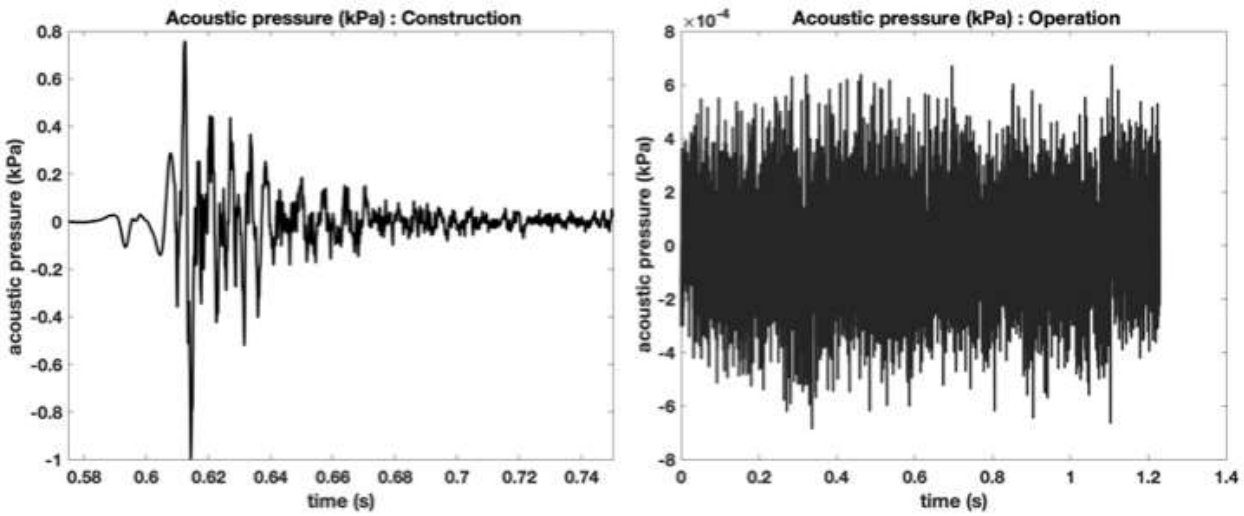

Figure 32. The sound pressure (kPa) measured during construction and operation of the wind farm. The levels during construction (left panel) was measured at a range of 500 m 1,640.4 ft). Operational noise (right panel) was measured at 50 m (49.2 ft) from the tower WTG 5. The amplitude spectra of these signals are shown in Figure 29. (Note the difference in scales in both figures; the peak construction amplitude is approximately 1,000 times higher than the peak operational amplitude. This amounts to 60 dB difference in sound pressure levels (as shown in Figure 29) between the construction and operational measurements.

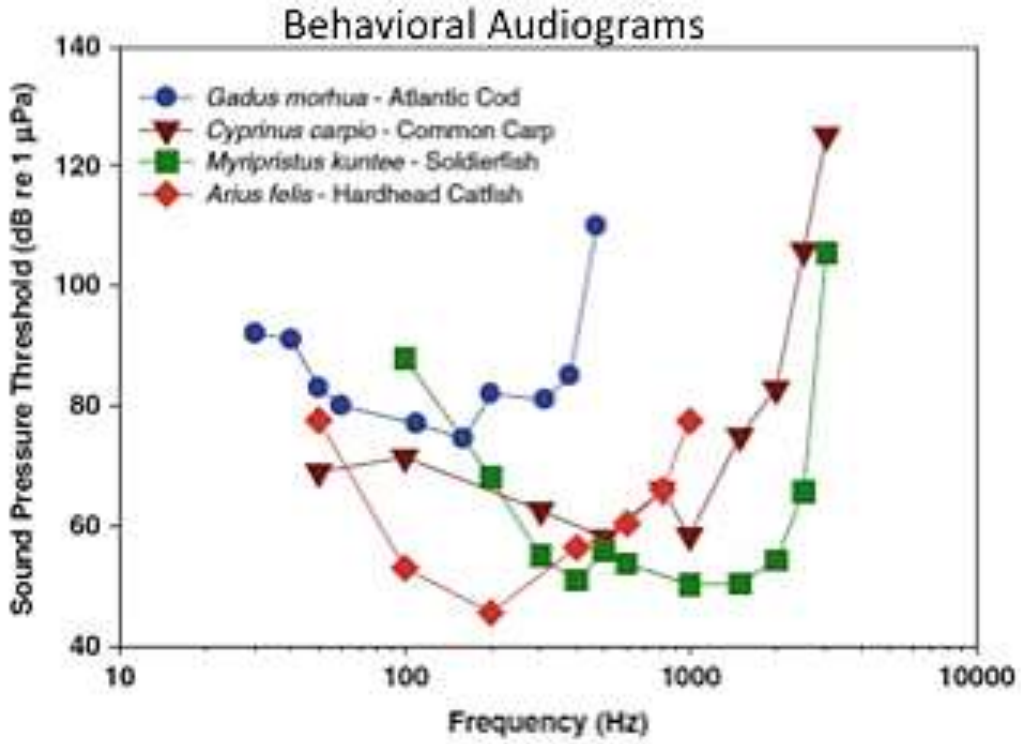

Figure 33. Sound pressure behavior audiograms of four species that are sound pressure sensitive in the frequency region 10 Hz to 10 kilohertz.

3.3.1 Modeling of interface wave motion

In this study, an algorithm based on the reflection-transmission coefficient approach developed by Hisada (1994) and Lai (1998) was used to calculate the particle motion. This method is based on calculating the reflection and transmission coefficients and then using them to construct the layer reflection and transmission matrices. They are then assembled into a global reflection and transmission matrix of the layered system. This results in an iterative algorithm for constructing the dispersion relationship.

Figure 34 shows the ratio of spectral amplitudes of the horizontal to vertical components (H/V ratio) as a function of frequency measured at 500 m (1,640 ft) from the wind farm. The different curves shown in **Figure 34** show the data from multiple hammer impacts. It can be seen from the figure that the peaks of the H/V curve are robust and consistent on all hammer impact events. There seems to be some spread in the peak at approximately 48 Hz.

The black dashed curve in **Figure 34** shows the mean H/V ratio, which was calculated based on a bottom model with an assumed shear wave speed profile in the sediment. Borehole data from the site was used to create this shear speed profile. Surface wave model based on the Hisada-Lix algorithm was used to predict the 3-D particle velocity field and to calculate the H/V ratio based on this shear speed profile in the sediment.

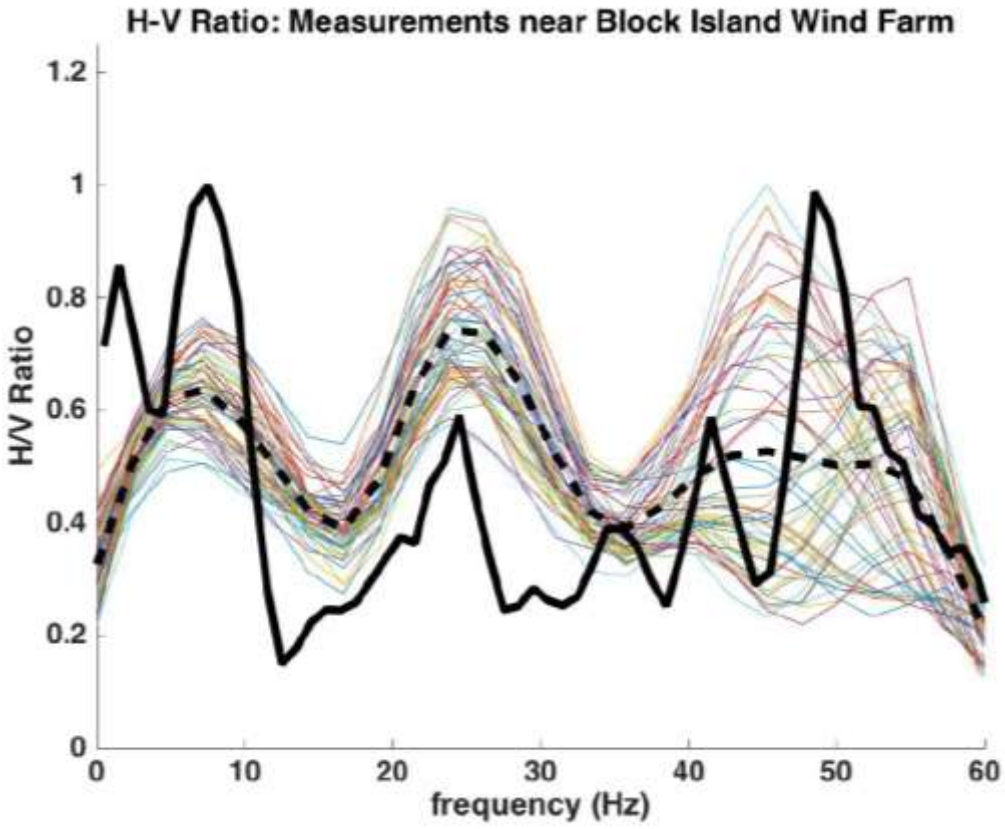

Figure 34. Ratio of the horizontal to vertical particle motion. Data from a number of time segments shown indicates consistent peaks at 7.5 and 25 Hz. The peak at 48 Hz is broader compared to the other two. The black dashed line is the mean H-V ratio curve. The black continuous curve is the theoretical prediction based on a bottom model as shown in Figure 5.

3.4 Discussion and Conclusions

Particle acceleration data calculated from underwater acoustic measurements made during construction Phase 1 pile driving events were compared with published behavioral audiograms for four fish species, namely, the Atlantic salmon (*S. salar*) , plaice (*P. platessa*) , dab (*L. limanda*), and Atlantic cod (*G. morhua*). The comparison indicated that particle acceleration levels in water are slightly above the behavioral sensitivity in the frequency range 30 to 300 Hz. This suggests that these fish may barely 'detect' the particle motion during construction at 500 m (1,640.4 ft) range.

The particle velocity levels measured on the seabed were well above the behavioral sensitivity for the four fish species up to a frequency of approximately 300 Hz. This suggests that potential impacts from construction pile driving may be more pronounced on demersal (bottom-dwelling) fishes than pelagic species, which spend most of their time in the water column and away from the seabed. It is possible that pelagic fishes like the herring may be affected more by the sound pressure rather than the particle motion. Overall, particle velocity measurement estimations generally agreed with values reported in literature.

Comparison of seabed particle velocity estimations between BIWF construction and operations phase indicated that the peak velocity levels (re 1 nm/s) on the seabed recorded during turbine operations were considerably lower (60 dB) when compared to the construction phase (120 dB).

4 3-D Underwater Sound Propagation Modeling[4]

The BIWF Phase 1 construction underwater acoustic monitoring data were used to set up a 3-D underwater sound propagation model to extend the sound propagation predictions beyond the coverage of the in-situ listening measurements. This 3-D modeling was an innovative state-of-the-art effort to provide data for improving understanding of underwater propagation of sounds that radiate with an azimuthal dependence.

Unlike in Europe where the majority of the offshore wind turbines have monopile foundations, the BIWF turbine foundations consist of a jacket structure, which is tailored to accommodate the complex aerodynamic and hydrodynamic loading of deep waters. The four legs of the jacket structure are raked at an angle of 13.27° to the vertical (**Figure 3**). The BIWF raked foundation design along with the complicated bathymetry, bottom properties and oceanography presented unique challenges that had to be addressed during the model setup. Two parallel modeling approaches were adopted:

1. A **finite element modeling** approach was used for 3-D source characterization of the raked steel pile in air, water and sediments.

2. A **3-D Parabolic Equation model** was used to simulate underwater acoustic propagation of sound originating from the pile driving.

For the finite element modeling approach, the RODEO Team is coordinating with Wilkes and Gavrilov (2017), who had previously reported on a modeling of a similar raked pile configuration. These analyses are still on-going and interpretation of model simulation output will be presented in future technical publications. Results and conclusions from the 3-D Parabolic Equation modeling are presented and discussed below.

[4]The information presented in the section has been accepted for publication in the JASA Express Letters in 2019. The citation for the paper is: Lin,Y.-T., A.E. Newhall, J.H. Miller, G.R. Potty, and K.J. Vigness-Raposa. A three-dimensional underwater sound propagation model for predicting the impacts of offshore wind turbine construction and operation.

4.1 Underwater acoustic propagation modeling using the 3-D Parabolic Equation Model

This type of modeling has never been attempted before for the BIWF environment, which is characterized by complicated 3-D oceanography, bathymetry and geology. The model utilized an accurate numerical solution scheme to solve the 3-D Helmholtz wave equation with realistic ocean environmental information inputs. The following external components are integrated into the model setup:

- High resolution bathymetric data are from the 3 arc-second U.S. Coastal Relief Model with a 100 m (328 ft) horizontal resolution (**Figure 35**).

- Environmental monitoring data (water temperature, salinity and currents) extracted from the Regional Ocean Modeling System ESPreSSO (Experimental System for Predicting Shelf and Slope Optics) model covering the Mid-Atlantic Bight with a 5 km (3.1 mi) horizontal resolution and 36 terrain-following vertical levels (**Figure 35**). The Regional Ocean Modeling System ESPreSSO model is a data-assimilated model, and it captures spatial and temporal variations of physical oceanographic conditions. This improves the prediction of the acoustical variability.

The model was validated with a set of transmission loss (TL) data collected during the BIWF environmental monitoring. Model simulation output were used to evaluate the seasonal variability of the underwater sound propagation condition in the BIWF Project Area. Significant steps from the modeling and key observations from the data analysis are discussed below.

4.2 Model Description and Validation

The model utilizes the parabolic-equation approximation, which has long been recognized as one of the most efficient and effective numerical methods to predict sound propagation in complex environments. The advantage of this method is due to the fact that it converts the Helmholtz wave equation of elliptic type to a one-way wave equation of parabolic type. This enables efficient marching solution algorithms for solving the boundary value problem posed by the Helmholtz equation. This can greatly reduce the computational resources for modeling 3-D sound propagation.

An acoustic signal playback experiment was conducted in December 2016 to collect a set of acoustic transmission data for validating the 3-D sound propagation model (**Figure 36**). The data were a set of broadband signals transmitted from a source towed by the Woods Hole Oceanographic Institute's R/V *Tioga* (the work vessel for mooring deployment) and received by a fixed Several Hydrophone Receiving Unit (SHRU) array. A time series of received signals is plotted as a stacked diagram with the vertical axis representing the transmitting time, which can also be converted to the source-to-receiver distance (S2R) as the ship was moving towards the hydrophone array. The horizontal axis of the signal stacked diagram is the reduced arrival time calculated by subtracting the nominal travel time S2R/1490 sec from the actual travel time; this is to align the received signals, so one can see the change of the received pulses as a function of the transmitting time or the source-to-receiver distance.

Figure 37 shows the comparison of the signal data and model. The model is in general agreement with the data especially it captures the pulse truncating time at closer source-to-receiver ranges less than 3,000 m (9,842.5 ft). This in fact indicates that the model produces a total reflection angle at the bottom agreeing with the real value. The model also produces the observed rate of change in the pulse arrival time as a function of S2R. One data feature the model does not capture is the attenuation of later arrivals at long ranges. This is because the model does not take into account the spatial variation of bottom acoustic properties, which need more resources to completely collect. In summary, the model is validated by comparing to a set of transmission data. We can then use the model to investigate the underwater sound propagation at BIWF and its temporal and spatial variability.

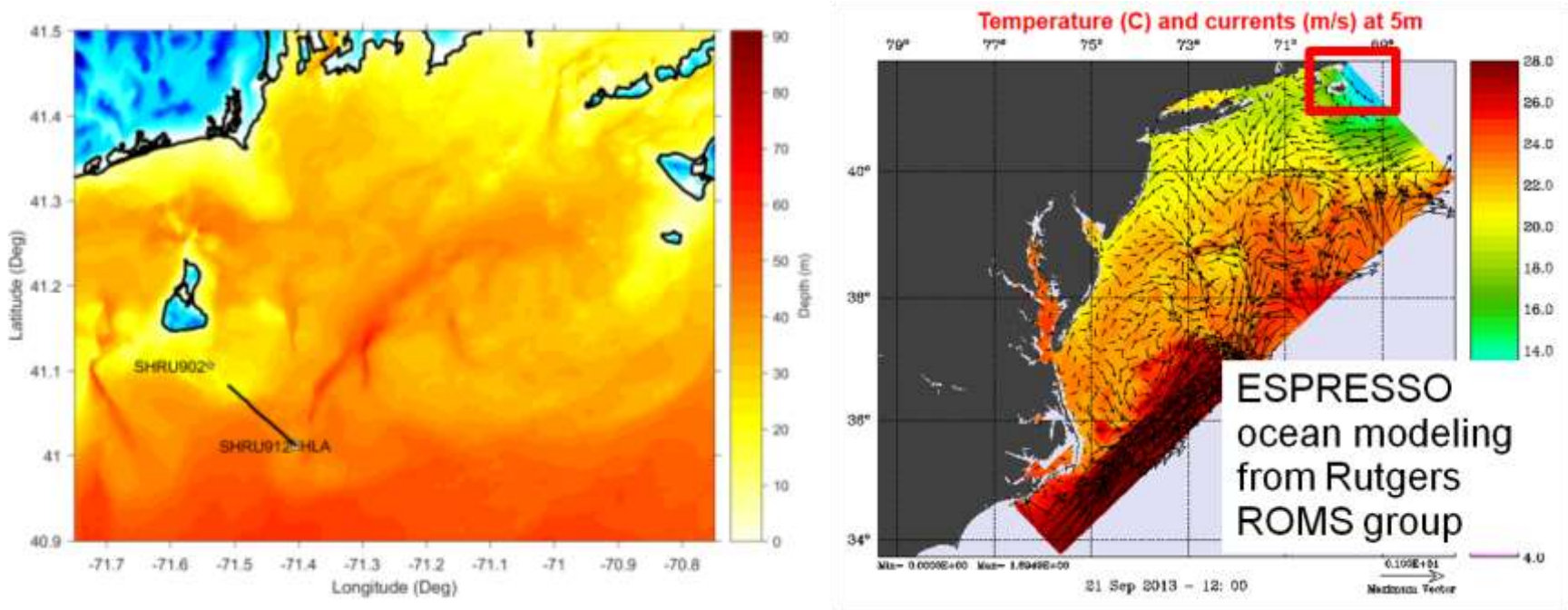

Figure 35. The BIWF underwater acoustics model incorporates the 3 arc-second U.S. Coastal Relief Model shown in the left panel and the RMOS ESPreSSO model shown in the right panel.

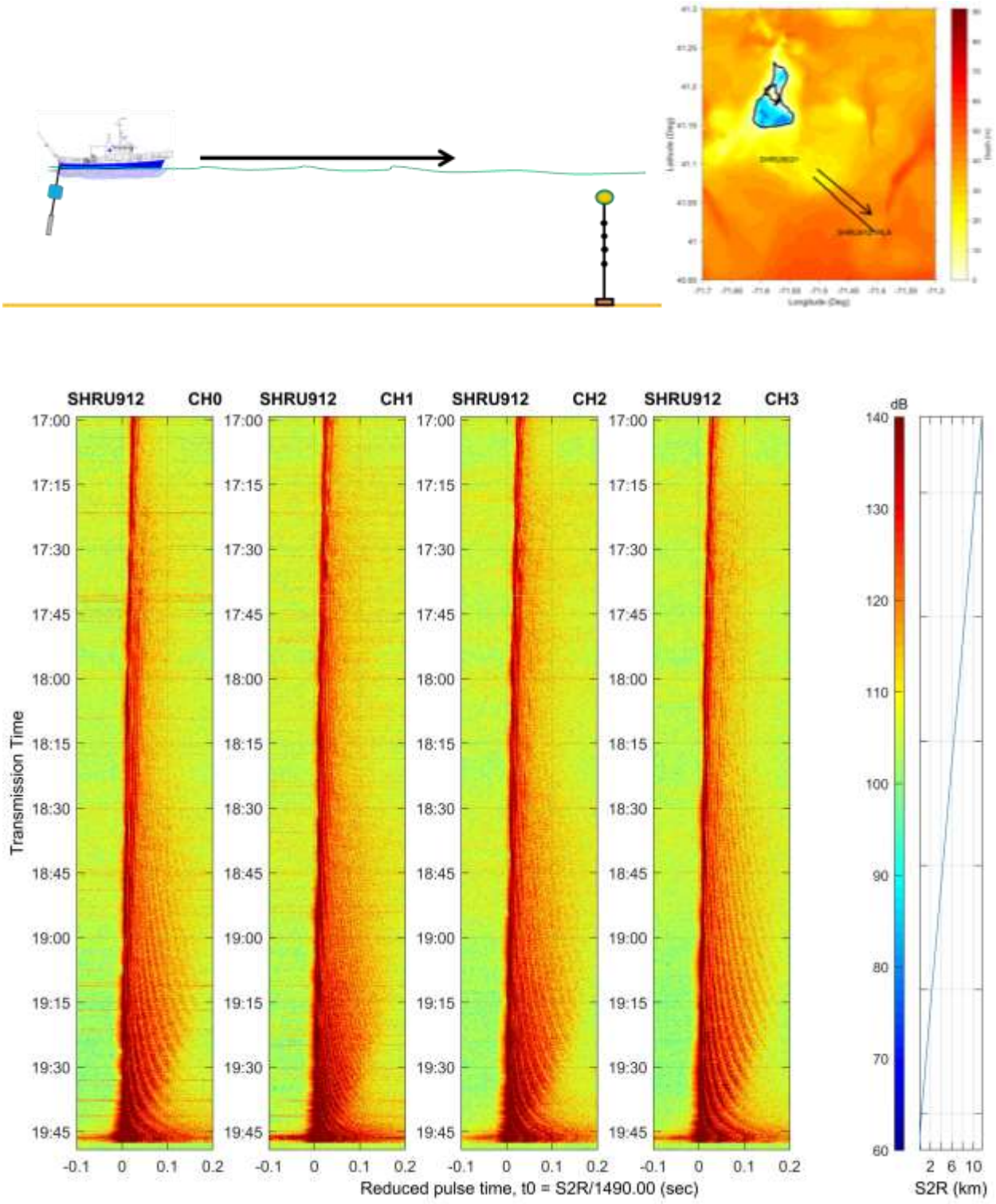

Figure 36. The playback experiment conducted during the hydrophone array deployment cruise. The source was towed by R/V *Tioga* and continuously transmitted broadband signals. The vessel was moving towards a fixed SHRU hydrophone array, as shown in the upper right panel. The received signals shown in the lower four panels were used to validate the sound propagation model.

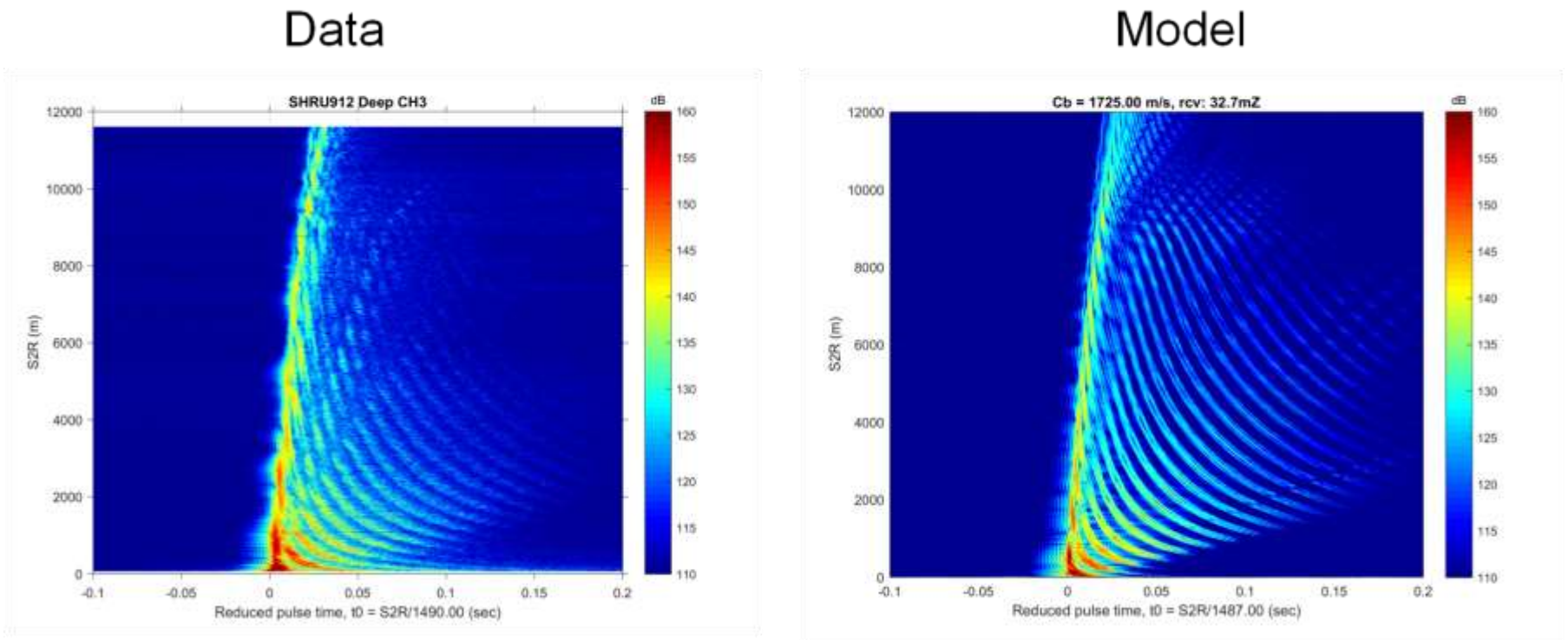

Figure 37. Comparison of acoustic transmission data and model.

4.3 Underwater Sound Propagation Analyses

Temporal (seasonal) and spatial variability of sound propagation conditions is identified in the integrated acoustic and oceanographic model. **Figures 38** to **41** show 3-D sound propagation in four different seasons. In each panel, three plots are shown. The left plot presents the model domain and also the bathymetry. The upper right plot shows the surface temperature, and one can clearly observe changes depending on the season. The lower right plot shows the transmission loss contour. Taking the 70 dB transmission loss as a reference, the propagation conditions in the fall and winter are better than in the summer, as expected from the analysis of reflection loss at the bottom presented in Section 2. To iterate the point, the underlying physics is explained again.

In the fall and winter, the water temperature is nearly constant from the sea surface to the seabed, which produces an iso-velocity condition and more omni-directional propagation, in contrast to downward refracting in summer time. Hence, the fall and winter has less bottom reflection loss. In addition, colder water temperature causes lower water sound speed, which increases the acoustic impedance at the seabed. So, the total reflection angle from the bottom becomes greater compared to summer time. This eventually enhances long-distance propagation of underwater sound as verified by the 3-D sound propagation model results.

Data recorded by two hydrophone arrays on 25 October 2015 (**Figure 42**) during BIWF Phase 1 construction pile driving , one at 500 m (1,640 ft) away from the pile being driven and the other at 15 km (9.3 mi) away (HDR 2018) was used in the 3-D underwater sound propagation model to simulate pile driving sound propagation. In the model, the close range pile sound was conservatively (underestimated) assumed to be the source signal, and a line source mimicking the driving sound radiating from the pile was also assumed. The model signal at 15 km (9.3 mi) is also shown in **Figure 42** to compare with the measured data. The model waveform is in agreement with the data, showing a dispersed waveform. However, the signal level at 15 km (9.3 mi) in the model was 3 dB less than the data, and this difference may be due to the underestimated model source level.

Seasonal variability of pile driving sound was analyzed. As shown in **Figure 43**, if the piling was in September when there was a thermocline causing a downward refracting propagation condition, the sound level at long ranges would be a couple of dB less. This is because the transmission loss in summer is higher as shown in the previous simulation study (**Figure 38**). However, the kurtosis of the propagating sound decays slower at shorter ranges to the pile.

This has an important implication for marine mammals. Because kurtosis (the fourth standardized moment) measures infrequent but sudden-peaky loud levels, slowly decaying kurtosis indicates possible harmful loud levels. Hence, there are two competing propagation factors in summer: the sound level decays faster compared to the winter time, but kurtosis decays slower. Future work is required to investigate marine mammal mitigation distance with considerations on both sound level and kurtosis and a balance between these two factors.

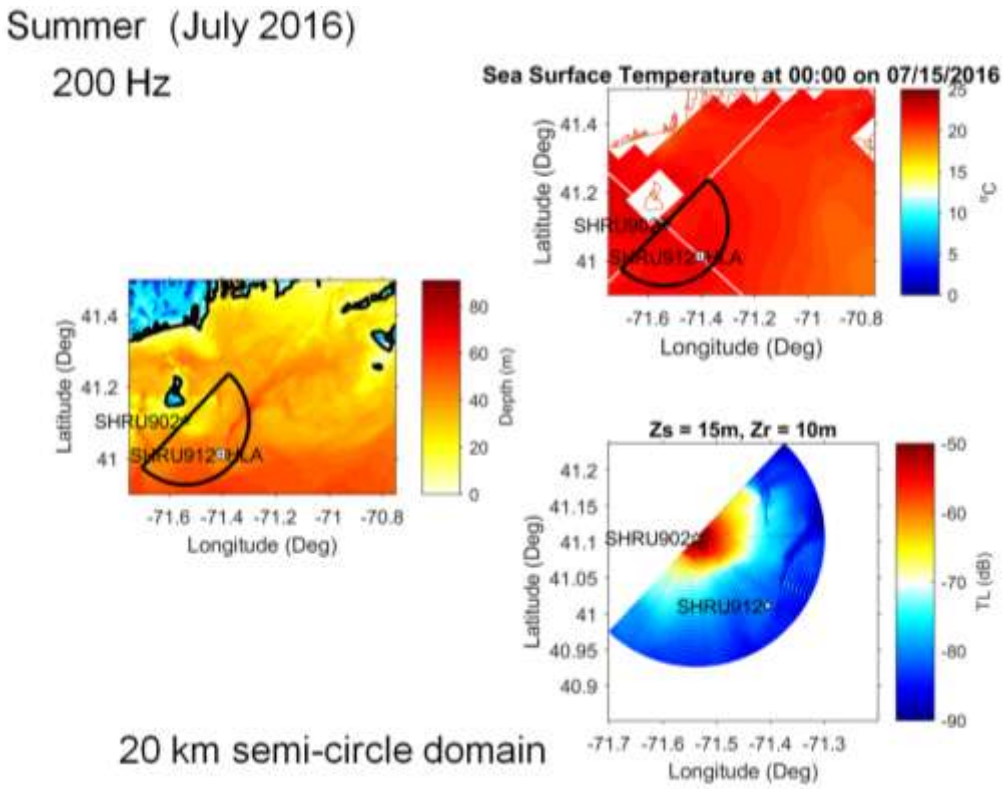

Figure 38. Seasonal variability of underwater sound propagation at BIWF (Summer 2016).

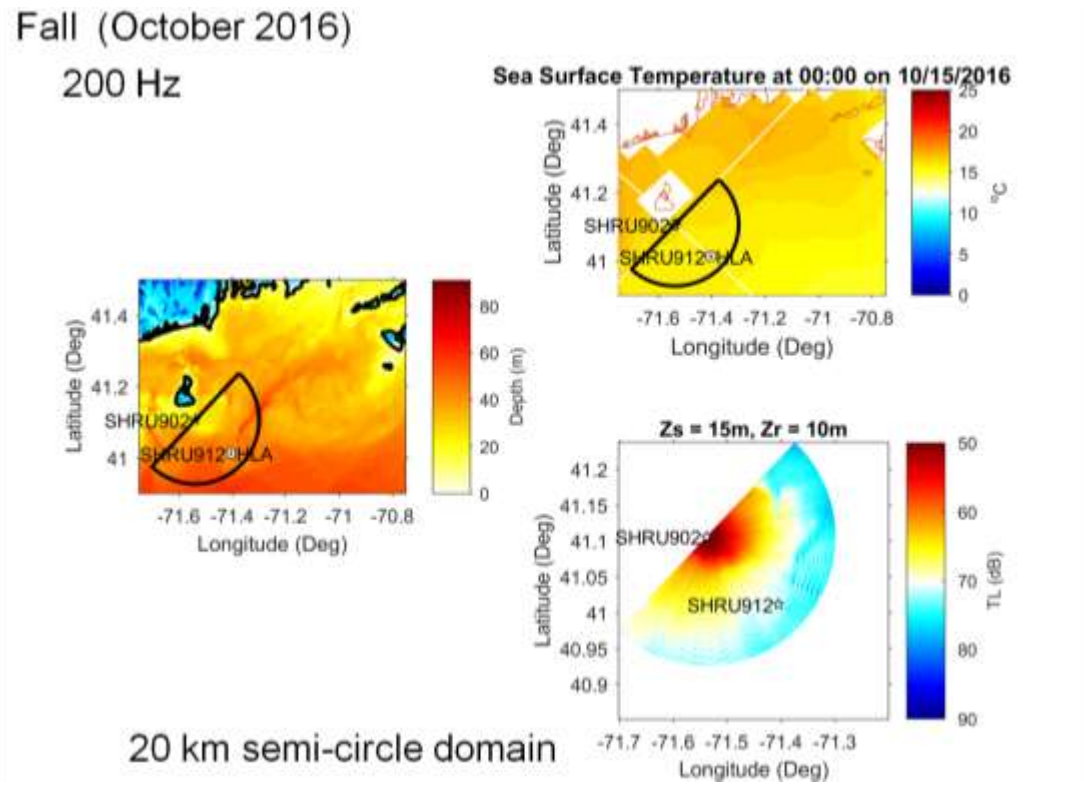

Figure 39. Seasonal variability of underwater sound propagation at BIWF (Fall 2016).

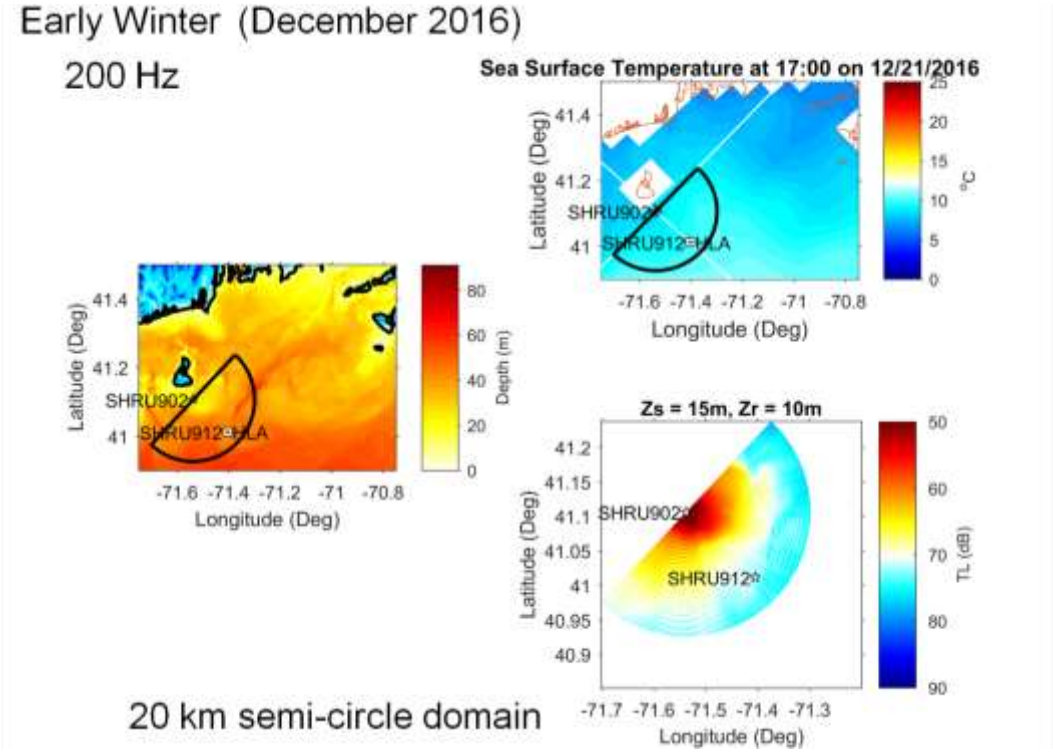

Figure 40. Seasonal variability of underwater sound propagation at BIWF (Early Winter 2016).

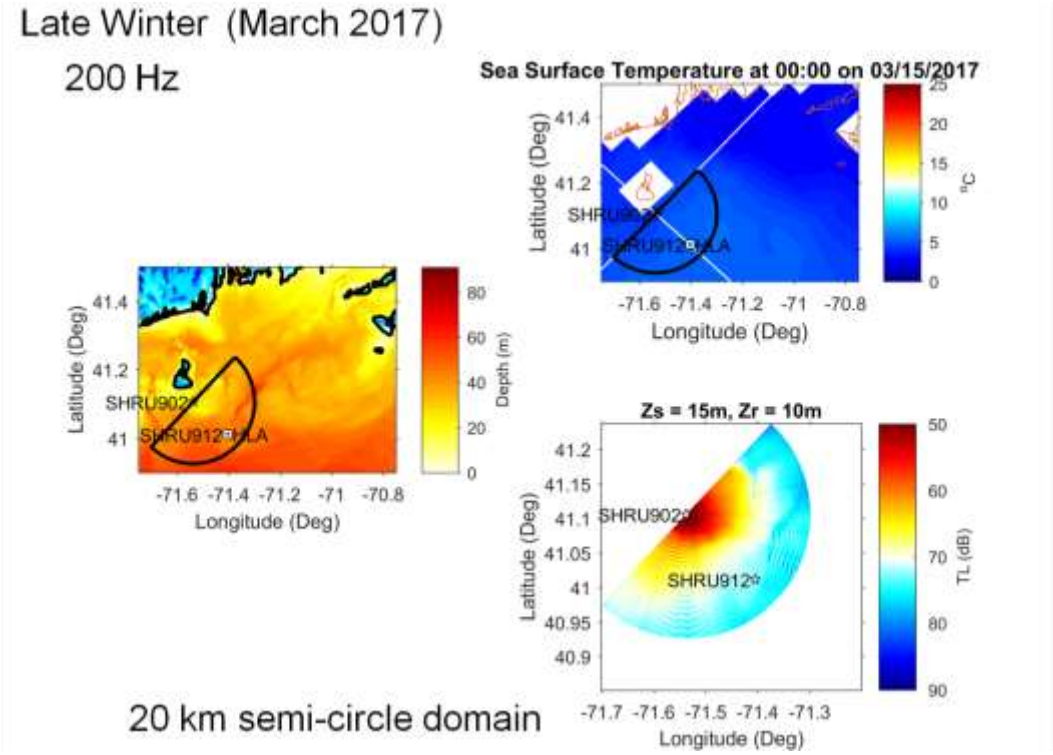

Figure 41. Seasonal variability of underwater sound propagation at BIWF (Late Winter 2017).

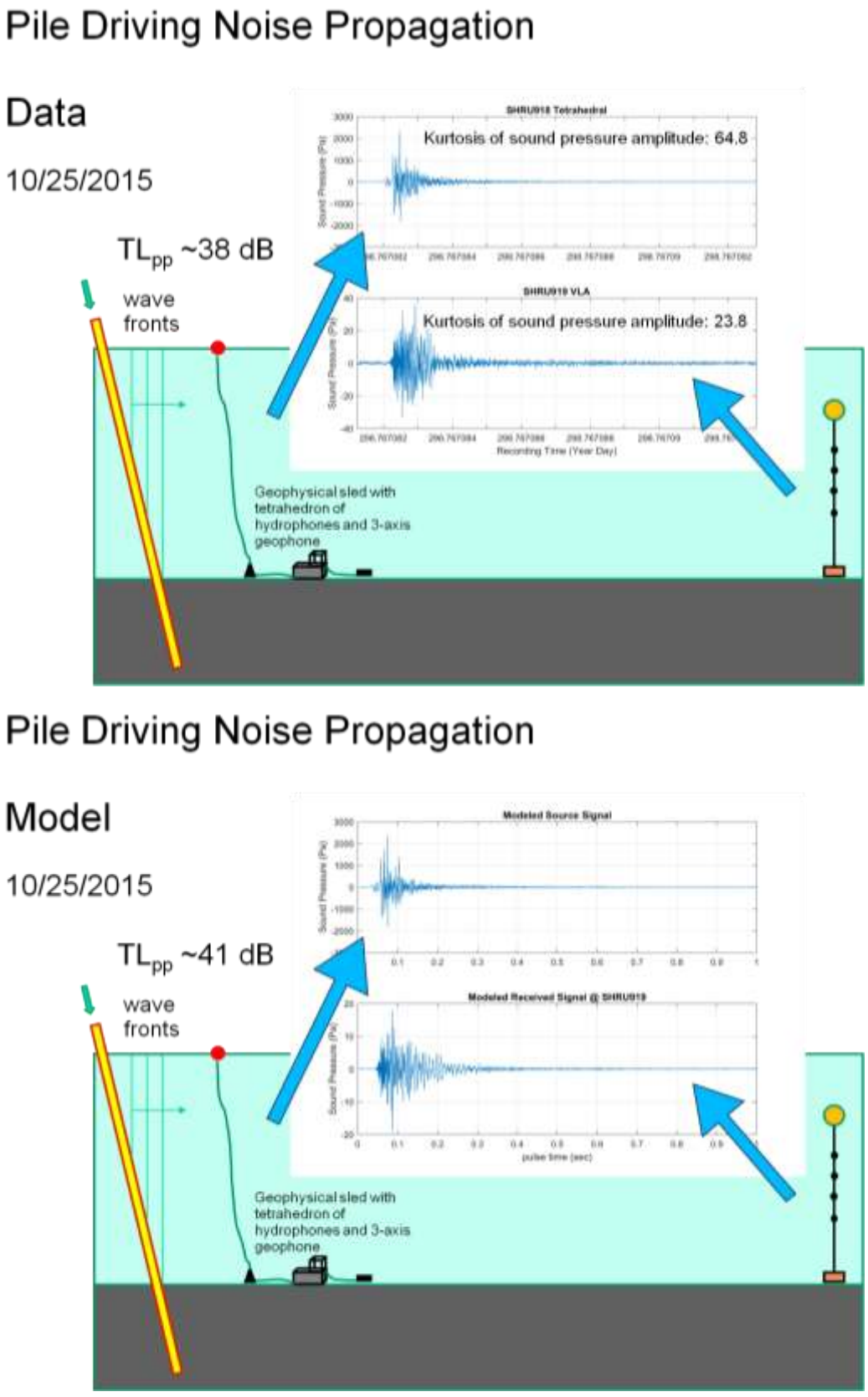

Figure 42. Data-model comparison of pile driving sound propagation.

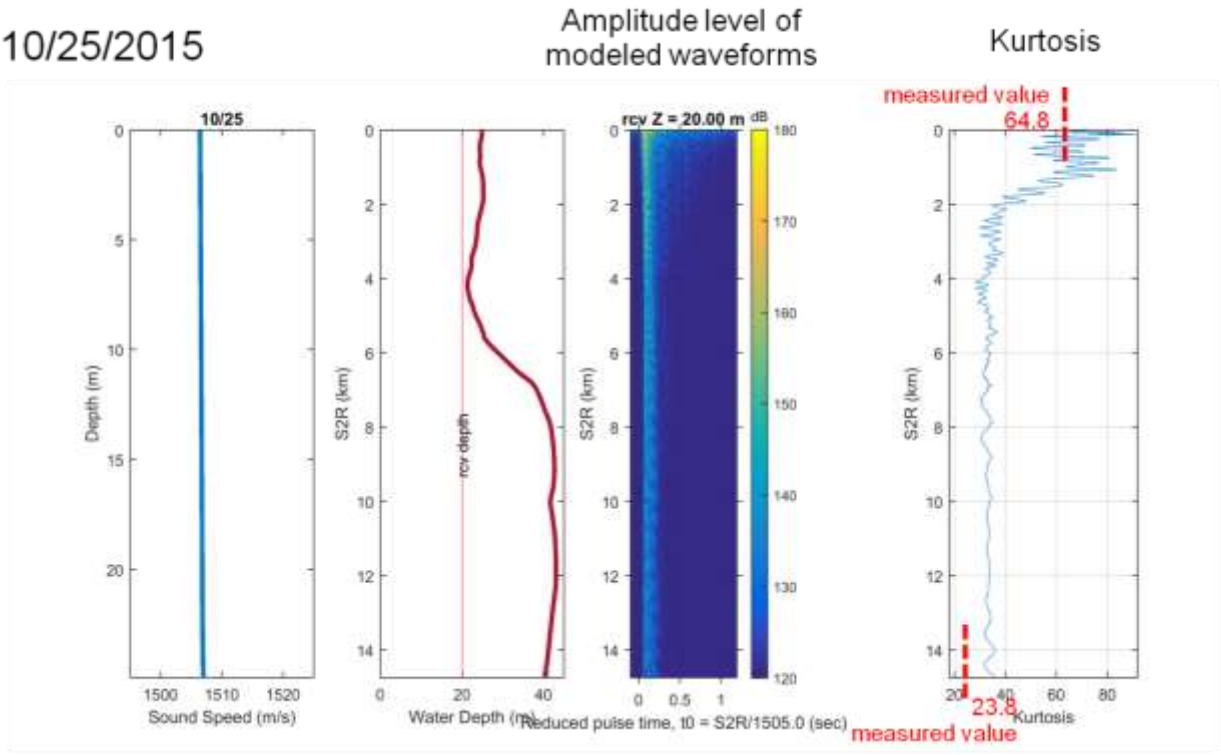

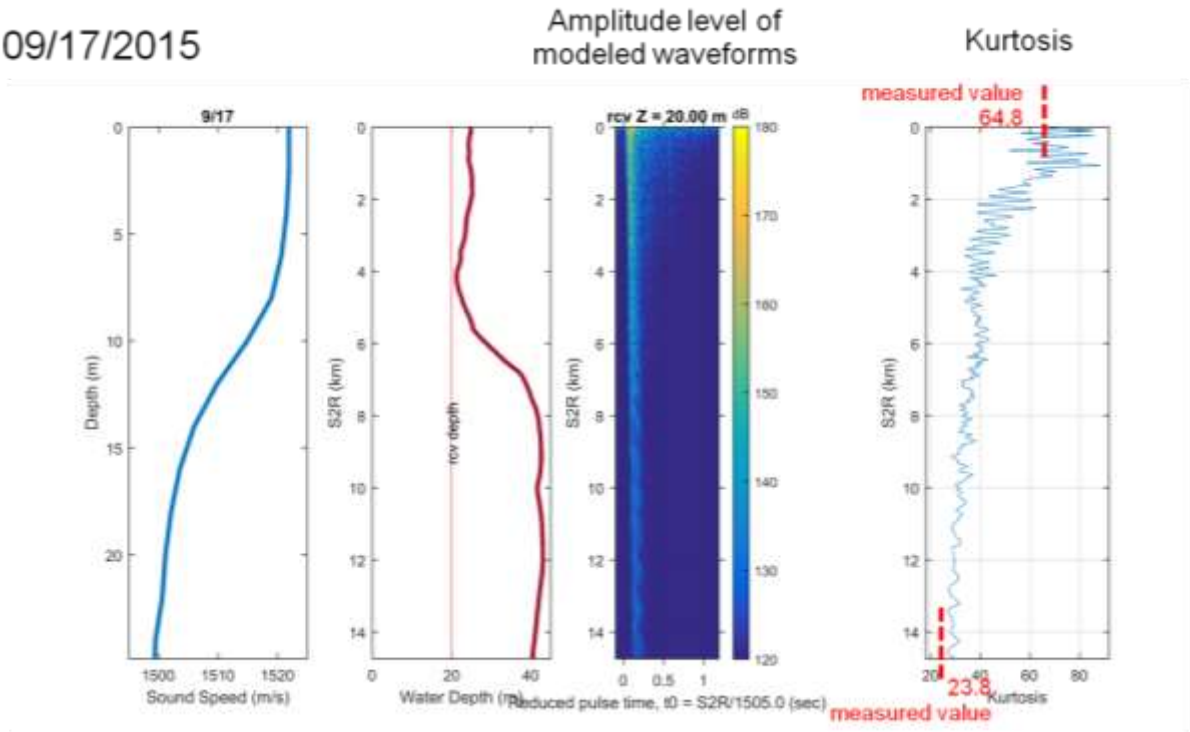

Figure 43. Seasonal variability of pile driving sound propagation.

4.4 Discussion and Conclusions

The BIWF foundation design using raked piles along with the complicated bathymetry, bottom properties and oceanography makes the modeling of underwater propagation of sound generated by the pile driving challenging. The challenged was addressed by breaking up the analyses into two separate modeling efforts 1) 3-D source characterization using finite element modeling of the raked steel pile in air, water and the sediment and 2) underwater acoustic propagation using 3-D Parabolic Equation model. The results and conclusions from the 3-D source characterization using finite element modeling of the raked steel pile in air, water and the sediment will be presented in future technical publications. Key findings from the underwater acoustic propagation modeling using a 3-D Parabolic Equation Model are discussed below

In the BIWF Project Area during summer, there is a strong thermocline with a decline of up to 8 degrees Celsius in less than 10 m (32.8 ft) (**Figure 44**) in the middle of the 20 m (65.6 ft) deep water column.

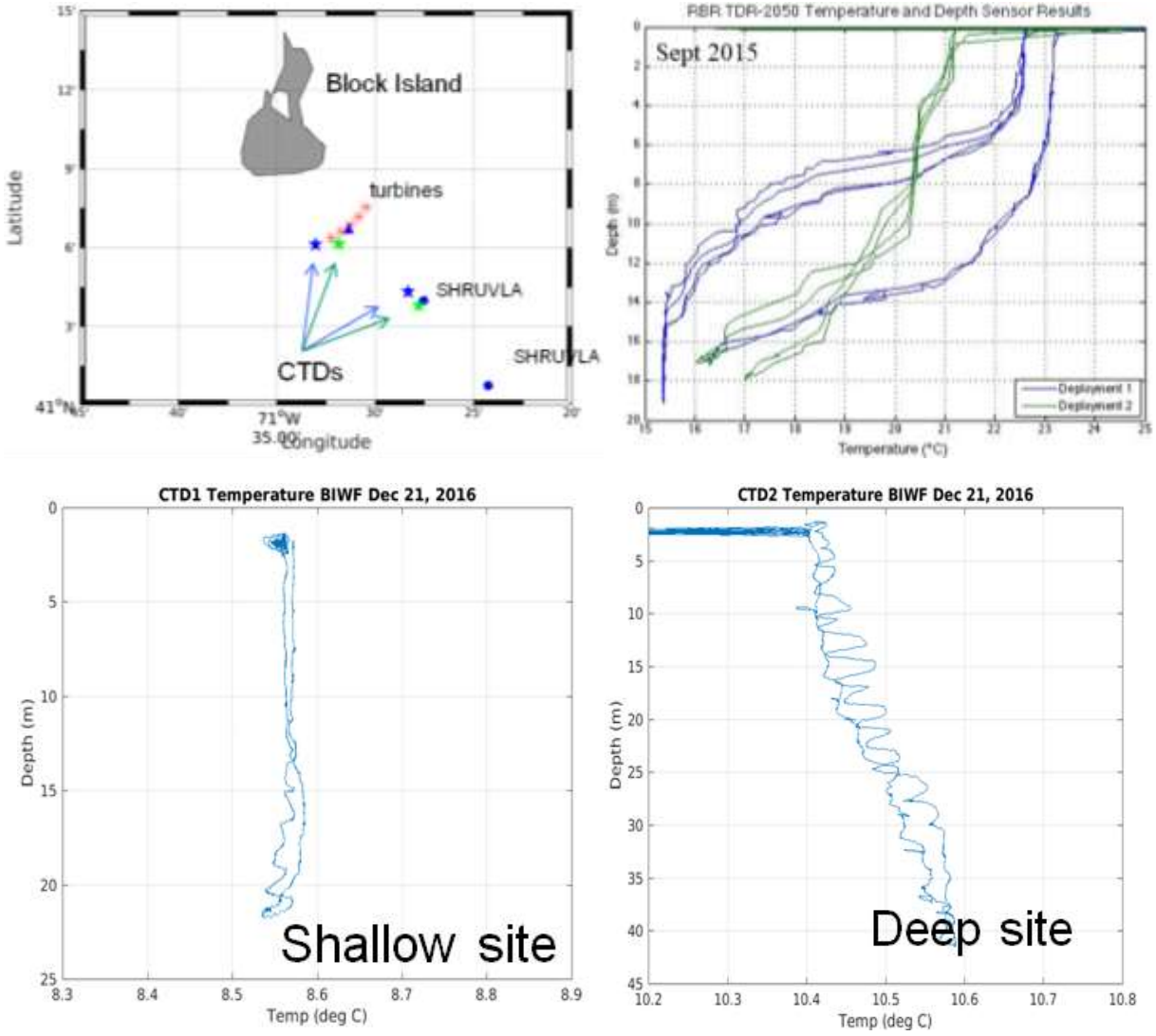

Figure 44. Temperature profile measurements collected during two hydrophone mooring deployment cruises. The upper left panel shows the CTD locations where the measurements were taken; the upper right panel shows temperature profiles in summer time (September 2015), and the bottom two panels show the profiles in winter time (December 2016).

This produces a significant negative sound speed gradient of -3.2/s and generates a downward refracting propagation condition. This can cause sound rays to bend towards the seabed and hit the bottom with greater angles and result in higher bottom reflection loss.

In winter, the surface water cools down because of less solar heat and atmosphere effects, so the thermocline weakens. In addition, strong winds and storms can enhance water column mixing. As a result, the water temperature is nearly constant from the sea surface to the seabed, which produces an iso-velocity condition and more omni-directional propagation, in contrast to downward refracting in summer time. Less bottom reflection loss is expected. In addition, colder water temperature causes lower water sound speed, which increases the acoustic impedance at the seabed. So, the total reflection angle from the bottom becomes greater compared to summer. This can remarkably enhance long distance propagation of underwater sound.

The 3-D sound propagation model simulations showed that underwater sound propagation within the BIWF Project Area show a strong seasonal variability, and it suggests pile-driving sound decays faster in summer time when the water column supports a downward refracting propagation condition. Future model development incorporating surface wind waves and sub-bottom sediment layer structure is required to improve the present model. The ultimate future goal is to establish an underwater soundscape modeling, predicting and planning software system.

5 Marine Mammal Detection

5.1 Introduction

Passive acoustic monitoring has become a standard methodology for assessing occurrence and distribution of marine mammals; however, little research has been conducted on the detection range of different species' vocalizations, and how that detection range varies with environmental conditions (e.g., ocean conditions, water depth, sediment type), signal type, passive acoustic monitoring system, and platform (e.g., moored buoy, autonomous underwater vehicle). To effectively use passive acoustics to monitor marine mammals, an understanding of the area over which a given monitoring system can detect a particular species of interest is critical.

The RODEO Program BIWF environmental monitoring offered a unique opportunity to use data collected by ongoing monitoring efforts in the Project Area, such as the real-time digital acoustic monitoring (DMON) setup, to determine what additional information could be gleaned from underwater acoustic data collected by platforms deployed underwater to monitor sounds associated with BIWF construction and operations. During the monitoring, one fin whale (*Balaenoptera physalus*) was detected by both the RODEO system and DMON setup. Because the RODEO systems were much more elaborate than the DMON system, RODEO data were used to investigate the potential for improving whale detection using data collected by such instruments, as well as increasing the understanding of the propagation (hence detection) of low-frequency vocalizations in shallow water environments. Results and observations from this analysis are summarized below.

5.2 Background

Fin whales are a type of baleen whale and are the second largest species of whale still found in today's oceans. Currently fin whales are listed as endangered under the U.S. Endangered Species Act and as federally endangered on the Rhode Island state list. They are found in the deep, offshore waters of all the major oceans, primarily in temperate and polar waters and less commonly in the tropics (NOAA 2018).

They are the most abundant large whale found in southern New England continental shelf waters and are most prevalent from spring through fall. While some whales stay throughout the winter, most are thought to migrate offshore and south to subtropical waters for mating and calving. They move to colder areas of the Arctic and Antarctic for feeding during the summer months (ACS 2018). Fin whales are present in all four seasons in the waters off of Rhode Island (**Figure 45**).

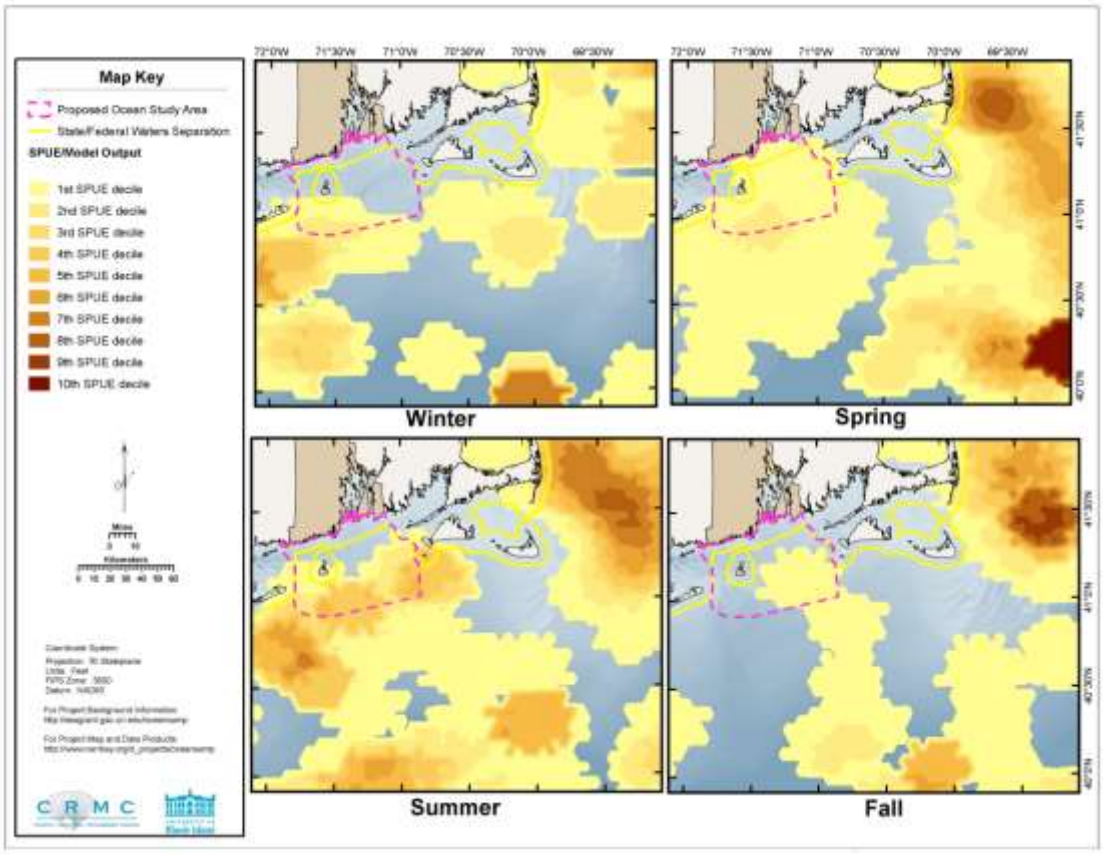

Figure 45. Modeled seasonal relative abundance patterns of fin whales offshore of Rhode Island showing their presence year round (Kenney and Vigness-Raposa 2010).

Adult fin whales can measure between 17 and 24 m (55.8 and 78.7 ft) long, with adult females being slightly larger than males. Fin whales are also one of the fastest of the baleen whales, with the capability to travel large distances in short amounts of time. Normally they swim between 5 and 8 knots (9 and 15 km/hr), but they can travel in short bursts of 15 to 20 knots (28 to 37 km/hr) (Kenney and Vigness-Raposa 2010).

Fin whales produce low frequency calls ranging from 18 to 300 Hz. The most common are the 20 Hz pulses, which are characterized by a chirp lasting approximately 1 second and sweeping down in frequency from approximately 25 to 15 Hz (Weirathmueller et al. 2013). These are high amplitude calls that occur in pulse trains with regular inter-pulse intervals (IPIs). An IPI is the time from the start of one pulse to the start of the next (Thompson et al. 1992).

Whales from northern latitudes have shorter inter-pulse intervals than whales at southern latitudes (Nieukirk et al. 2012). In waters off Rhode Island, different intervals are observed during different seasons. A short IPI season is observed from September through January where the interval is commonly 9.6 seconds. A long IPI season that runs from March through May is where intervals are commonly 15.1 seconds. The intermediate months are transition periods. Shorter IPIs in conjunction with high abundance

of 20 Hz vocalizations correspond to the fin whale reproductive season, which is November through March (Morano et al. 2012).

The 20 Hz pulses are only produced by males and are thought to be a breeding display to attract females. Studies suggest that fin whales communicate over tens of kilometers, but the precise communication range is not known (Nieukirk et al. 2012). Vocalizing fin whales behave in a stereotypical manner where they move very little and appear to stay at approximately 50 m (49.2 ft) depth (Au and Hastings 2008). Fin whales are most often alone, but groups of three to seven individuals are common as well (ACS 2018, Rebull et al. 2006).

Songs of 20 Hz pulses produced in series with stereotyped pulse intervals are known as a bout. Bouts are composed of regularly repeated pulse intervals, either at one nominal pulse rate (singlet) or at two alternating pulse intervals (doublet). Songs typically last between 1 and 20 minutes, but song bouts can last hours to days. The vocalizations generally stop when the whale surfaces, so the signals have periodic interruptions or rests within the bout (Watkins et al. 1987). The call series are usually associated with the respiration cycle of the whales where the rests correspond to when the whale is breathing and the whale is generating the calls when it is diving (Rebull et al. 2006, Watkins et al. 1987).

Few studies estimating fin whale call source levels have been performed because of the difficulty in acquiring a set of calls where the positions of both the whale and acoustic recorder are accurately known (Weirathmueller et al. 2013). Source levels of these 20 Hz pulses are variable and have been estimated at up to 186 dB (Watkins et al. 1987), 159 to 184 dB (Charif et al. 2002) and 189 dB (Weirathmueller et al. 2013).

In this report, 20 Hz fin whale pulses that were detected offshore of Rhode Island are characterized and the propagation of these low frequency vocalizations in a shallow water environment is discussed.

5.3 Data Collection

Acoustic data were recorded in fall 2015 during the BIWF Phase 1 construction using two stationary vertical arrays and a tetrahedral array that were equipped with Several Hydrophone Receive Units (SHRUs) as the data acquisition systems. Each vertical array consisted of four hydrophones spaced 5 m (16.4 ft) apart that were located between water depths of 20 and 40 m (65.6 and 131.2 ft). Two of the hydrophones had low sensitivity and the other two had high sensitivity. These arrays were deployed 7.5 km (4.7 mi) and 15 km (9.3 mi) from the BIWF foundations in approximately 40 m (131.2 ft) of water. The tetrahedral array consisted of four hydrophones deployed close to the seabed at a range of 500 m (1,640.4 ft) from the foundation of WTG 3 (**Figure 46**).

Fin whale vocalizations were recorded on all of the stationary sensors deployed. Custom MATLAB scripts were used to analyze the data. A band pass filter in the bandwidth of 15 to 28 Hz was applied, and a peak picker was utilized to identify all peaks occurring at intervals of at least 8 seconds. Detection was achieved by thresholding the peaks on the signal-to-noise ratio.

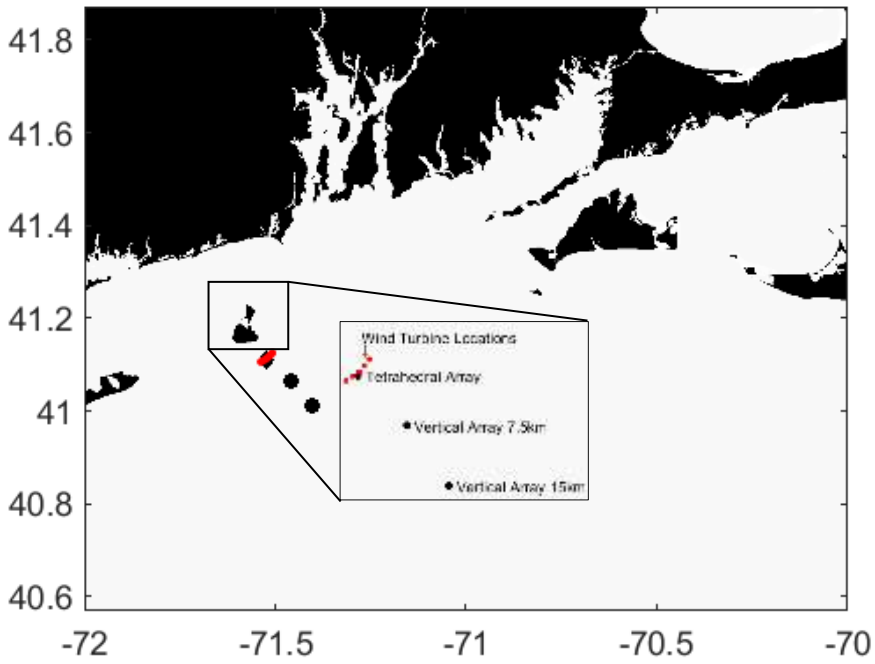

Figure 46. Location of the stationary sensors deployed during the BIWF construction phase.

5.4 Detections

On 4 November 2015, a bout of fin whale 20 Hz pulses was detected for over 18 hours. It is hypothesized that these vocalizations were made by a single male fin whale moving off the coast of Massachusetts and Rhode Island. Detections were made on the tetrahedral array and both of the vertical arrays and also overlap with detections received on a DMON (digital acoustic monitoring instrument) buoy located off of Nomans Land, Massachusetts (WHOI 2018). The DMON buoy was approximately 40 km (24.9 mi) from the locations of the vertical arrays.

The bout was recorded for over 18 hours (**Figure 47**). Periodic rests occurred throughout the bout in regular intervals. Based on the amplitude and received level distribution of the detections, the whale was moving towards the vertical array for the first 10 hours of detections and then away from the array for the remaining duration of the detections. The peak received level for each detection was calculated over the duration of the bout according to **Equation 6** (**Figure 48**).

$$RL_{pk} = 20\log_{10}(\max(|P(t)|)) \qquad \text{(Equation 6)}$$

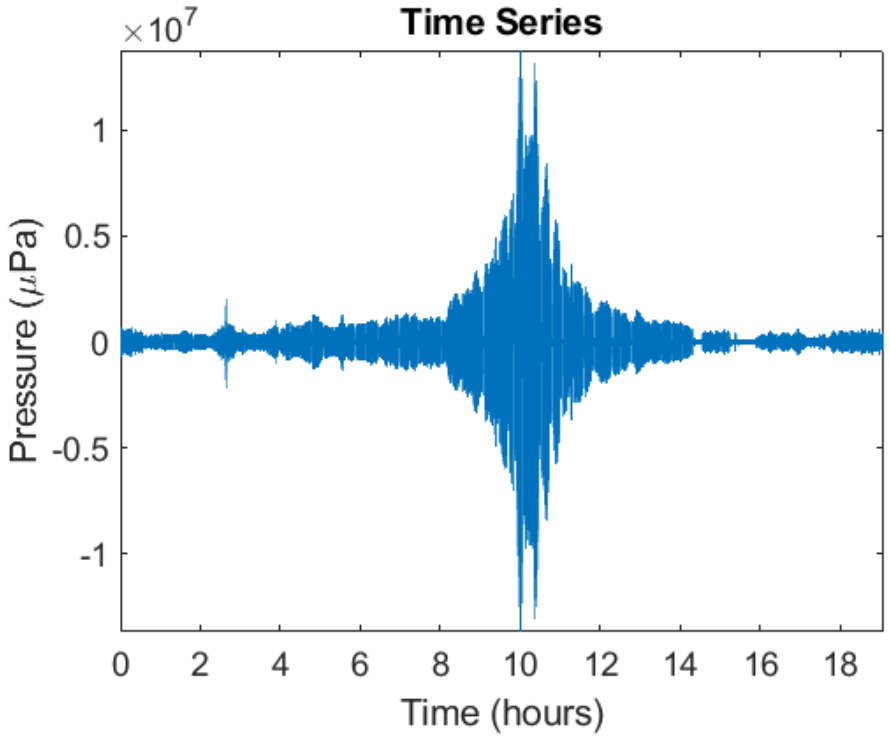

Figure 47. Band pass filtered time series of fin whale bout recorded on one channel of the vertical array location 15 km (9.3 mi) from the wind farm foundations. Time is referenced from the beginning of the bout.

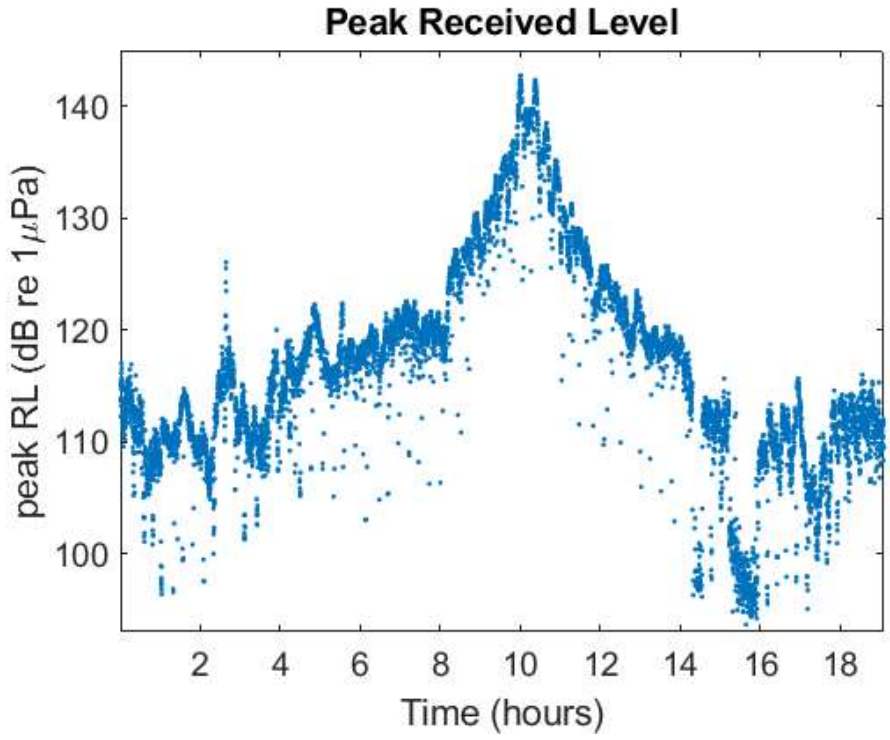

Figure 48. Peak received level for each 20 Hz fin whale pulse detected on 15 November 2015 on one channel of the vertical array located 15 km from the wind farm locations. Time is referenced from beginning of the bout.

The maximum received level was calculated to be 143 dB on the 15 km vertical array and 129 dB on the 7.5 km vertical array, which is assumed to be at the closest point of approach to each respective array. Precise time synchronization between arrays was not available, but based on the relative amplitude of the detections it was determined that the whale was closest to the 15 km (9.2 mi) array.

Looking at portions of the time series, the detections at the beginning and end of the sequences (or the vocalizing periods between rests) were slightly lower in amplitude. This is consistent with that observed by Watkins (1987). **Figure 49** shows a zoomed in portion of the time series illustrating the rest periods breaking up the vocalizations, with the slightly lower amplitude calls before and after the rests. This pattern continued for most of the bout.

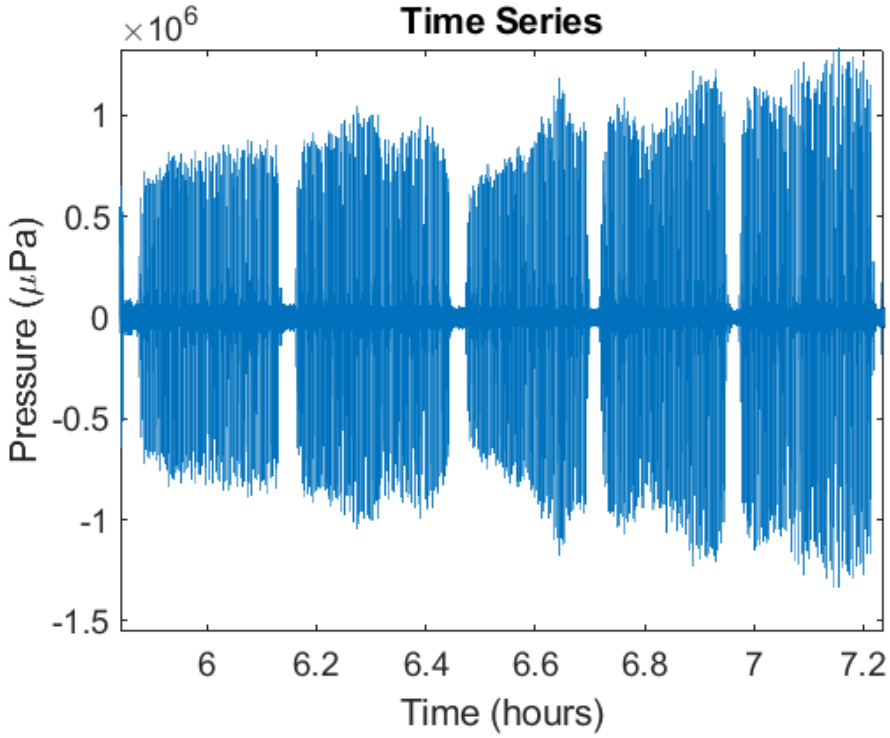

Figure 49. Time series section highlighting the rest periods in between the songs throughout the bout on 15 November 2015 on one channel of the vertical array located 15 km from the wind farm locations. Time is referenced from beginning of the bout.

The median interpulse interval calculated throughout this bout was 9.6 seconds, which is consistent with previously recorded intervals for this water area. This interval in combination with the long duration of high amplitude calls is common behavior for males during reproductive season. These calls were recorded at the beginning of the reproductive season, which runs from November through March (Morano 2012).

5.5 Modal Dispersion

The fin whale bout was detected on sensors located in shallow waters of 40 m (131.2 ft) and less. The propagation of sound waves in shallow waters can be described by normal mode theory where the sound channel is treated like an acoustic wave guide (Au and Hastings 2008). The wavelength of the 20 Hz pulses was roughly 75 m (246.1 ft), assuming a sound speed in the water of 1,500 m/s. Therefore, the waveguide in which the sound was propagating was much deeper than the depth of the water.

The number of propagating modes in a waveguide is dependent on frequency and can be estimated by **Equation 7**, where M is the number of modes, f is the frequency, D is the waveguide depth and c is the sound speed through water (Jensen et al. 2011).

$$M < \frac{2fD}{c} \qquad \text{(Equation 7)}$$

Using a frequency of 20 Hz to represent the fin whale pulses, a sound speed of 1500 m/s, and a waveguide depth equal to that of the water column of 40 m, the number of possible propagating modes is less than 1.067. Assuming that the low frequency vocalizations utilize the bottom sediment as part of the waveguide, there are two possible propagating modes in a waveguide of 75 m (246.1 ft). Two distinct modes were seen in the data collected, where the second mode arrives before the first mode (**Figure 50**). The depth to bedrock in this area is currently being studied so the exact depth is not known, but it is thought that the waveguide in this area at this frequency is from the water surface to the depth of bedrock.

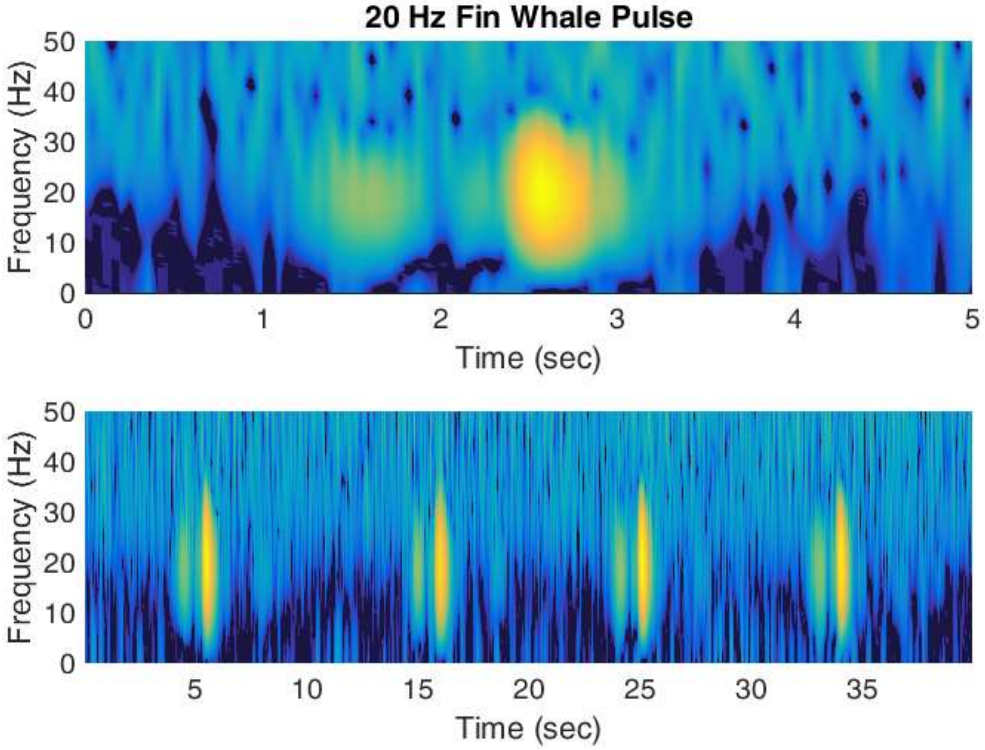

Figure 50. Individual 20 Hz pulse (top) and a few pulses in a series (bottom) showing two distinct modal arrivals.

Each mode is a standing wave in the vertical that propagates in a horizontal direction that is characterized by a shape function and a horizontal wave number, which relates to the phase velocity. The phase velocity for a given mode is the speed at which a constant phase front propagates through the waveguide and it varies with frequency, which is an effect known as dispersion. The group velocity of a mode describes the speed of energy transport and is useful in describing the pulse propagation (Jensen et al. 2011).

For time-limited signals, as in the 20 Hz pulses, different group velocities will separate modes in a signal at long ranges. This is known as modal dispersion. Two distinct modes were seen in the data collected on the vertical arrays and the time interval between the arrivals of each mode varied with range. Individual pulses were examined at times before, at, and after the closest point of approach (**Figure 51**).

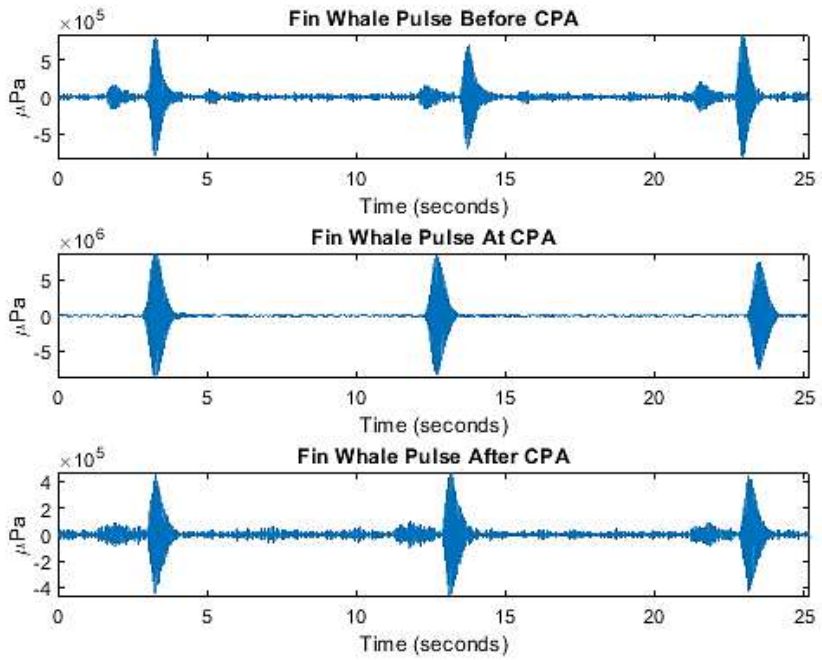

Figure 51. Times series showing individual 20 Hz pulses at example times before, at, and after the closest point of approach. The second mode visibly arrives before the first mode in the top and bottom plot, which relate to times before and after the closest point of approach.

The second mode arrives before the first mode as it is a more sediment driven mode than the first. Because the sound speed through the sediment is faster than that through the water, the second mode travels faster and therefore arrives first. The time delay between the arrival of the second and first mode decreases as the whale approaches the array and then increases as it moves away. Examples of this time delay at different points in the recording are shown in **Figure 52**.

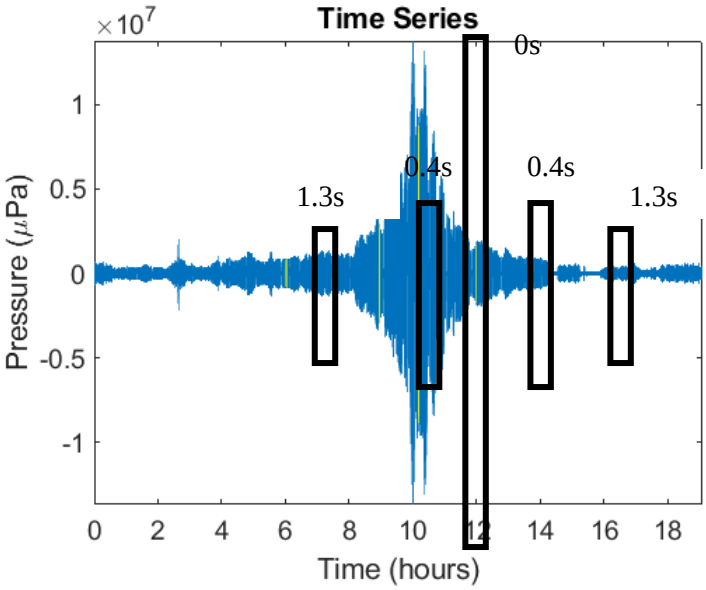

Figure 52. Band pass filtered time series of fin whale bout recorded on one channel of the vertical array location 15 km (9.2 mi) from the wind farm foundations with boxes around time segments where the time delay between modal arrivals were calculated. The time delay between modal arrivals is indicated in the figure.

5.6 Discussion and Conclusions

Fin whales are common marine mammals in waters off Rhode Island. Vocalizations from these mammals were observed and recorded at various times throughout the BIWF Phase I construction phase. A bout lasting over 18 hours thought to be made by a male fin whale was recorded during the beginning of the mating season in November 2015. This recording was used to track the whale as it moved through the monitoring area.

The shallow waters present in the monitoring area contribute to propagation that encompasses a waveguide spanning from bedrock to sea surface. This depth waveguide would result in two propagating modes from a fin whale pulse centered on 20 Hz. The dispersion of these two modes seen in the data provides a promising method of determining the range of the whale from the sensors. The group speed of each mode and the varying time interval between each modal arrival can be used to estimate range. The overall goal is to localize and track the whale as it moved past the sensors. This is an ongoing effort that will utilize the recordings made on the vertical and tetrahedral arrays.

6 References

ACS. 2018. Fin Whale. Retrieved October 19, 2018, from https://www.acsonline.org/fin-whale.

Au, W.W.L., and M.C. Hastings. 2008. Principles of Marine Bioacoustics. New York, NY: Springer Science+Business Media.

Bibee, L.D. 2011. A comparison of seismometer and hydrophone recordings of VLF seismo-acoustic signals, OCEANS 91 Proceedings, Volume: 1, 93–96.

Bruns, B., P. Stein, C. Kuhn, H. Sychla, and J. Gattermann. 2014. "Hydro sound measurements during the installation of large diameter offshore piles using combinations of independent noise mitigation systems." Inter.noise-2014, Melbourne, Australia.

Charif, R., A. Waack, and L. Strickman. 2010. Raven Pro 1.4 User's Manual. Ithaca, NY: Cornell Laboratory of Ornithology.

Charif, R. A., D.K. Mellinger, K.J. Dunsmore, K.M. Fristrup, and C.W. Clark. 2002. Estimated Source Levels of Fin Whale Vocalizations: Adjustments for Surface Interferences. Marine Mammal Science, 18(1), 81–98.

Chapman, C.J., and O. Sand. 1974. Field studies of hearing in two species of flatfish, *Pleuronectes platessa* (L.) and *Limanda limanda* (L.) (Family Pleuronectidae). Comp Biochem Physiol, 47A:371–385.

Chapman, C.J., and A.D. Hawkins. 1973. A field study of hearing in the cod, *Gadus morhua* L. J. Comp. Physiol., 85:147–167.

Coombs, S. and Popper, A.N. J. 1979. Hearing differences among Hawaiian squirrelfish (family Holocentridae) related to differences in the peripheral auditory system. Comp. Physiol. (1979) 132: 203. https://doi.org/10.1007/BF00614491

Dahl, P.H., C.A.F. de Jong, and A.N. Popper. 2015. The Underwater sound field from Impact Pile Driving and Its Potential effects on Marine life, Acoustics Today, 11(2) 18–25.

Dosso, S.E., and G.H. Brooke. 1995. Measurement of seismo-acoustic ocean-bottom properties in the high Arctic, J. Acoust. Soc. Am. 98 (3), 1657–1666.

Elliott, J, K. Smith, D.R. Gallien, and A. Khan. 2017. Observing Cable Laying and Particle Settlement During the Construction of the Block Island Wind Farm. Final Report to the U.S. Department of the Interior, Bureau of Ocean Energy Management, Office of Renewable Energy Programs. OCS Study BOEM 2017-027. 225 pp.

Fay, R.R. 1988. Hearing in Vertebrates: A Psychophysics Data Book. Winnetka, IL: Hill-Fay Associates.

National Oceanic and Atmospheric Administration (NOAA). 2018. Fin Whale. Retrieved October 19, 2018 from https://www.fisheries.noaa.gov/species/fin-whale.

Giard, J., G.R. Potty, J.H. Miller, and C.D.P. Baxter. 2013. "Validation of an Inversion Scheme for Shear Wave Speed using Scholte Wave Dispersion," Proceedings of the OCEANS 2013, San Diego, USA.

Gray, M., P.H. Rogers, and D.G. Zeddies. 2016. "Acoustic particle motion measurement for bioacousticians: principles and pitfalls," Proc. Mtgs. Acoust. 27, 010022; doi: 10.1121/2.0000290.

Hamernik, R.P., W.A. Ahroon, K.D. Hsueh, S. Lei, and R.I. Davis. 1993. Audiometric and histological differences between the effects of continuous and impulsive noise exposures. The Journal of the Acoustical Society of America. 93(4). 2088-2095. 10.1121/1.406695.

Hawkins, A.D., A.D.F. Johnstone. 1978. The hearing of the Atlantic salmon, *Salmo salar* . J Fish Biol, 13:655–673.

Hawkins, A.D., and A.N. Popper. 2014. Assessing the Impact of Underwater Sounds on Fishes and Other Forms of Marine Life, Acoustics Today, 30–41.

HDR. 2018a. Field Observations During Wind Turbine Foundation Installation at the Block Island Wind Farm, Rhode Island. Final Report to the U.S. Department of the Interior, Bureau of Ocean Energy Management, Office of Renewable Energy Programs. OCS Study BOEM 2018-029. 175 pp.

HDR. 2018b. Benthic Monitoring During Wind Turbine Installation and Operation at the Block Island Wind Farm, Rhode Island. Final Report to the U.S. Department of the Interior, Bureau of Ocean Energy Management, Office of Renewable Energy Programs. OCS Study BOEM 2018-047. 155 pp.

HDR. 2019a. Field Observations During Wind Turbine Installation at the Block Island Wind Farm, Rhode Island. Final Report to the U.S. Department of the Interior, Bureau of Ocean Energy Management, Office of Renewable Energy Programs. OCS Study BOEM 2019-027. 292 pp.

HDR. 2019b. Field Observations During Wind Turbine Operations at the Block Island Wind Farm, Rhode Island. Final Report to the U.S. Department of the Interior, Bureau of Ocean Energy Management, Office of Renewable Energy Programs. OCS Study BOEM 2019-028. 281 pp.

HDR. 2019c. Underwater Acoustic Monitoring Data Analyses for the Block Island Wind Farm, Rhode Island. Final Report to the U.S. Department of the Interior, Bureau of Ocean Energy Management, Office of Renewable Energy Programs. OCS Study BOEM 2019-029. 110pp.

Hisada, Y. 1994. "An Efficient Method for Computing Green's Functions for a Layered Half-Space with Sources and Receivers at Close Depths," Bull. Seismol. Soc. Am., 84 (5), 1456–1472.

Jensen, F.B., W.A. Kuperman, M.B. Porter, and H. Schmidt. 2011. Computational Ocean Acoustics (Second). New York, NY: Springer Science+Business Media.

Kenney, R.D., and K.J. Vigness-Raposa. 2010. Marine Mammals and Sea Turtles of Narragansett Bay, Block Island Sound, Rhode Island Sound, and Nearby Waters: An Analysis of Existing Data for the Rhode Island Ocean Special Area Management Plan. In Ocean Special Management Plan.

Ladich, F., and R.R. Fay. 2013. Auditory evoked potential audiometry in fish, Rev Fish Biol Fisheries, 23, 317–364.

Lai, C.G. 1998. "Simultaneous Inversion of Rayleigh Phase Velocity and Attenuation for Near-Surface Site Characterization," Ph.D. Dissertation, Georgia Institute of Technology.

Morano, J. L., D.P. Salisbury, A.N. Rice, K.L. Conklin, K.L. Falk, and C.W. Clark. 2012. Seasonal and geographical patterns of fin whale song in the western North Atlantic Ocean. The Journal of the Acoustical Society of America, 132(2), 1207–1212.

Nieukirk, S. L., D.K. Mellinger, S.E. Moore, K. Klinck, R.P. Dziak, and J. Goslin. 2012. Sounds from airguns and fin whales recorded in the mid-Atlantic Ocean, 1999–2009. The Journal of the Acoustical Society of America, 131(2), 1102–1112. https://doi.org/10.1121/1.3672648.

Popper, A.N., A. D. Hawkins, R. Fay, R. Mann, D. Bartol, S. Carlson, T. Coombs, S. Ellison, W. Gentry, R. Halvorsen, M. Løkkeborg, S. H. Rogers, P. Southall, B. Zeddies, D. N. and T. William. 2014. Sound Exposure Guidelines for Fishes and Sea Turtles: A Technical Report prepared by ANSI-Accredited Standards Committee S3/SC1 and registered with ANSI, Springer Briefs in Oceanography, ASA Press.

Popper, A.N., and A.D. Hawkins. 2018. “The importance of particle motion to fishes and invertebrates,” J. Acoust. Soc. Am., 143(1).

Popper, A.N. 2006. What do we know about pile driving and fish? In Proceedings of the 2005 International Conference on Ecology and Transportation (Irwin, C. L., Garrett, P. & McDermott, K. P., eds.), pp. 26–28. Raleigh, NC: Center for Transportation and the Environment, North Carolina State University.

Popper, A.N. and M.C. Hastings. 2009. The effects of anthropogenic sources of sound on fishes, Journal of Fish Biology, 75, 455–489.

Popper, A.N. and W.N. Tavolga. 1981. Structure and function of the ear in the marine catfish, *Arius felis*. Journal of Comparative Physiology 144:27-34.

Potty, G.R. and J.H. Miller. 2018. “Shear wave inversion using the horizontal to vertical ratio of Scholte wave particle velocity,” Proceedings of the IEEE/MTS OCEANS Conference (OCEANS 17), Charleston, NC, USA.

Potty, G.R. and J.H. Miller. 2012. “Measurement and Modeling of Scholte Wave Dispersion in Coastal Waters,” Proceedings of 3rd International Conference on Ocean Acoustics (OA 2012), Beijing, China, J. Simmen, Z. Li, and J-X Zhou eds., AIP Conference Proceedings.

Potty, G.R. and J.H. Miller. 2018. “Shear wave inversion using the horizontal to vertical ratio of Scholte

wave particle velocity," IEEE/MTS OCEANS -2018, Charleston.

Rebull, O.G., J.D. Cusí, M.R. Fernández, and J.G. Muset. 2006. Tracking fin whale calls offshore the Galicia Margin, North East Atlantic Ocean Tracking fin whale calls offshore the Galicia Margin, North East. 120(4), 2077–2085. https://doi.org/10.1121/1.2336751.

Reinhall, P.G. and P.H. Dahl. 2011. Underwater Mach wave radiation from impact pile driving: theory and observation, The Journal of the Acoustical Society of America 130, 1209–1216.

Rogers, P.H. A.D. Hawkins, A.N. Popper, R.R. Fay, and M.D. Gray. 2016. "Parvulescu revisited: Small tank acoustics for bioacousticians," in The Effects of Noise on Aquatic Life II, edited by A.N. Popper and A.D. Hawkins (Springer Science+Business Media, New York), pp. 933–941.

Thompson, P.O., L.T. Findley, and O. Vidal. 1992. 20-Hz pulses and other vocalizations of fin whales, Balaenoptera physalus, in the Gulf of California, Mexico. The Journal of the Acoustical Society of America, 92(6), 3051–3057.

Tsouvalas, A., and A.V. Metrikine. 2016. "Structure-Borne Wave Radiation by Impact and Vibratory Piling in Offshore Installations: From Sound Prediction to Auditory Damage," J. Mar. Sci. Eng., 3, 44; https://doi:10.3390/jmse4030044.

Watkins, W.A., P. Tyack, K.E. Bird, and J.E. Bird. 1987. The 20-Hz signals of finback whales (*Balaenoptera physalus*). The Journal of the Acoustical Society of America, 82(6), 1901–1912. https://doi.org/10.1121/1.395685.

Weirathmueller, M.J., W.S.D. Wilcock, and D.C. Soule. 2013. Source levels of fin whale 20 Hz pulses measured in the Northeast Pacific Ocean Source levels of fin whale 20 Hz pulses measured in the Northeast Pacific Ocean. The Journal of the Acoustical Society of America, 133(2), 741–749. https://doi.org/10.1121/1.4773277.

Woods Hole Oceanographic Institution (WHOI). 2018. Autonomous Real-time Marine Mammal Detections. Nomans Land Buoy. Retrieved October 19, from http://dcs.whoi.edu/nomans0315/nomans0315.shtml.

Wilkes, D.R. and A.N. Gavrilov. 2017. Sound radiation from impact-driven raked piles. The Journal of the Acoustical Society of America. 142, 1-11. 10.1121/1.4990021.

Appendix A: Pile-Driving Data Analyses Technical Report

Block Island Wind Farm Acoustic Measurements Final Report

Marine Acoustics, Inc

2 Corporate Place, Suite 105

Middletown, RI 02842

Prepared by:

Jennifer L. Amaral

Adam S. Frankel

Kathleen Vigness-Raposa

October 31, 2018

Table of Contents

Table of Figures

Table of Tables

1. Introduction

Marine Acoustics, Inc. (MAI) measured the underwater acoustic sound created by pile driving construction activities associated with the Block Island Wind Farm (BIWF) during September 2015. Impact pile driving creates intense sound that radiates into the environment and propagates through the air, water, and sediment. Observational and numerical studies suggest that only about 0.5% of the hammer energy used during pile driving translates into acoustic energy in the water column (Dahl, 2015).

The BIWF pile driving was performed to secure the lattice jacket foundation support structure for each wind turbine to the seabed. Each foundation required cylindrical, steel piles, split into two or three sections, to be impact driven at the four corners of the structure. The legs of the jacket structure were raked at an angle of 13.27° to the vertical (Figure 1). Raked piles are common in infrastructure projects because of their increased resistance to lateral loads. Due to the non-axisymmetric geometry of the pile relative to the water column and seabed, raked piles are expected to radiate underwater sound with an azimuthal dependence (Wilkes, 2017).

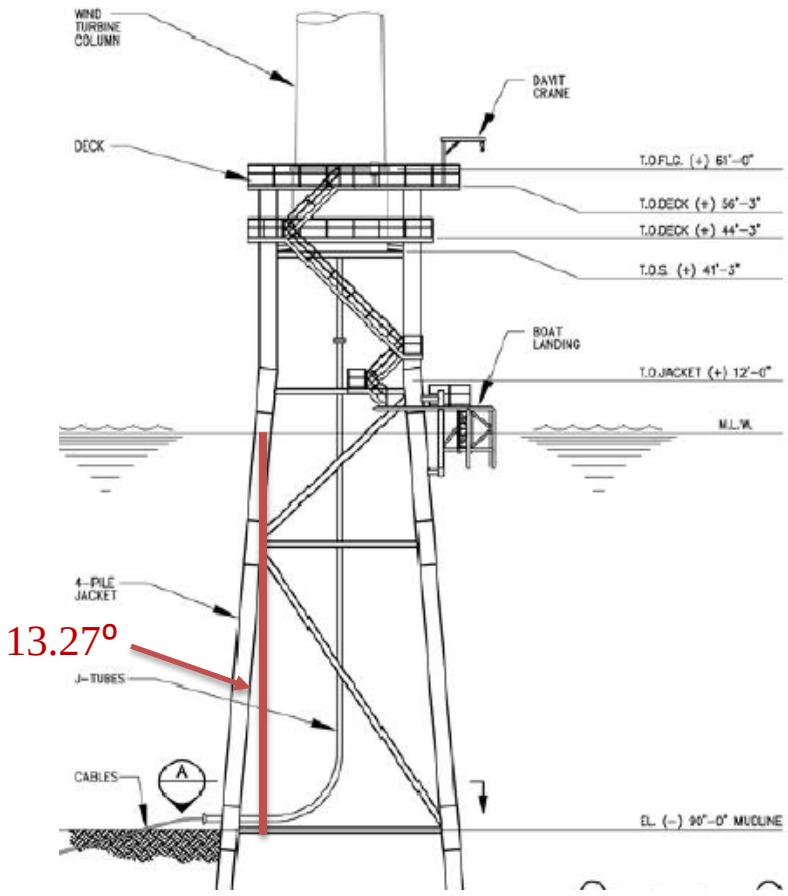

Figure 1. Schematic of the lattice jacket foundation structure showing the raked piles.

MAI deployed a passive towed hydrophone array from a vessel and recorded the sounds of the impact pile driving as the vessel moved away from the construction activity. The recordings were taken during the pile driving events that occurred on September 2 and 17, 2015. A total of three pile driving events were recorded; two associated with the installation of Wind Turbine Generator (WTG) 3 on September 2 and one associated with WTG 5 on September 17. The recordings were analyzed to determine the sound levels of the pile driving versus range from the turbine, strike energy, pile angle, and penetration depth into the sediment. The analysis investigated how the impulsive nature of the pile driving signal changes with range and how the angle of the raked pile being driven impacts the overall received sound levels.

2. Field Methods

2.1 Data Collection Equipment

An eight-hydrophone passive towed array built by Hydroscience Technologies, Inc. was deployed by MAI to record the impact pile driving events. The hydrophone elements are irregularly spaced to allow for beamforming at multiple frequencies. The array was towed from the R/V *Shanna Rose*, which is based at the University of Rhode Island's dock at the Point Judith Marina.

The data acquisition system used with the towed array was developed and built by MAI specifically for use with this array. The system is comprised of Alligator BNC input/output boxes, an Alligator SCS-800 chassis with an Alligator 820 Bessel-function filter card, a National Instruments SCB-68 interface box, and a National Instruments PCI 6071E analog-to-digital conversion card. The array itself is powered using two 12V batteries connected in series.

The data were recorded from the array using the software program Raven (Charif et al. 2010) in 30 second files at a sampling rate of 64 kHz. Gains of 1x, 10x, or 100x were applied during data acquisition in the field depending on the range of the array from the pile driving event.

2.2 Field Procedures

The field procedures discussed in this section were similar between the two deployment days. The towed array was loaded onto the R/V *Shanna Rose* and secured on deck. The data acquisition system was loaded and set up in the lab area of the vessel. Transit to the Block Island Wind Farm site took about two hours from the Point Judith Marina. Once at the start location, the towed array was unspooled and deployed into the water. Sea Bird SBE39 temperature and pressure sensors were attached to the array at various locations along the length of the cable.

Once the array was completely deployed, it was tied to the A-frame of the vessel. A strain relief was rigged to take the tension out of the array while it was being towed. The array was connected to the battery and powered up and the data acquisition system was tested.

For the cruise on September 2, the gain was set at 100x initially. This proved to be too high and resulted in clipped data, so the gain was lowered to 10x. On September 17, the gain was set to 1x to start. Once the boat was in position as close to the pile driving location as possible, the array was towed until straight. Recording was started using Raven and the time series of each of the channels was viewed in real time. Once the signal to noise ratio (SNR) started to become too low, the gain was increased to 10x. The gain was then increased to 100x at a point farther along the transect.

During both cruises, the array was towed as straight as possible along a radial emanating from the location of the pile driving. If pile driving stopped, the boat slowed down or stopped until pile driving started again. Both cruise days were successful in that pile driving occurred and data were collected along a radial at varying distances from the pile. The GPS positions of the R/V *Shanna Rose* were recorded by the captain throughout the duration of the towed array deployment. These data were used during the analysis to determine the range of the array to the pile driving events at all points during the towing operations.

On September 2, pile driving had already started before the boat reached the desired start position. The array was quickly deployed and approximately 20 minutes of data were collected during this event. Some of these data were clipped and therefore not all of the data recorded with this first pile driving event were used for analysis. Pile driving stopped for a period of time while another pile was prepared to be driven. The towed array was deployed during this down time but not recording. Recording began again once the pile driving operations on the next pile started. Therefore, there are two separate pile driving events for the cruise on September 2.

On September 17, the array was in the water before pile driving operations began. Once the pile driving started, the boat began to move away from the pile. There is only one pile driving event during this cruise. There was near continuous pile driving for about an hour that was recorded.

2.3 Pile Driving Events

A total of three pile driving events were recorded; two on September 2 and one on September 17. All of the piles recorded were the first section (P1) of each pile. The recordings on September 2 were of the B2 and A2 pile being driven on WTG 3. The recording on September 17 was of the A1 pile being driven on WTG 5. The track lines for all three piling events are provided in Figure 2. The locations of the A1, A2, and B2 legs of the lattice jacket foundations are provided in Figure 3.

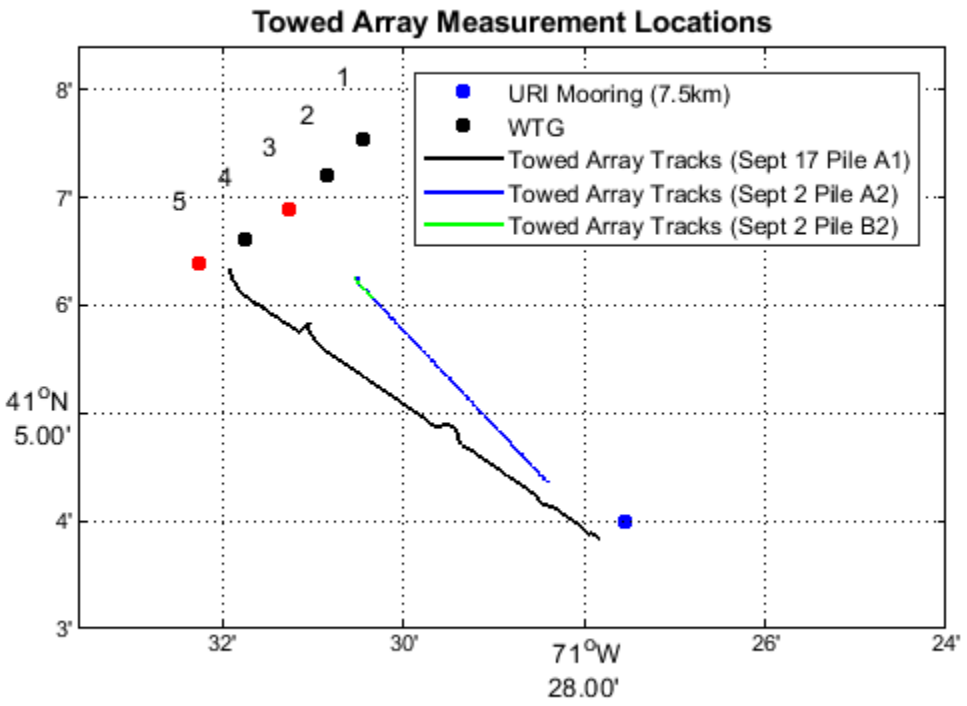

Figure 2. MAI towed array track lines for all three piling events. Wind turbine locations are indicated by black dots. The red dots indicate the turbines on which MAI recorded pile driving.

3. Analysis Methods

3.1 Range Determination

The GPS data file recorded by the captain of the R/V *Shanna Rose* from each cruise was downloaded. The position of the pile(s) being driven was provided. The distance between each vessel position and the pile was determined using great circle calculations.

Since the GPS position recorded was that of the vessel, the distance offset from the GPS receiver to the middle of the array had to be determined. The distance from the GPS receiver to the stern of the boat was estimated at 7 m, the amount of hydrophone array lead-in cable was 47 m, and the distance to the center of the array was 50 m. Therefore, a distance offset of 104 m was used in the analysis.

3.2 Pile and Towed Array Orientation

The piles are angled in relation to the vertical of each foundation, as shown in Figure 1. The towed array measurements were of different piles and therefore at different orientations relative to the pile. Figure 3 indicates the piles that were driven on the three different days. The orientations of the foundations are all the same, with pile B1 pointing north at 0°. Piles B2 and A1 were taken to be at 90° and 270°, respectively.

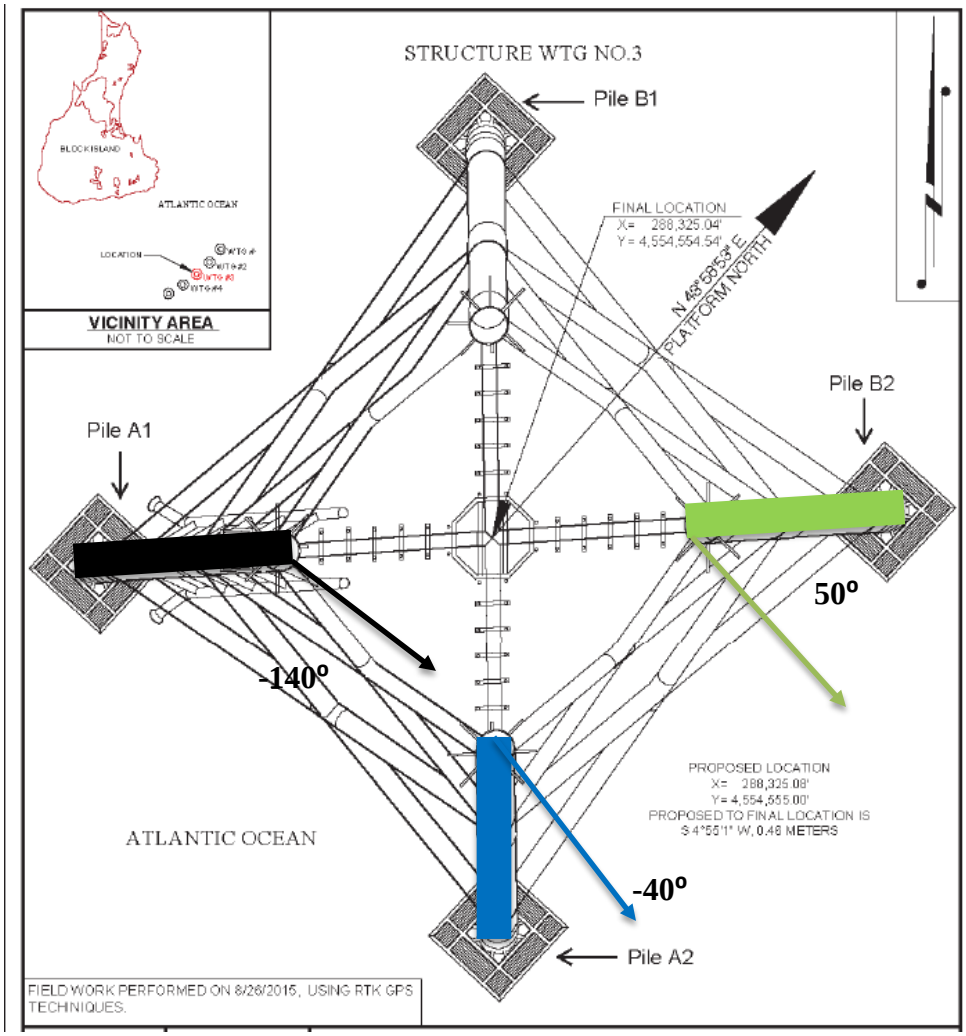

Figure 3. Indications of which piles were driven during the specific deployment days of September 17, 2015 (black), September 2, 2015 pile event 1 (green) and September 2, 2015 pile event 2 (blue). Calculated horizontal orientation angles between pile and array transit are indicated. Arrows represent the direction of the towed array transit in relation to the pile.

Using the bearing of each towed array transit in relation to the center of the wind turbine and the orientation of each pile, the orientation of the towed array transit in relation to the pile was calculated. The horizontal angle between the array and the piles driven on September 2 was 50° and -40°, whereas the angle between the array and the

pile driven on September 17 was approximately -140° (Figures 3 and 4). A positive angle is clockwise from the towed array track line to the pile and a negative angle is measured counterclockwise from the track line to the pile being driven.

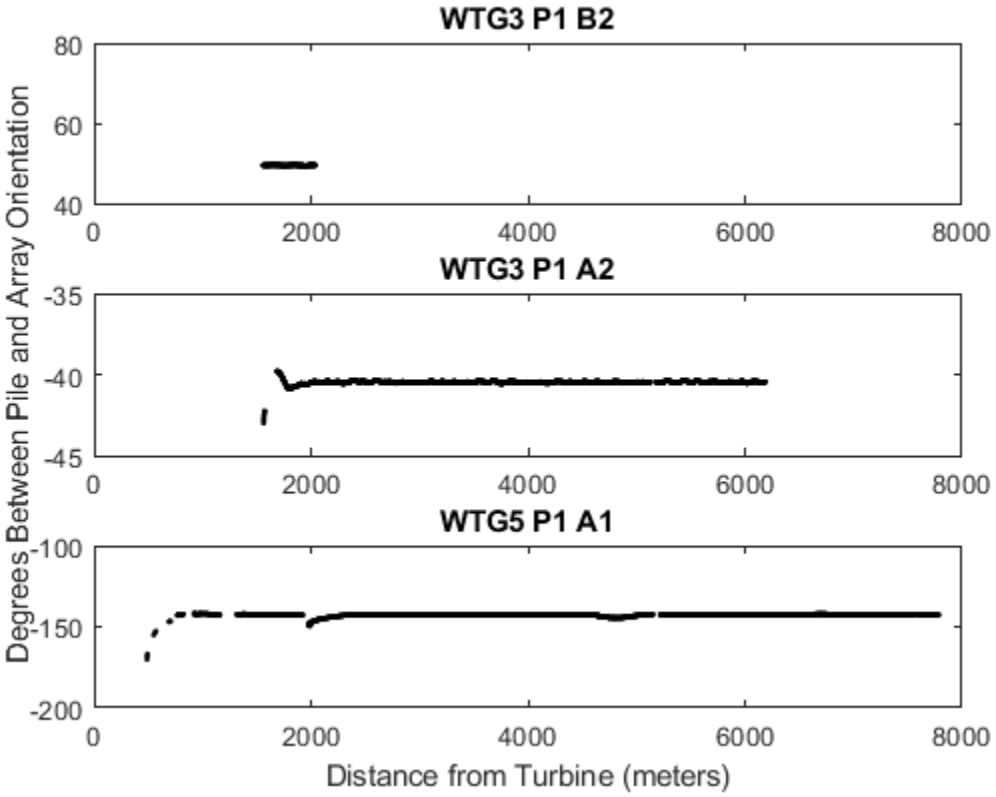

Figure 4. Horizontal angle between the towed array track line along the transit and the orientation of the pile being driven for all three pile driving events. Angle is measured clockwise relative to the pile. A negative angle means the array is east of the pile being driven.

The horizontal angles calculated for the two events on September 2 show that the towed array transit was at roughly the same relative angle for both piles driven. Therefore, the orientation of the pile to the array was very similar. The orientation of the pile to the array was much different on September 17, with the relative angle of the pile being more towards the seafloor bottom than during the measurements made on September 2. When the array is oriented such that the pile is angled more towards the seafloor bottom, the top of the pile is closer to the array. When the bottom of the pile is closer to the array than the top, this is defined as the pile angled towards the surface (Figure 5).

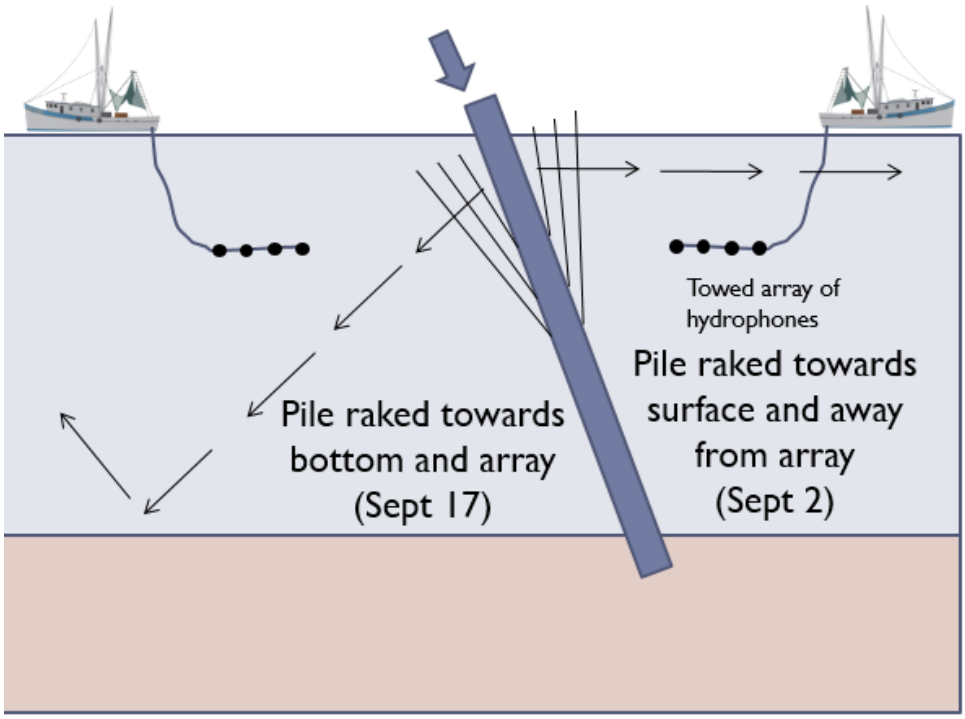

Figure 5. Schematic showing the orientation of the pile towards the array on both measurement days. The V-shaped lines emanating from the pile represent the Mach cone produced when the pile is struck.

Wilkes (2017) demonstrated that sound radiation from a raked pile is significantly different at various horizontal directions from the pile. They reported sound exposure levels (SELs) radiated by piles raked at an angle of 14° to the vertical and inclined towards the array direction to be 10 dB lower at distances of 1.2-1.5km from the pile than those radiated from piles inclined in the opposite direction.

3.3 Underwater Mach Wave Generated from Pile Driving

The high-pressure underwater noise field generated from impact pile driving on hollow steel pipes is attributed to a “Mach wave” effect (Dahl, 2015). Elastic waves are excited in the steel pile due to hammer strikes. The hammer energy travels down the length of the pile as compressional waves, which causes the pile to bulge outwards and deform. This radial deformation of the pile wall is due to the Poisson effect, which is when a material is compressed in one direction and expanded in another. The bulge acts as the sound source because it produces pressure waves in the air, water, and sediment as it moves down the length of the pile (Wilkes, 2017).

The compressional wave speed in steel is much greater than the speed in water. As the pressure wave from the pile enters the water it will slow down, causing a Mach cone around the pile. The angle of this Mach cone is dependent on the ratio of the

compressional wave speed in water to that in steel. Assuming the compressional wave speed in steel (Cs) is 5300 m/s and the speed through water (Cw) is 1500 m/s, the angle of the Mach cone relative to the axis of the pile would be approximately 16°, which was calculated using Equation 1. Depending on the precise values of Cw and Cs, the angle could be in the neighborhood of 15°-19° (Dahl, 2015).

$$\theta = \sin^{-1}\frac{Cw}{Cs} \qquad \text{(Eq. 1)}$$

The angle calculated in Equation 1 is relative to the axis of the pile. When the pile is raked, the sound level radiated from the pile will depend on the orientation from the pile. The wave front of the primary Mach wave radiated in the direction of the pile incline has a much steeper incidence angle on the seabed compared to that in the opposite direction where it propagates almost horizontally (Figure 6). Due to the non-axisymmetric geometry of the pile relative to the water column and seabed, raked piles are expected to radiate underwater sound with an azimuthal dependence, with sound levels varying by approximately 10 dB in different directions (Wilkes, 2017).

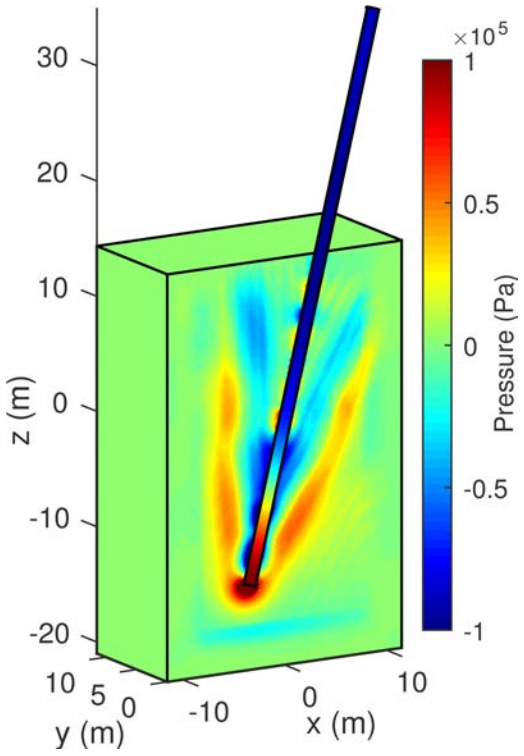

Figure 6. Near-field results from a finite element model for a 3D pile raked at an angle of 14° to the vertical showing the varying orientations of the Mach wave fronts that radiate at an angle of approximately 16° relative to the pile axis (Wilkes, 2017).

3.4 Acoustic Analysis

The data from both measurement days were recorded using consecutive 30 second duration files. The total number of files and piling time collected on both days is provided in Table 1. The total time used in the analysis for each pile is also provided. This excludes any clipped data and includes all of the data used in the analysis presented in this report. The track lines that correspond to the data used in the analysis are shown in Figure 2. The data collected on WTG 5 on September 17th had lower dynamic range than the data collected on September 2nd.

Table 1. Total size and number of files collected during both cruise days.

Date	Number of Files Collected	Total Data Collected	Total Recorded Time Used in Analysis
9/2/2015	145	4.08 GB	Pile B2: 4.7 minutes Pile A2: 50.1 minutes
9/17/2015	342	9.76 GB	Pile A1: 74.4 minutes

All analysis was completed using custom MATLAB scripts. Each individual 30 second duration file was opened in MATLAB and adjusted to account for the amplifier gain and hydrophone sensitivity. Thus, each file then represented the received level of the sound at each hydrophone.

A peak detector was employed to locate all of the pile driving impulses in the recordings. For each impulse, the peak and peak-to-peak sound pressure received levels were calculated according to Equations 2 and 3, respectively

$$RL_{pk} = 20\log_{10}(max(|P(t)|)) \qquad \text{(Eq. 2)}$$

$$RL_{pk-pk} = 20\log_{10}(max(P(t)) - min(P(t))) \qquad \text{(Eq. 3)}$$

The sound exposure level was also calculated for each impulse according to Equation 4, with the signal duration being defined as the 90% envelope (T_{90}) or the amount of time that contains 90% of the signal energy. This is a meaningful definition of the signal duration that begins when the cumulative signal energy exceeds 5% (T_5) of the total signal energy and ends when it reaches 95% (T_{95}) of this value. The 90% envelope is $T_{95} - T_5$.

$$SEL = 10\log_{10}\left(\int_{T5}^{T95} P(t)^2 dt\right) \qquad \text{(Eq. 4)}$$

The rise and decay times of each impulse were also calculated. The rise time was defined as the peak time minus the time at which 5% of the energy is present (T_5). The decay time was defined as the time at which 95% of the energy is present (T_{95}) minus the peak time.

The kurtosis of each impulse was also calculated. Kurtosis is a measure of the "impulsiveness" and variance of a signal. Higher kurtosis relates to a signal where the variance is a result of infrequent extreme deviations as opposed to frequent, modestly sized deviations. A signal that has the same power spectrum can have much different kurtosis values depending on the impulsiveness of the signal.

For example, Figure 7 provides a comparison of two signals that have the same energy spectrum. The signal on the left has constant variance and deviations and results in a kurtosis of 3. The signal on the right is impulsive and therefore consists of an extreme pressure fluctuation, which results in a higher kurtosis value of 189.

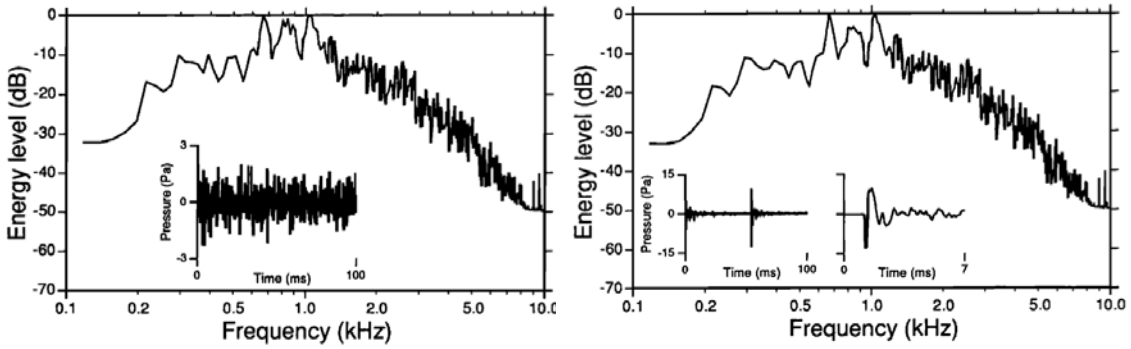

Figure 7. Comparison of two signals that have the same average energy spectrums but result in different kurtosis values depending on the impulsiveness of the signal. The signal on the left has a kurtosis value of 3, whereas the signal on the right has a kurtosis value of 189 (Hamernik, 1993).

A time window of 0.1 seconds before and 0.8 seconds after the peak were used for this calculation. This time window was chosen to account for the varying time interval between hammer drops. This window ensured the kurtosis calculation only contained one impulse and did not overlap adjacent hammer drops. Examples of the time windows used in the SEL and kurtosis calculations are shown in Figure 8.

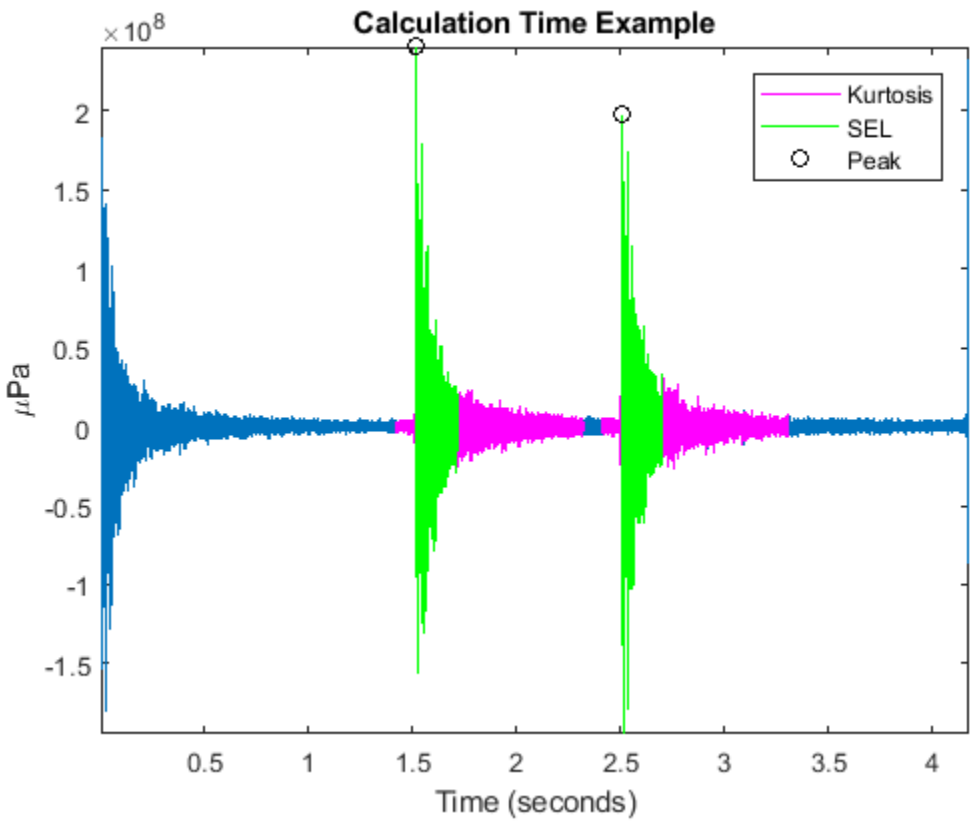

Figure 8. Example of time windows used for SEL and kurtosis calculations on two impulses.

These metrics were plotted against range from the pile to visualize the variation in values over distance and investigate the range dependence of the signal.

3.5 Statistical Analysis

One of the reasons for applying a statistical model to these data is that many of the predictive variables (i.e., penetration depth of the pile into the sediment, strike energy of each hammer impulse, range of the array from pile driving activity) were changing throughout the measurement. The range from source to receiver was increasing. The strike energy generally increased in relatively large increments (blue line, Figure 9) and the penetration depth into the sediment gradually increased (black line, Figure 9).

If these varying conditions are not teased apart, counter-intuitive results can occur. For example, a simple plot of received level measured on the towed array as a function of strike energy (Figure 10) shows that as the strike energy increased, received level decreased. This paradoxical finding is the result of simultaneous changes in strike energy, range of array from pile driving, and pile penetration depth.

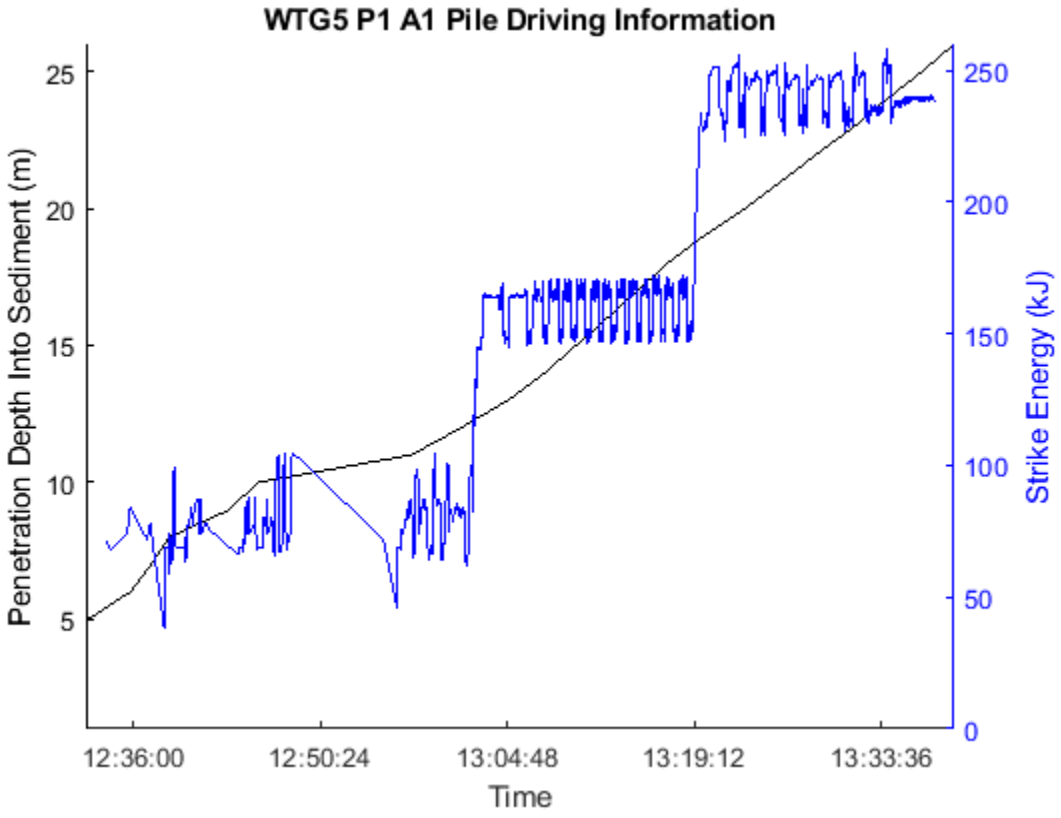

Figure 9. Penetration depth (black) and strike energy (blue) over the course of the A1 pile being driven during the September 17, 2015 recording.

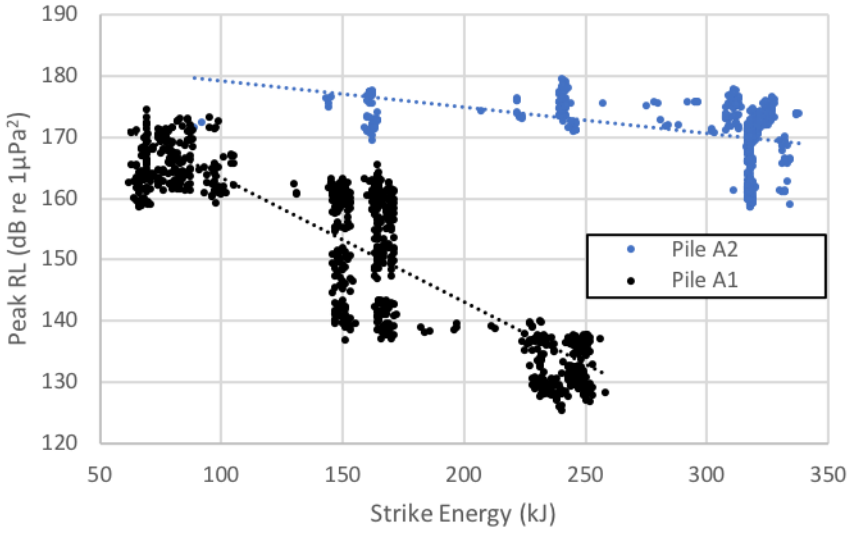

Figure 10: Simple plot of towed array peak received level as a function of strike energy. This presentation shows a decrease in received sound levels as strike energy increases. This paradoxical finding is the result of simultaneous changes in strike energy, receiver range and pile penetration depth. Pile A2 is from September 2 and Pile A1 is from September 17.

The combined data from both measurement days and three piling events were analyzed statistically using multiple regression models to explore the relationship of the received level metrics as functions of the following predictor (independent) variables: 1) the log of range, 2) the 3D angle of the pile relative to the hydrophone array (described below), 3) pile penetration depth (Johnson transformed to reduce skewness), 4) strike energy (kJ) and 5) the interaction term of strike energy and pile depth.. The individual measures of peak RL, SEL and kurtosis from the eight hydrophones were averaged for each pile strike. This prevented artificial inflation of sample size and pseudo replication. Individual regression models were created for each dependent metric.

Since the piles were raked relative to vertical, the three-dimensional (3D) angle or apparent angle of the pile changed depending on the orientation of the array to the pile. This is illustrated in Figure 11. The piles are angled at 13.27˚ relative to the centerline of the support jacket. The 3D angle relative to the receiver was calculated using Equation 5 and Figure 11, where β is the horizontal angle between the pile and direction of the receiver (see Figure 3). A positive 3D angle means the pile is angled more towards the surface and a negative angle means the pile is angled more towards the seafloor.

$$3D\ Angle = \tan^{-1}(\cos\beta * \tan(13.27°)) \qquad (Eq. 5)$$

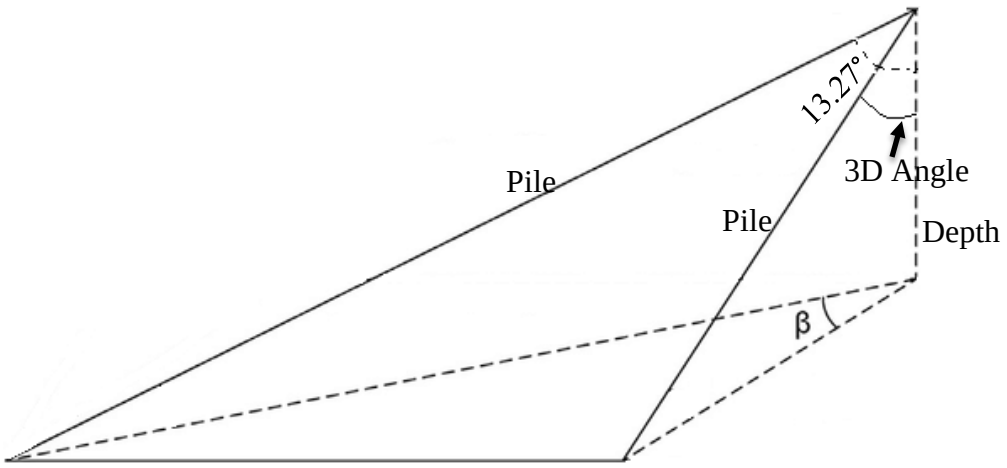

Figure 11. Schematic showing the 3D apparent angle and how this angle changes with the perspective of the array. The pile length and depth are constant, but the angle of the pile to the vertical appears to change as the horizontal angle (β) from the pile direction changes. This apparent angle is measured as the 3D angle according to Equation 5.

For example, pile B2 has an orientation of 90°. The bearing from the jacket structure to the ship was around a constant of 140˚. Thus, the horizontal angle between the pile being driven and the array was roughly 50˚ (140˚ - 90˚) and the 3D angle of the pile relative to the array was 8.6˚.

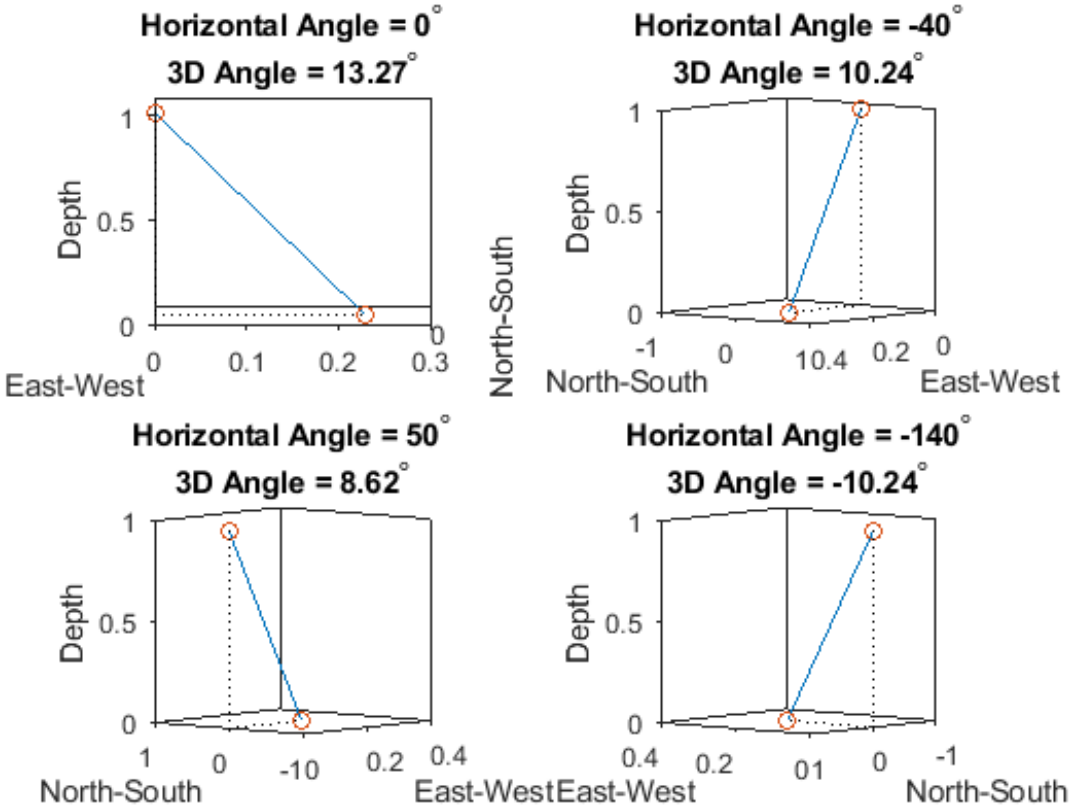

Figure 12: An illustration of the 3D angle, the bearing dependent apparent angle between the pile and a vertical line. The views that result from the horizontal orientation of the pile and array, as in Figure 3, are shown. The resulting 3D apparent angles for each array orientation are provided. A negative 3D angle means the pile is angled more towards the bottom, whereas a positive angle is when the pile is angled more towards the surface.

4. Results

4.1 Pile Driving Sound

4.1.1 Received Levels

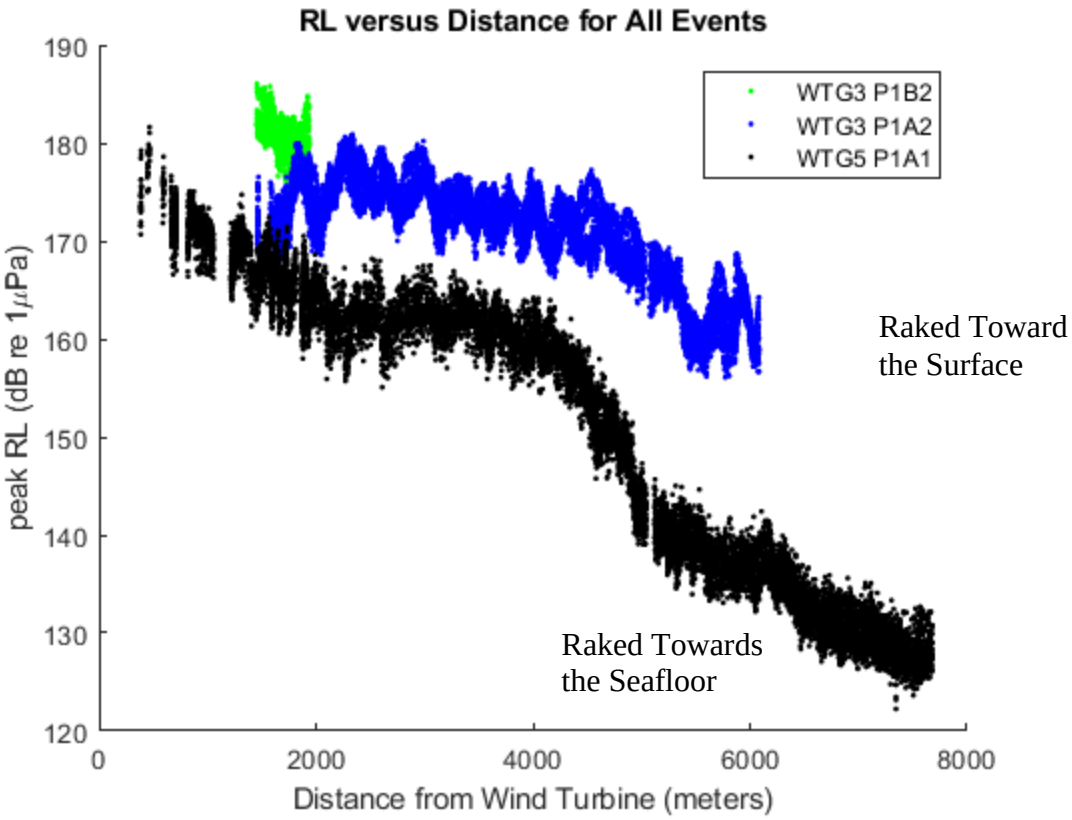

Figure 13. Peak received level for each pile driving impulse for all three pile driving events.

The peak RL calculated for all three pile driving events revealed larger RLs from the piles angled towards the surface (blue and green) versus the pile angled towards the bottom (black). Because the orientation of the Mach cone is relative to the raked pile, when the pile was angled towards the bottom more energy was directed towards the sediment. This resulted in more bottom interactions and subsequent attenuation that reduced the measured received levels at range. When the array was oriented such that the pile was raked towards the surface, the Mach cone propagated more horizontally through the water column and therefore suffered less interface attenuation, as supported by Figures 5 and 6. The same trend is seen in the SEL calculations in Figure 14.

4.1.2 Sound Exposure Levels

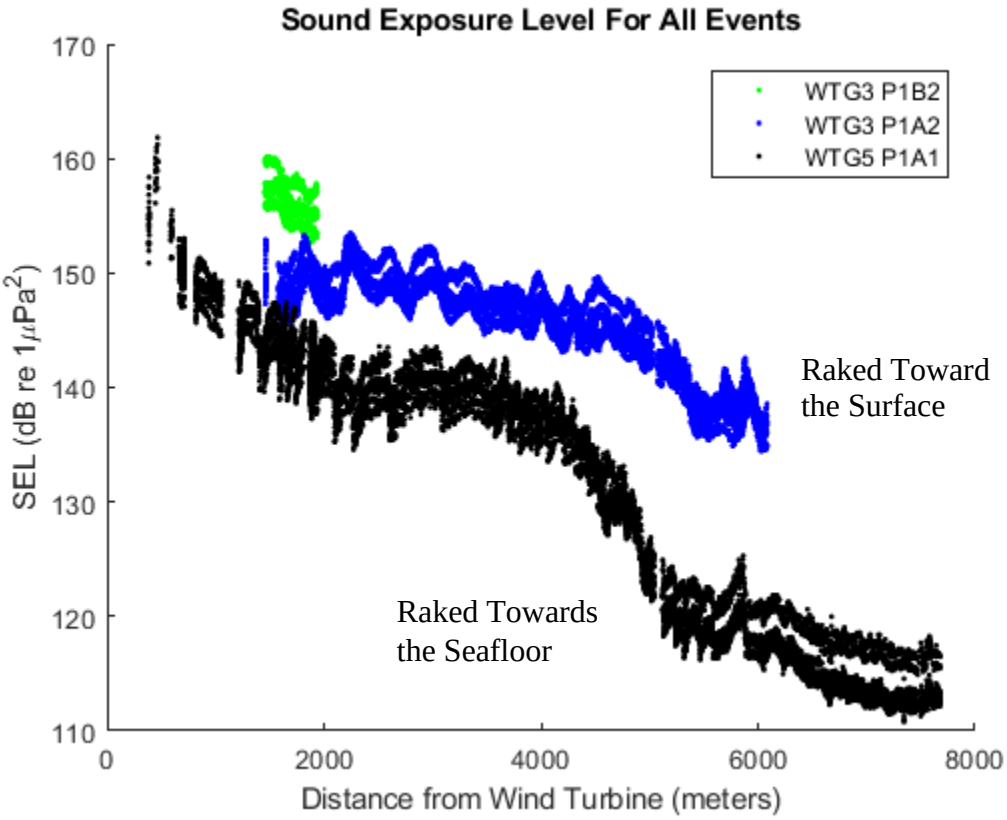

Figure 14. Single strike sound exposure levels using a signal duration of T_{90} for each pile driving impulse for all three pile driving events.

4.1.3 Kurtosis

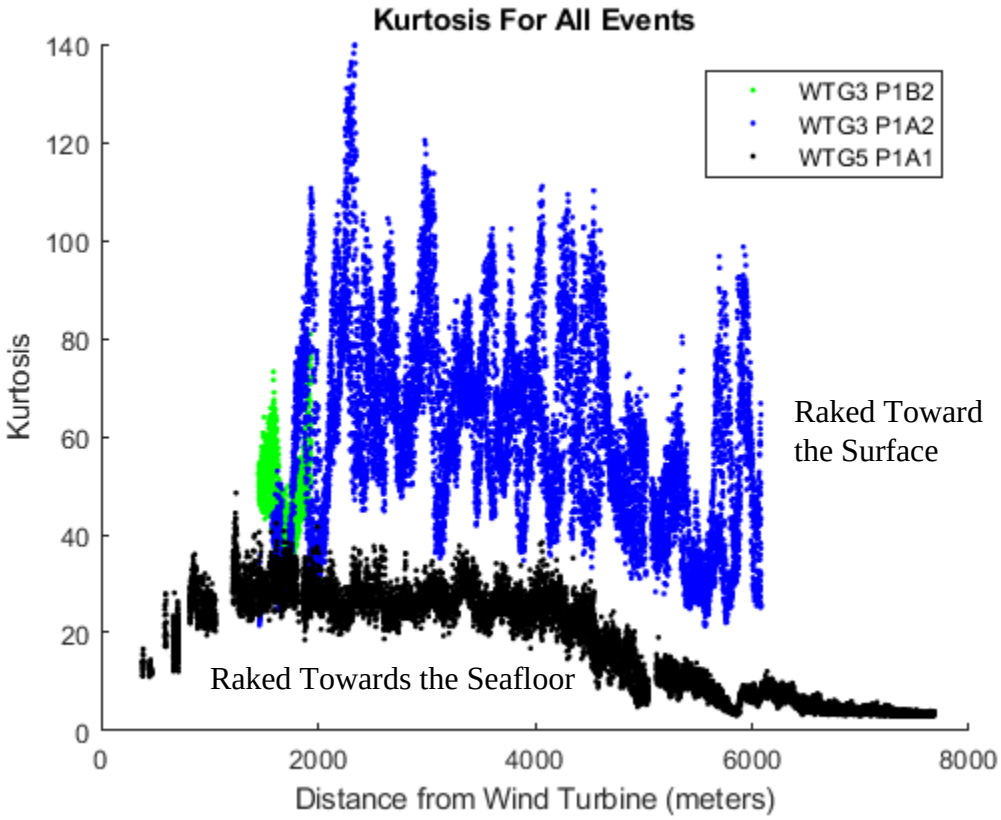

Figure 15. Kurtosis for each pile driving impulse for all three pile driving events. Calculated using 0.1 seconds before and 0.8 seconds after the peak.

Kurtosis is a measure of the impulsiveness of a signal (Hamernik et al. 1993). As the array travels further from the pile driving, the signal has increased travel and spreading time. This results in an elongated signal due to multipath arrivals, which decreases the impulsiveness of the signal in the time domain. Therefore, signals received at closer ranges are expected to have higher kurtosis than those at farther ranges. The relative trend of the measured kurtosis in Figure 15 shows the kurtosis decreasing as the array moves out in range. This trend is seen regardless of the inclination of the pile in relation to the array.

4.1.4 Decay Time

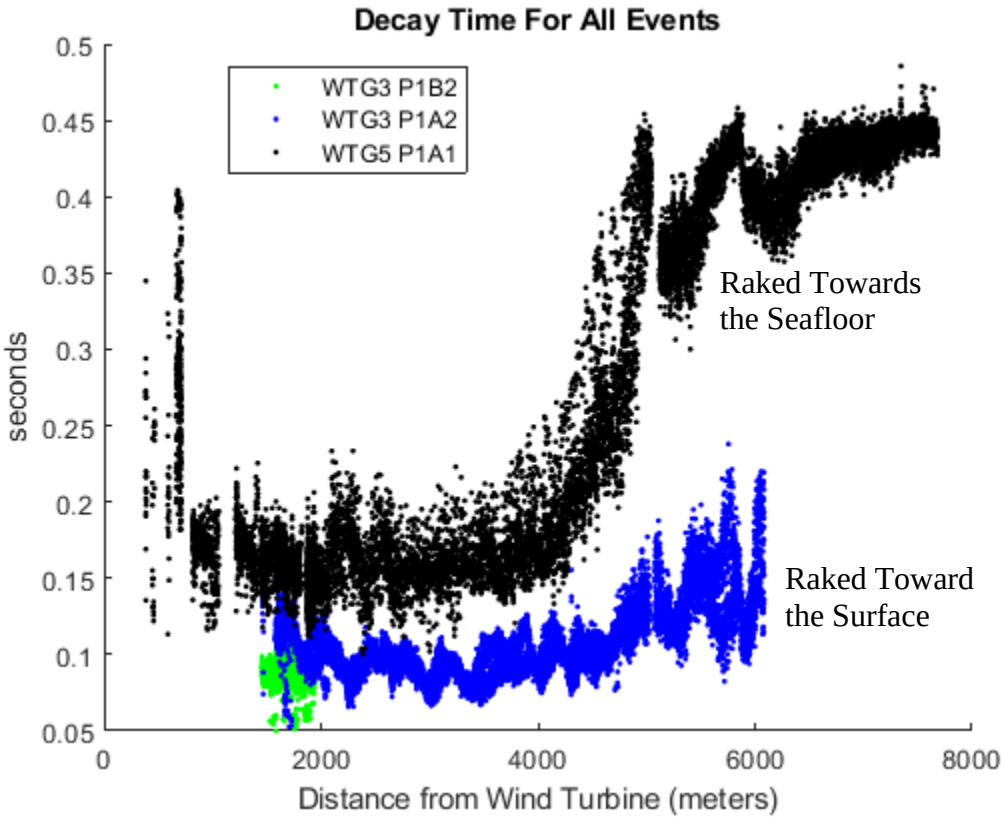

Figure 16. Decay time for each pile driving impulse for all three pile driving events. Calculated by determining the time interval between the peak and the time at which 95% of the energy had passed (T_{95}).

The decay time of each impulse increases with range of the array from the pile. This is consistent with the kurtosis trend seen in Figure 15 since as the signal elongates, the kurtosis should decrease. The increase in decay time is due to the multipath arrivals spreading out in time as the array moves away from the pile.

4.2 Statistical Model

Multiple regression (MR) methods allow the simultaneous investigation of multiple predictive factors that are changing simultaneously (Manly, 1994). MR models produce estimates of the coefficients for each individual variable. These values are analogous to the slopes of simple bivariate plots, in that they indicate the direction and magnitude of the relationship between the two variables. The statistical significance of each coefficient is evaluated with its t-ratio value. The t-ratio represents the difference of the slope from a null hypothesis value of 0 (no relationship between the two variables) divided by its variance. It is important to remember that this test is done while

considering the effect of the other variables in the MR model. These t-ratios provide insight into the relative contribution of these variables to the measured values, where the absolute values of the t-ratio indicate the level of importance of that independent variable in the model. The probability of a predictor randomly differing from 0 is reported as Prob > |t|. Values less than 0.05 are generally accepted as statistically significant and are marked with an asterisk. Many predictors can be statistically significant, but those with a greater t-ratio have more impact in the model than variables with lower t-ratios.

Given the apparent strong change in received sound levels (Figure 13 and Figure 14) and decay time (Figure 16) at approximately 4500 meters, the statistical model was stratified to separately examine data near (< 4500 m) and far (> 4500 m) from the turbines.

4.2.1 Statistical Model of Peak Received Level Near Turbine

The overall model was statistically significant ($F_{(5,1112)} = 4030$, $p < 0.0001$) and explained 94.7% of the variance in received peak level. All predictor variables and their interaction terms were statistically significant. These values are shown in Table 2. The coefficient for log transformed range was -18.05, which is consistent with transmission loss slightly less than spherical spreading. The coefficient for 3D pile angle was 0.43, indicating that piles inclined toward the sea surface will produce higher received levels. The coefficient of the penetration depth was -1.20, indicating that as penetration depth increases, the received level should decrease. The coefficient of 0.03 for strike energy indicates that peak received level increased with increasing strike energy. Again, it is worth noting that the opposite relationship is seen in a simple bivariate plot of peak RL as a function of strike energy (see Figure 13). Finally, the interaction term between strike energy and penetration depth was also statistically significant.

Table 2: Peak RL predictor variables Near the Turbine

Term	Estimate	Std Error	t Ratio	Prob>|t|
Intercept	222.72317	3.991466	55.80	<.0001*
Log10 of Range	-18.04811	0.989294	-18.24	<.0001*
3D Angle (deg)	0.4333109	0.015311	28.30	<.0001*
Penetration depth (m)	-1.200029	0.399752	-3.00	0.0027*
Strike Energy (kJ)	0.0315802	0.002019	15.64	<.0001*
(Strike Energy (kJ)-220.839) *(Penetration depth (m)+0.47194)	0.0055376	0.002348	2.36	0.0185*

4.2.2 Statistical Model of Peak Received Level Far From Turbine

The overall model was statistically significant ($F_{(5,828)} = 14940$, $p < 0.0001$). The model explained 98.9% of the variance in received peak level. All predictor variables were statistically significant, except their interaction. These values are shown in Table 3.

The coefficient for log transformed range was -240.3. This extreme value probably results from the increased transmission loss and the lack of TL values at closer ranges. The coefficient for 3D pile angle was -0.34. However, the t-ratio for this variable is very small, indicating that it is not a meaningful predictor effect. The coefficient of the penetration depth was 14.4, indicating that as penetration depth increases, the received level also increases, a paradoxical result. The coefficient of 0.05 for strike energy indicates that peak received level increased with increasing strike energy. Finally, the interaction term between strike energy and penetration depth was not statistically significant for the distant data.

Table 3: Peak RL predictor variables Far from the Turbine

Term	Estimate	Std Error	t Ratio	Prob>|t|
Intercept	1027.3746	34.11483	30.12	<.0001*
Log10 of Range	-240.3493	9.416861	-25.52	<.0001*
3D Angle (deg)	-0.345337	0.097788	-3.53	0.0004*
Penetration depth (m)	14.433601	1.059525	13.62	<.0001*
Strike Energy (kJ)	0.0478501	0.005041	9.49	<.0001*
(Strike Energy (kJ)-254.282) *(Penetration depth (m)-0.63264)	0.0023121	0.003617	0.64	0.5229

4.2.3 Statistical Model of Sound Exposure Level (SEL) near the turbine

The overall model was statistically significant ($F_{(5,1112)} = 6897$, $p < 0.0001$). The model explained 96.2% of the variance in SEL. Predictor variables coefficient values are presented in Table 4. The coefficient for log transformed range was –20.4. This value is slightly greater than spherical spreading. The coefficient for 3D pile angle was 0.24, again indicating that piles inclined toward the sea surface will produce higher SELs. Finally, the energy coefficient of 0.02 indicates that increasing strike energy leads to higher sound levels.

Table 4: SEL predictor variable values Near the turbine

Term	Estimate	Std Error	t Ratio	Prob>|t|
Intercept	209.44728	2.768969	75.64	<.0001*
Log10 of Range	-20.40128	0.686295	-29.73	<.0001*
3D Angle (deg)	0.2437421	0.010622	22.95	<.0001*
Penetration depth (m)	0.2310326	0.277317	0.83	0.4050
Strike Energy (kJ)	0.0246587	0.001401	17.60	<.0001*
(Strike Energy (kJ)-220.839)*(Penetration depth (m)+0.47194)	0.0015755	0.001629	0.97	0.3337

4.2.4 Statistical Model of SEL far from the turbine

The overall model was statistically significant ($F_{(5,828)} = 1257$, $p < 0.0001$). The model explained 98.6% of the variance in SEL. Predictor variables coefficient values are presented in Table 5. The coefficient for log transformed range was –219. This extreme value probably results from the increased transmission loss and the lack of TL values at closer ranges. The coefficient for 3D pile angle was -0.61. However, the absolute value of the t-ratio for this variable is the smallest of all the main variables in this analysis, indicating that it is less important here. Finally, the energy coefficient of 0.04 indicates that increasing strike energy leads to slightly higher sound levels.

Table 5: SEL predictor variable values Far from the Turbine

Term	Estimate	Std Error	t Ratio	Prob>|t|
Intercept	930.5184	28.56922	32.57	<.0001*
Log10 of Range	-219.4691	7.886083	-27.83	<.0001*
3D Angle (deg)	-0.610068	0.081892	-7.45	<.0001*
Penetration depth (m)	15.337925	0.887291	17.29	<.0001*
Strike Energy (kJ)	0.0379882	0.004221	9.00	<.0001*
(Strike Energy (kJ)-254.282)*(Penetration depth (m)-0.63264)	-0.003095	0.003029	-1.02	0.3073

4.2.5 Statistical Model of Kurtosis Near the Turbine

The overall model was statistically significant ($F_{(5,1112)} = 3200$, $p < 0.0001$). The model explained 84.5% of the variance in the kurtosis metric. Predictor variables were all statistically significant. These values are presented in Table 6. The coefficient for log transformed range was 1.5, indicating that kurtosis should increase within the range to 4500 meters. However, the t-ratio for this result was low (8.69). This analysis was dominated by the 3D angle (t-ratio = 29.86), whose coefficient was 0.08, indicating that piles inclined toward the surface will have a higher kurtosis value than those inclined toward the seafloor. The coefficient for penetration was -0.64 suggesting that increased penetration depth will reduce the kurtosis of the outgoing signal. There was a very weak positive relationship between strike energy and kurtosis. Finally, the interaction term between strike energy and penetration depth was also significant.

Table 6: Kurtosis Predictor Variable Estimates Near the Turbine

Term	Estimate	Std Error	t Ratio	Prob>|t|
Intercept	-5.925874	0.707603	-8.37	<.0001*
Log10 of Range	1.5232392	0.175381	8.69	<.0001*
3D Angle (deg)	0.0810516	0.002714	29.86	<.0001*
Penetration depth (m)	-0.649541	0.070868	-9.17	<.0001*
Strike Energy (kJ)	0.0025202	0.000358	7.04	<.0001*

Term	Estimate	Std Error	t Ratio	Prob>|t|
(Strike Energy (kJ)-220.839)*(Penetration depth (m)+0.47194)	0.0026627	0.000416	6.40	<.0001*

4.2.6 Statistical Model of Kurtosis Far from the Turbine

The overall model was statistically significant ($F_{(5,828)} = 3659$, $p < 0.0001$). The model explained 95.6% of the variance in kurtosis metric. Predictor variables are presented in Table 7. The coefficient for log transformed range was – 16.7, indicating that kurtosis should decrease with range. The coefficient for penetration was 1.3 suggesting that increased penetration depth will increase the kurtosis of the signal. Neither the 3D angle nor the strike energy had any significant effect in this model.

Table 7: Kurtosis Predictor Variable Estimates far from the turbine

Term	Estimate	Std Error	t Ratio	Prob>|t|
Intercept	61.649552	4.411801	13.97	<.0001*
Log10 of Range	-16.73237	1.217808	-13.74	<.0001*
3D Angle (deg)	-0.02005	0.012646	-1.59	0.1132
Penetration depth (m)	1.3014327	0.13702	9.50	<.0001*
Strike Energy (kJ)	-0.000795	0.000652	-1.22	0.2232
(Strike Energy (kJ)-254.282)*(Penetration depth (m)-0.63264)	-0.004685	0.000468	-10.02	<.0001*

4.2.7 Statistical Model of Decay Time Near the Turbine

The overall model was statistically significant ($F_{(5,1112)} = 776$, $p < 0.0001$). The model explained 77.7% of the variance in decay time. Predictor variables values are presented in Table 8. Log transformed range was surprisingly non-significant. The coefficient for the 3D angle was -0.04, indicating that sound generated from piles inclined toward the seafloor will have longer decay times than those inclined toward the sea surface. This variable was dominant in the analysis with a t-ratio magnitude of -12.32. The coefficient for penetration was 0.35 suggesting that increased penetration depth will increase the decay time of the received signal. There was a very weak negative relationship between strike energy and decay time. Finally, the interaction of strike energy and penetration depth was significant as well.

Table 8: Decay TIme Predictor Variable Estimates near the Turbine

Term	Estimate	Std Error	t Ratio	Prob>|t|
Intercept	1.0570439	0.932019	1.13	0.2570
Log10 of Range	-0.03101	0.231003	-0.13	0.8932
3D Angle (deg)	-0.044064	0.003575	-12.32	<.0001*
Penetration depth (m)	0.353554	0.093343	3.79	0.0002*
Strike Energy (kJ)	-0.005132	0.000471	-10.88	<.0001*

Term	Estimate	Std Error	t Ratio	Prob>|t|
(Strike Energy (kJ)-220.839)*(Penetration depth (m)+0.47194)	-0.001342	0.000548	-2.45	0.0145*

4.2.8 Statistical Model of Decay Time Far from the Turbine

The overall model was statistically significant ($F_{(5,828)} = 5485$, $p < 0.0001$). The model explained 97.1% of the variance in decay time. Predictor variables were all statistically significant. These values are presented in Table 9. The coefficient for log transformed range was 14.2, indicating that decay time should strongly increase with range. The coefficient for the 3D angle was 0.02, indicating that piles inclined toward the sea surface will have a slightly shorter decay time than those inclined toward the sea floor. The coefficient for penetration was -1.15 suggesting that increased penetration depth will shorten the decay time of the received signal. There was a very weak positive relationship between strike energy and kurtosis. Finally, the interaction term between strike energy and penetration depth was strongly significant.

Table 9: Decay Time Predictor Variable Estimates far from the turbine

Term	Estimate	Std Error	t Ratio	Prob>|t|
Intercept	-52.45953	2.941039	-17.84	<.0001*
Log10 of Range	14.264479	0.811827	17.57	<.0001*
3D Angle (deg)	0.0204385	0.00843	2.42	0.0155*
Penetration depth (m)	-1.158204	0.091342	-12.68	<.0001*
Strike Energy (kJ)	0.0009681	0.000435	2.23	0.0262*
(Strike Energy (kJ)-254.282)*(Penetration depth (m)-0.63264)	0.0052605	0.000312	16.87	<.0001*

4.2.9 Statistical Summary

The previous subsections reported the results for each measured variable separately. This section presents a summary and synthesis of those results. Table 10 summarizes the direction and magnitude of the relationship between the measured (dependent) and predictor (independent) variables in all of the previous tables. Using the t-ratio values, the significance of the parameter in defining the relationship is represented with one + or – sign if the t-ratio value is less than 1, two + or – signs if the t-ratio value is greater than 1 but less than 10, and three + or – signs if the t-ratio value is greater than 10. NS stands for “non-significant.”

Both received sound level metrics of peak RL and SEL decreased strongly with range (Tables 2-5). Kurtosis initially increased at short ranges (Table 6) and then decreased strongly at ranges beyond 4500 m (Table 7). This effect is shown in both Figure 14 and Table 10. Likewise decay time only began to significantly increase at

ranges greater than 4500 m. The kurtosis and decay time metrics show the effect of increased multipath arrivals with increasing range.

The analysis indicates that when the pile is raked toward the surface the received levels metrics (Tables 2 and 4) and kurtosis (Table 6) both increase at the closer ranges, while decay time decreases (Table 8). The opposite pattern is seen at ranges greater than 4500 m (Tables 3, 5, 7 and 9). All of these effects are consistent with sound that propagates more horizontally in the water column. The subsequent reduction in boundary interactions reduced transmission loss.

Penetration depth had little effect on received level at close ranges, but increased RL at greater ranges (Table 3 and 5). This may be due to enhanced coupling of the pile to the sediment and subsequent acoustic re-radiation into the water column. The effect of increased penetration depth on kurtosis and decay time was less clear, with apparently contradictory effects of reducing kurtosis but increasing decay time at short ranges.

Increased strike energy led to increased received level metrics at all ranges (Tables 2-5) and kurtosis near the turbine (Table 6). Decay time decreased at close range near the turbine (Table 8) but increased at longer ranges. This may be due to a slightly stronger main pulse at close ranges and increased multiple arrivals at longer ranges.

Table 10: Statistical Summary. The sign indicates the direction of the effect and the number of + or – signs indicate the relative strength of the effect based on the t-ratio values. NS indicates a non-significant effect.

Predictors		Measured Values			
		Peak RL	SEL	Kurtosis	Decay Time
Log Range	Near	---	---	++	NS
	Far	---	---	---	+++
3D Angle	Near	+++	+++	+++	---
	Far	--	--	--	++
Penetration Depth	Near	--	NS	--	++
	Far	+++	+++	NS	---
Strike Energy	Near	+++	+++	++	---
	Far	++	++	NS	++
Strike Energy x Penetration Depth	Near	++	NS	++	--
	Far	NS	NS	---	+++

5. Discussion

The three different pile driving events recorded on the towed array resulted in differing peak received levels, sound exposure levels, decay times and kurtosis values. The differences were hypothesized to be due to the angle of the pile being driven relative to the towed array. The angle of the pile relative to the array changes based on the bearing of the array from the pile being driven. Figure 4 indicates that the horizontal bearing of the array to the piles was similar for the September 2 deployments, but much different during the September 17 deployment. This difference in bearing resulted in the pile being angled more towards the seafloor during the September 17 measurements than for the September 2 measurements.

The inclination of pile away towards the surface produced higher received levels, as predicted by pile jacket geometry and Mach cone propagation theory (Reinhall and Dahl, 2011 and Wilkes, 2017). This was noted when the received levels recorded on September 2 were higher than those recorded on September 17. Increased kurtosis values when the pile is inclined towards the surface also derived from enhanced propagation through the water column and fewer interactions with the waveguide boundaries. Therefore, the received signal was more impulsive and the signal energy was not as elongated in time since it contained less multipath arrivals. On the other hand, when the pile is angled towards the seafloor more sound energy is directed towards the sediment and therefore less sound is transferred directly through the water column.

The signal elongating in time was directly observed by measuring the decay time of each impulse. The decay time increased with range, with a sharp increase at a distance of around 5 km. The data from September 2 also showed the decay time trending upwards around 5km. This sharp increase could be a result of propagation effects due to varying bathymetry along this radial.

Overall the raked pile has an azimuthal dependent beam pattern. Precise measurement of the beam pattern was not within the scope of this project, but the differences in signal characteristics and received level due to this azimuthal dependence were observed between the two measurement days. This azimuthal dependence was the driving factor behind the differences in measurements between the two pile driving days. There was little correlation between the penetration depth and strike energy and the received sound levels recorded so no conclusion can be drawn as to how those affected the data. The increasing decay time and decreasing kurtosis suggest that the signal was becoming less impulsive with range, but there was no clear transition point to where the signal became definitively non-impulsive. More measurements would have to be taken to further define this transition point, which would be location and source dependent.

Literature Cited

Charif, R., A. Waack, and L. Strickman. (2010). Raven Pro 1.4 User's Manual. Ithaca, NY: Cornell Laboratory of Ornithology.

Dahl, P.H. and Reinhall, Per & Popper, Arthur & C Hastings, Mardi & Ainslie, Michael. (2014). Underwater sound from pile driving, what is it and why does it matter. The Journal of the Acoustical Society of America. 135. 2312. 10.1121/1.4877620.

Hamernik, R. P., W.A Ahroon, K.D. Hsueh, S. Lei and R.I. Davis. (1993). Audiometric and histological differences between the effects of continuous and impulsive noise exposures. The Journal of the Acoustical Society of America. 93(4). 2088-2095. 10.1121/1.406695

Manly, B. F. J. (1994). *Multivariate Statistical Methods* (Chapman & Hall, London).

Reinhall, P. G., and P. H. Dahl, (2011). Underwater Mach wave radiation from impact pile driving: theory and observation, The Journal of the Acoustical Society of America 130, 1209-1216.

Slifker, J. F., and Shapiro, S. S. (1980). The Johnson System: Selection and Parameter Estimation. Technometrics 22, 239-246. 10.1080/00401706.1980.10486139

Wilkes, D.R. and A.N. Gavrilov. (2017). Sound radiation from impact-driven raked piles. The Journal of the Acoustical Society of America. 142, 1-11. 10.1121/1.4990021

Department of the Interior (DOI)

The Department of the Interior protects and manages the Nation's natural resources and cultural heritage; provides scientific and other information about those resources; and honors the Nation's trust responsibilities or special commitments to American Indians, Alaska Natives, and affiliated island communities.

Bureau of Ocean Energy Management (BOEM)

The mission of the Bureau of Ocean Energy Management is to manage development of U.S. Outer Continental Shelf energy and mineral resources in an environmentally and economically responsible way.

BOEM Environmental Studies Program

The mission of the Environmental Studies Program is to provide the information needed to predict, assess, and manage impacts from offshore energy and marine mineral exploration, development, and production activities on human, marine, and coastal environments. The proposal, selection, research, review, collaboration, production, and dissemination of each of BOEM's Environmental Studies follows the DOI Code of Scientific and Scholarly Conduct, in support of a culture of scientific and professional integrity, as set out in the DOI Departmental Manual (305 DM 3).